THÈSE

En vue de l'obtention du

DOCTORAT DE L'UNIVERSITÉ DE TOULOUSE

Délivré par : *l'Université Toulouse 3 Paul Sabatier (UT3 Paul Sabatier)*

Présentée et soutenue le *29/11/2019* **par :**

JONG HOON KIM

Compressed Sensing and Finite Rate of Innovation for Efficient Data Acquisition of Quantitative Acoustic Microscopy Images

JURY

Su Ruan	Professeur des Universités	Rapporteur
Xavier Descombes	Directeur de Recherche	Rapporteur
Hervé Liebgott	Professeur des Universités	Examinateur
Jonathan Mamou	Directeur de Recherche	Examinateur
Alin Achim	Professeur des Universités	Examinateur
Adrian BASARAB	Maître de Conférences	Directeur de Thèse
Denis KOUAMÉ	Professeur des Universités	Co-Directeur de Thèse

École doctorale et spécialité :
MITT : Signal, Image, Acoustique et Optimisation
Unité de Recherche :
Institut de Recherche en Informatique de Toulouseétologie (UMR CNRS 5505)
Directeur(s) de Thèse :
Adrian BASARAB et *Denis KOUAMÉ*
Rapporteurs :
Su Ruan, Xavier Descombes

Abstract

Quantitative acoustic microscopy (QAM) is a well-accepted modality for forming 2D parameter maps making use of mechanical properties of soft tissues at microscopic scales. In leading edge QAM studies, the sample is raster-scanned (spatial step size of $2\mu m$) using a 250 MHz transducer resulting in a 3D RF data cube, and each RF signal for each spatial location is processed to obtain acoustic parameters, *e.g.*, speed of sound or acoustic impedance. The scanning time directly depends on the sample size and can range from few minutes to tens of minutes. In order to maintain constant experimental conditions for the sensitive thin sectioned samples, the scanning time is an important practical issue.

To deal with the current challenge, we propose the novel approach inspired by compressed sensing (CS) and finite rate of innovation (FRI). The success of CS relies on the sparsity of data under consideration, incoherent measurement and optimization technique. On the other hand, the idea behind FRI is supported by a signal model fully characterized as a limited number of parameters. From this perspective, taking into account the physics leading to data acquisition of QAM system, the QAM data can be regarded as an adequate application amenable to the state of the art technologies aforementioned. However, when it comes to the mechanical structure of QAM system which does not support canonical CS measurement manners on the one hand, and the compositions of the RF signal model unsuitable to existing FRI schemes on the other hand, the advanced frameworks are still not perfect methods to resolve the problems that we are facing.

In this thesis, to overcome the limitations, a novel sensing framework for CS is presented in spatial domain: a recently proposed approximate message passing (AMP) algorithm is adapted to account for the underlying data statistics of samples sparsely collected by proposed scanning patterns. In time domain, as an approach for achieving an accurate recovery from a small set of samples of QAM RF signals, we employ sum of sincs (SoS) sampling kernel and autoregressive (AR) model estimator. The spiral scanning manner, introduced as an applicable sensing technique to QAM system, contributed to the significant reduction of the number of spatial samples when reconstructing speed of sound images of a human lymph node. Furthermore, the scanning time was also hugely saved due to the merit of the mechanical movement of the proposed sensing pattern. Together with the achievement in spatial domain, the introduction of SoS kernel and AR estimator responsible for an innovation rate sampling and a parameter estimation respectively led to dramatic reduction of the required number of samples per RF signal compared to a conventional approach. Finally, we showed that both data acquisition frameworks based on the CS and FRI can be combined into a single spatio-temporal solution to maximize the benefits stated above.

Keywords – Quantitative acoustic microscopy, compressed sensing, sparsity, incoherent measurement, approximate message passing, Cauchy denoiser, sensing pattern, finite rate of innovation, parametric model, sum of sinc kernel, autoregressive model

Contents

Chapter 1

Introduction

Contents

Ultrasonography is one of the major medical imaging modalities, and in particular occupies an exclusive status in obstetrics monitoring due to its clinical safety to not use ionizing radiation, as well as in cardiology owing to its real-time visualization ability. Furthermore, its various merits such as low cost, portability and relatively easy operation make it widely used in medical fields after radiography. Aside from the features stated above, this thesis focuses on the fact that the physics of ultrasound (US) can be exploited to investigate and even quantify biomechanical properties of biological soft tissues. Quantitative acoustic microscopy (QAM), which forms an image in micro scale with quantified parameters by evaluating elastic properties of soft tissues, is a representative application.

This chapter begins by an overview of the fundamental physics of US imaging, and subsequently addresses the distinct characteristics and mechanical principles of QAM. Then, as the motivation of this study, we underline the intrinsic limitations and challenges which the QAM technology is currently facing, and present the objectives and contributions of this work. Finally, the overall structure of the thesis is presented.

1.1 Ultrasound wave

The process to form an image within the QAM technology is very similar to the one in the conventional medical US imaging in the sense that US pulses are utilized to investigate target objects. Therefore, prior to exploring the QAM, we review the physical basics of US wave and the fundamental knowledge of US instruments addressed in the literature [Fanet 2014, Smith 2010, Kremkau 1993, Trots 2007].

US is defined as pressure waves with RF spectrum exceeding the maximum audible frequency of 20 KHz, which requires a source to generate them and a physical medium to propagate. While an US pulse emitted from the source travels inside mediums consisting of multiple different echogenic materials, it undergoes several physical phenomena such as reflection, transmission, refraction, scattering and so forth which are triggered by the difference of acoustic properties at the boundaries among each medium. Thus, a diagnostic echography is constructed basically measuring the perturbation level of soft tissues with respect to the irradiated US. The acoustic characteristics of typical biological tissues and certain materials of interest are displayed in Table 1.1. The numbers offer the intuition that the mechanical properties of tissues are affecting the manner of US wave propagation, and thus the contrast of the values can be utilized to not only visualize the internal structure of human body, but also explore pathogenesis for instance, in oncology. The conventional medical US imaging has been implemented in diverse modes commensurate with its clinical purpose: A-mode (amplitude), B-mode (brightness), M-mode (motion) and Doppler modes. Furthermore, the advanced methodologies in signal and image processing on the one hand, and the development of hardware on the other hand enable to expect the emergence of innovative imaging technologies such as 3D or 4D US imaging. Describing the details of the modes exemplified above is beyond our focus, and thus interested readers in the areas can be referred to [Fanet 2014].

In the next sections we will inspect the nature of US wave on the perspective of how to generate and detect it, and how it interacts with a given medium.

Table 1.1: Acoustic characteristics of biological tissues and certain materials [Fanet 2014]

Biological tissues and materials	Density (kg/m^3)	Speed of sound(SOS) (m/s)	Acoustic impedance (kg/[m$^2 \cdot$ s])
Air	1.20	344	430
Water	1000	1480	1.52 $\times 10^6$
Blood	1060	1530	1.62 $\times 10^6$
Fat	920	1410 to 1470	1.34 to 1.39$\times 10^6$
Muscle	1070	1500 to 1640	1.65 to 1.70$\times 10^6$
Liver	1060	1550	1.65$\times 10^6$
Kidney	1040	1560	1.62$\times 10^6$
Bone	1200 to 1810	2700 to 4100	3.2 to 7.8$\times 10^6$
Lung	400	650	0.26$\times 10^6$
Skin		1519	1.58$\times 10^6$
Blood Vessels	1080	1530	1.65$\times 10^6$
Soft tissues		1540 on average	1.63$\times 10^6$
Spleen	1060	1566	1.66$\times 10^6$
Quartz		5750	1.52$\times 10^7$

1.1.1 Transducer

Piezoelectric phenomenon. US waves are produced and detected at a shaped piezoelectric material in a device called a transducer or probe. Fig. 1.1 illustrates a single element transducer activated by the piezoelectric phenomena; electrical energy can be converted into mechanical vibrations, *i.e.*, ultimately US waves, and conversely acoustic energy can be also transformed to electric pulses. The conversion of the energy forms described above is completed by PZT standing for lead (Pb) zirconate titanate, which is a piezoelectric resonator transmitting US pressure by regularly changing its physical shape when a voltage is applied, and generating electric signals when being excited by external vibrations.

Matching layer. The matching layer located at the tip of a transducer is hired so as to minimize the loss of the energy entering into a patient's skin by lowering the gap of the acoustic impedance between PZT and skin. Specifically, the acoustic flow is affected by the difference of acoustic impedances of two adjacent materials perpendicularly aligned to the travel path of US. Therefore, the acoustic characteristic of the matching layer to be adopted is determined by the relationship of $Z_m = \sqrt{Z_p Z_s}$ where Z_m, Z_p and Z_s denote the acoustic impedances of matching layer, PZT and skin respectively. The

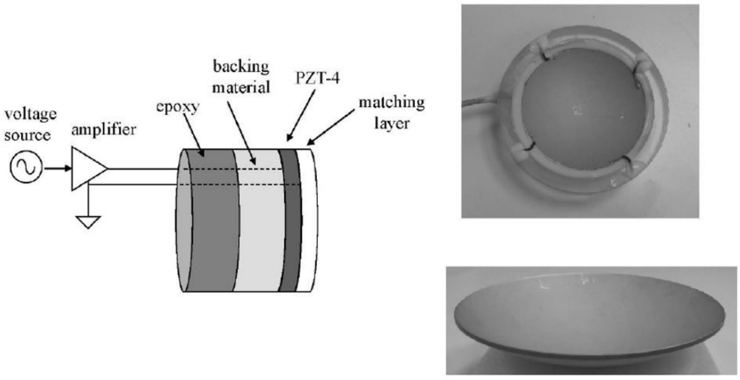

Figure 1.1: A single element transducer [Smith 2010]

details on the physics of US associated with this consideration are discussed in the following subsection.

Beamforming. In the bottom right image of Fig. 1.1, the lens of the transducer is displayed, which has a concave shape in order to concentrate the emitted acoustic energy on a specific local area to be identified. In single element transducers, the geometry lens leads to a mechanical beamforming, in other words determines a focal zone consisting of both the beam width at the focused point and the focal length as a working distance, which turns out to dictate the lateral resolution [Fanet 2014]. By contrast, the multi-element probes hire the electronic beamforming technique for focusing of US, which are comprised of unfocused rectangular elements sequentially arranged with various geometries in accordance with their medical use: linear array, convex array, annular array, etc. The electronic beamforming produces an effective focused beam by applying voltage pulses with a relative delay in time with respect to individual elements of the piezoelectric array (for the beamforming process of a linear array, refer to Fig. 1.2). Unlike the medical US imaging used to rapidly acquire a cross sectional image in real-time, the beamforming for QAM is done by the mechanical focusing based on a single element transducer described above, and thus the detailed review on the architecture or operation of the arrays subjected to the electronic beamforming is not covered in this thesis. Instead, we will mainly focus on the exploration of dedicated transducer to QAM in section 1.2.1.

Frequency and bandwidth. As another characteristic of a transducer, the resonant frequency and its bandwidth are deeply involved in determining the axial and lateral resolutions. Fig. 1.3 reveals the series of steps for electrical signals to be converted into pressure waves; Voltage pulses, produced by periodically gating the output of a

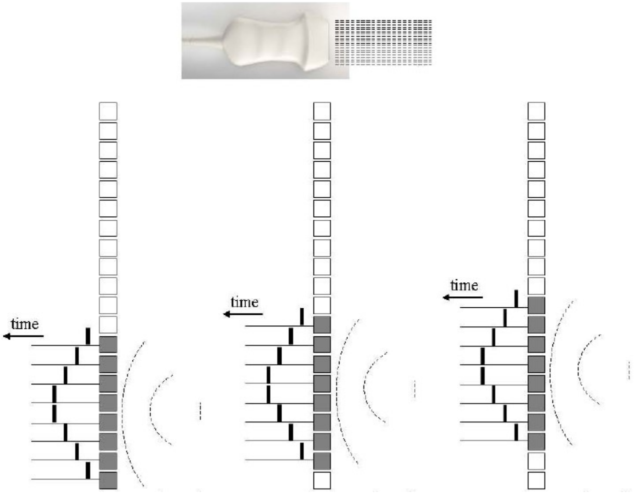

Figure 1.2: Electronic beamforming of a linear array [Smith 2010]

frequency generator with the pulse repetition rate (PRR), are applied to the face of the PZT element, the damping characteristic of which determines the shape of pressure waves or bandwidth. Fig. 1.4 highlights the mechanical damping effect of a transducer which acts like a bandpass filter, *i.e.*, the wider bandwidth leads to the heavier damping and the shorter the duration of the pressure wave [Trots 2007]. The frequency component, located at the central position of the spectrum shown in the left images of Fig. 1.4, is called the center frequency which determines the spatial resolution of an echogram together with the bandwidth and beamforming.

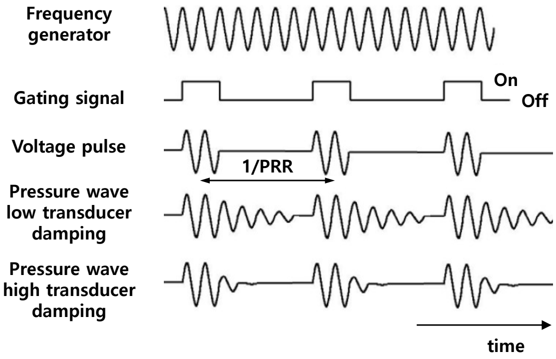

Figure 1.3: Generating pressure waves from electrical signals [Smith 2010]

Resolution. The spatial resolution representing the degree of image clarity is, in an US system, evaluated from two perspectives: one is the lateral resolution showing the ability to distinguish two structures closely situated on the same perpendicular plane to the beam propagation, the other is the axial resolution related to the minimum distance

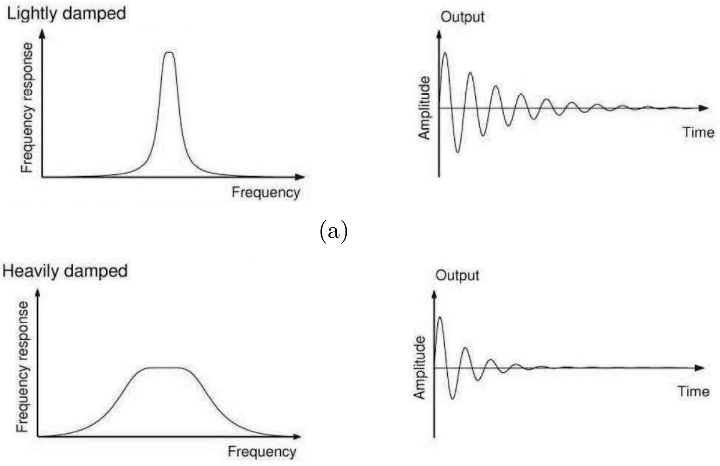

(a)

(b)

Figure 1.4: The pulse shape varies with the damping characteristic of the transducer. The pressure wave lightly damped (a) has narrower bandwidth and dies out more slowly than one heavily damped (b) [Trots 2007].

distinguishable between two structures lined up along the direction of propagation of US beam. The lateral resolution can be improved by increasing the center frequency or decreasing the beam width using beamforming techniques as stated previously. On the other hand, the axial resolution is improved by shorter duration of the US pulse, *i.e.*, the higher damping degree which also means the wider bandwidth and the higher center frequency.

Frequency attenuation. It should be noted that the higher frequency, the greater attenuation, namely the penetrability of the US wave is inversely related to the frequency. The attenuation indicates all of energy losses occurring over the wave propagation. To be more specific, when expressing the energy as a function with respect to the distance (z) in the propagation direction, it is defined as an exponential decay relative to the attenuation coefficients ($\boldsymbol{\alpha}$) as follows:

$$P(z) = P_0 e^{-\alpha z} \tag{1.1}$$

where P_0 represents the original pressure amplitude at position of $z = 0$ and $\boldsymbol{\alpha}$ expressed in Nepers/cm is given by:

$$\alpha = \frac{1}{z} ln \frac{P_0}{P(z)} \tag{1.2}$$

The attenuation coefficient is proportionally related to the frequency and can be recast as:

$$\alpha(f) = bf^m \tag{1.3}$$

where m is considered as marginally greater than one for most biological tissues, and b is a constant varying with tissues; for example, $m = 1.2$ and $b = 0.5$ in homogeneous liver [Kouamé 2015]. Therefore, as far as the choice of working frequency of the transducer is concerned, one must consider the tradeoff between the desired resolution and the depth to be explored, which is demonstrated in Fig. 1.5. It is clearly unveiled that the quality of the resulting images is dominated by the operating frequency, which is getting higher as moving towards the right side image. Compared to the left image, the edges on the right image are much sharper whereas it severely suffers from the poor penetration, and thus completely fails to get echograms in deep regions (the bottom of images).

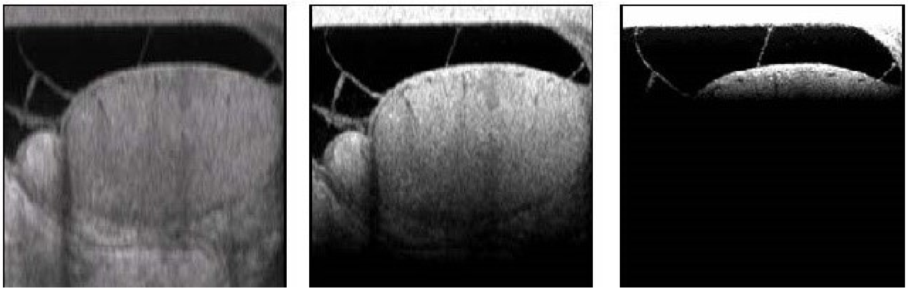

Figure 1.5: The resulting images of a same object irradiated by US beam are displayed, the quality of which is varied depending on the operating frequency. The top and bottom on the images corresponds to respectively near and far region from the probe [Smith 2010].

1.1.2 Physics of ultrasound

Wavefronts. The US wave emitted from a source forms a wavefront which are the set of points of medium being simultaneously agitated by the applied pressure, and classified by three types depending on its shape: spherical waves, cylindrical waves and plane waves. In practice, a wavefront appears as a combination of the three different forms, yet it can be thought of as a plane wave in most cases since even though a point source generates spherical waves, they eventually behave like plane waves at a target further away from the source as depicted in Fig. 1.6.

Wave propagation. The particles of the medium initially at a steady state, when reached by the wavefront, begin moving back and forth synchronizing with the oscillation of the pressure wave. They transmit the acoustic energy further the propagation direction in a way repeatedly compressing and dilating the elastic medium. The periodicity of particle displacement caused by the cyclic phenomenon is called the wavelength λ, and alternatively the period T can be defined in the sense of time domain (for the illustrative diagram, see Figure. 1.7). These two measures (λ, T) can be associated with

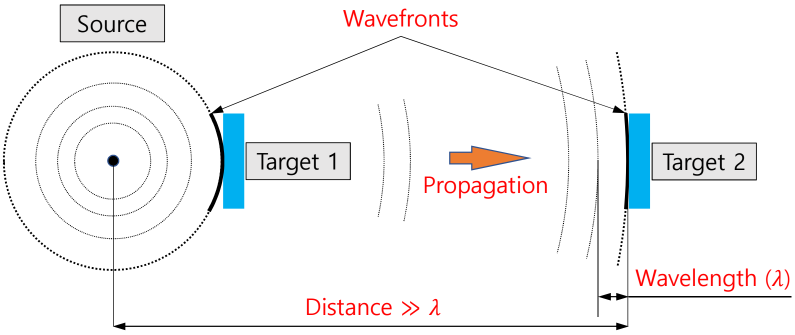

Figure 1.6: The target 1 receives a spherical wave whereas the target 2 located far away from the source experiences nearly a plane wave.

each other by introducing the velocity c to represent the propagation speed of the wave or sound (SOS); $\lambda = cT$ or $c = \lambda f$ from the reciprocal relation between frequency f and T. The SOS ($\boldsymbol{c}$) is also linked to the density ($\boldsymbol{\rho}$) and impedance ($\boldsymbol{Z}$) via the derivation of the wave equation, given the assumption in convention at US system; the support mediums for propagation are homogeneous and perfectly elastic, and thus the amplitude and direction of the initial plane wave are constantly preserved, even though the conditions do not perfectly hold in practice.

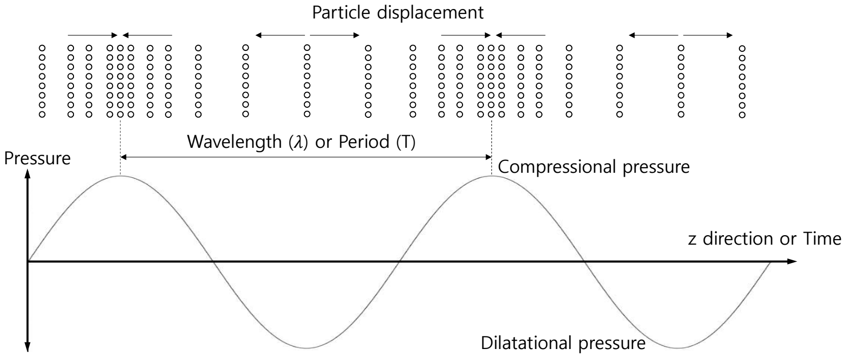

Figure 1.7: Direction of particle vibration is the same as that of wave propagation, and US are purely longitudinal waves.

Propagation equation. The wave equation relative to the direction (z) for US wave to pass through is established by tweaking Newton's second law of motion; the net force ($\sum F$) applied to an object is equivalent to the product of the mass of that object and the acceleration of the object:

$$\frac{\partial K_{zz}}{\partial z} + \frac{\partial K_{yz}}{\partial y} + \frac{\partial K_{xz}}{\partial x} = \boldsymbol{\rho}\frac{\partial^2 W}{\partial^2 t^2} \tag{1.4}$$

where K_{zz} is the stress ($[N/m^2]$) caused by the longitudinal wave, and K_{yz} and K_{xz} are the stresses caused by the shear waves in directions y and x respectively. W is the particle displacement ($[m]$) in the direction z, and t is the time ($[s]$). The shear waves tends to be quickly attenuated and negligible, and thus US wave is reckoned as the purely longitudinal wave. Thus (1.4) boils down to:

$$\frac{\partial K_{zz}}{\partial z} = \boldsymbol{\rho}\frac{\partial^2 W}{\partial t^2} \tag{1.5}$$

K_{zz} is linked to the longitudinal strain (ϵ_{zz}) by involving the constants μ and ν referred as Lamé's first and second parameters which have the same unit ($[N/m^2]$) as the pressure:

$$K_{zz} = (\nu + 2\mu)\epsilon_{zz} \tag{1.6}$$

The strain (ϵ) is the dimensionless constant characterizing the degree of deformation of a medium per unit distance, and in the longitudinal direction is calculated by $\frac{\partial W}{\partial z}$. (1.5) is further rewritten by means of (1.6) and the formula of the strain:

$$\nabla^2 W \overset{(a)}{=} \frac{\boldsymbol{\rho}}{\nu + 2\mu}\frac{\partial^2 W}{\partial t^2} \overset{(b)}{=} \frac{1}{\boldsymbol{c}^2}\frac{\partial^2 W}{\partial t^2} \tag{1.7}$$

where ∇^2 denotes a second order differential operator ($\frac{\partial^2}{\partial x^2}+\frac{\partial^2}{\partial y^2}+\frac{\partial^2}{\partial z^2}$) in three-dimensional space (x, y, z). (a) comes from simply rearranging $\frac{\nu+2\mu}{\partial z}\frac{\partial^2 W}{\partial z}$ acquired by substituting (1.6) in the left-hand side of (1.5), and (b) is accomplished by applying $\Box = \frac{1}{c^2}\frac{\partial^2}{\partial t^2} - \nabla^2$ called the d'Alembertian operator to the effective net displacement W; $\Box W = 0$. From the derivation, the SOS ($\boldsymbol{c}$) can be expressed by the characteristics of a tissue:

$$\boldsymbol{c} = \sqrt{\frac{\nu + 2\mu}{\boldsymbol{\rho}}} \approx \sqrt{\frac{\boldsymbol{K}}{\boldsymbol{\rho}}} \tag{1.8}$$

where $\boldsymbol{K}$ is the bulk modulus (N/m^2) gathering parameters (ν, μ) as $\mathbf{K} = \nu + \frac{2}{3}\mu$. The compressibility ($\boldsymbol{k} = \frac{1}{\boldsymbol{K}}$) as the reciprocal of $\boldsymbol{K}$ is often used. On the other hand, the acoustic impedance ($\boldsymbol{Z}$) represented with the unit of $kg/m^{-2}.s^{-1}$ or Rayleigh determines the amplitude of reflected signal at the interface and is defined by the product of the density ($\boldsymbol{\rho}$) of the medium and the SOS ($\boldsymbol{c}$) in the medium:

$$\mathbf{Z} = \boldsymbol{\rho c} = \sqrt{\boldsymbol{\rho K}} \tag{1.9}$$

where the second equality is led by (1.8). Table 1.1 gives some typical SOS ($\boldsymbol{c}$), acoustic impedance ($\boldsymbol{Z}$) and density ($\boldsymbol{\rho}$), as the features characterizing the properties of the tissues.

Reflection, transmission and refraction at interfaces. The ultimate aim of ultrasonography is to record and analyze the signals returned from interfaces defined as boundaries between two mediums with different acoustic properties. In what follows, based on the underlying physics of US wave, we examine the phenomena occurring as US wave passes through the interfaces. It is consistently supposed that materials are homogeneous, isotropic and perfectly elastic, and that the acoustic energy is propagated along the longitudinal direction forming the plane wave.

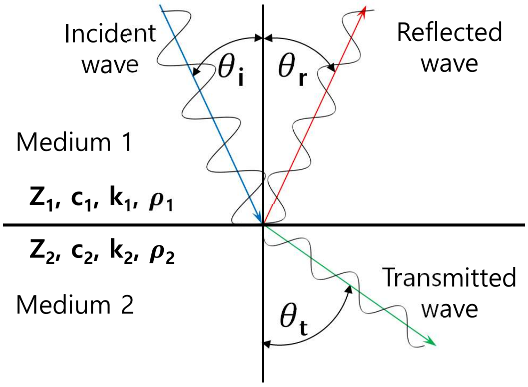

Figure 1.8: The dynamics of wave propagation occurring at the interface is illustrated. θ indicates the angle between the travel path of the plane wave and the normal to the interface, and the subscripts i, r, and t stand for respectively incident, reflected, and transmitted.

As depicted in Fig. 1.8, mediums 1 and 2, having the different acoustical properties ($\boldsymbol{Z}, \boldsymbol{c}, \boldsymbol{k}, \boldsymbol{\rho}$), give rise to the variation of direction and amplitude of the acoustic energy of the incident wave at the interface, in the manner of reflection and transmission. The reflected angle θ_r is identical to the incidence angle θ_i, and the transmitted angle θ_t is determined by the Snell–Descartes law, also known as the law of refraction defined with the SOS ($\boldsymbol{c}_1, \boldsymbol{c}_2$) of each medium and ($\theta_i$) as:

$$\frac{\sin\theta_i}{\boldsymbol{c}_1} = \frac{\sin\theta_r}{\boldsymbol{c}_1} = \frac{\sin\theta_t}{\boldsymbol{c}_2} \tag{1.10}$$

The coefficients of pressure reflection (R) and pressure transmission (T) are computed with the acoustic impedances ($\boldsymbol{Z}_1, \boldsymbol{Z}_2$) of each medium, the angle of incidence (θ_i) and the angle of refraction (θ_t) as follows:

$$R = \frac{P_r}{P_i} = \frac{\boldsymbol{Z}_2\cos\theta_i - \boldsymbol{Z}_1\cos\theta_t}{\boldsymbol{Z}_2\cos\theta_i + \boldsymbol{Z}_1\cos\theta_t}, \quad T = \frac{P_t}{P_i} = \frac{2\boldsymbol{Z}_2\cos\theta_i}{\boldsymbol{Z}_2\cos\theta_i + \boldsymbol{Z}_1\cos\theta_t} \tag{1.11}$$

The relationship can be also expressed using the coefficients of energy reflection α_r and transmission α_t, with $I = \frac{P^2}{2\boldsymbol{Z}}$:

$$\alpha_r = \frac{I_r}{I_i} = \left(\frac{\boldsymbol{Z}_2\cos\theta_i - \boldsymbol{Z}_1\cos\theta_t}{\boldsymbol{Z}_2\cos\theta_i + \boldsymbol{Z}_1\cos\theta_t}\right)^2, \quad \alpha_t = \frac{I_t}{I_i} = \frac{4\boldsymbol{Z}_1\boldsymbol{Z}_2\cos\theta_i}{(\boldsymbol{Z}_2\cos\theta_i + \boldsymbol{Z}_1\cos\theta_t)^2} \tag{1.12}$$

Accordingly if the impedance of medium 2 is negligible compared to that of medium 1, most of energy is reflected, and consequently no US wave is transmitted into the medium 2. For example, this occurs if medium 2 is air. Taking into account such a nature of US, the matching layer of transducer described in section 1.1.1 is devised to maximize the acoustic energy to be transmitted into the skin.

1.2 Quantitative acoustic microscopy

In biology and life science, the microscope is an indispensable tool to broaden our observable limit to the subcellular world. Since the advent of the optical microscope (see Fig. 1.9 (a)) designed by Antony van Leeuwenhoek in the late 17th century which is accredited as the first real microscope, the microscopy has been remarkably advanced to super resolution (PALM, STORM, STED [Schermelleh 2010]) and to 3D imaging (SPIM [Keller 2008]), through the innovation of scanning systems, and the introduction of sophisticated natural principles, *e.g.,* the fluorescence phenomenon. The resolution limit of every microscope is intrinsically subjected to Abbe's law ($d = \frac{\lambda}{2N.A.}$) which states that the resolvable minimum distance is determined by the wavelength and numerical aperture $N.A.$ [Hockin 1884]. Electron microscope (Fig. 1.9 (b)), having much shorter wavelength (0.00389nm for an electron beam of 100 KeV) than those of the visible light (from 750nm to 390nm), is able to provide extremely high resolution, and has been further evolving by combining the advantage of the light microscopy like the correlative Light Electron Microscopy. However, the usefulness of microscopy is not confined to only the capability to demonstrate the superb resolution since it is also arguably beneficial to be able to accurately quantify physical properties of a material in a microscopic level. The quantitative acoustic microscopy (QAM) is used as a method to disclose a histological structure or examine an abnormality of a biological soft tissue in a submicrometer resolution exploiting the fact that physically distinct objects perturb in elastically different ways with respect to the irradiation of US pulses. In what follows, we focus on the mechanical structure, the process of data acquisition, signal processing and biomedical applications of QAM.

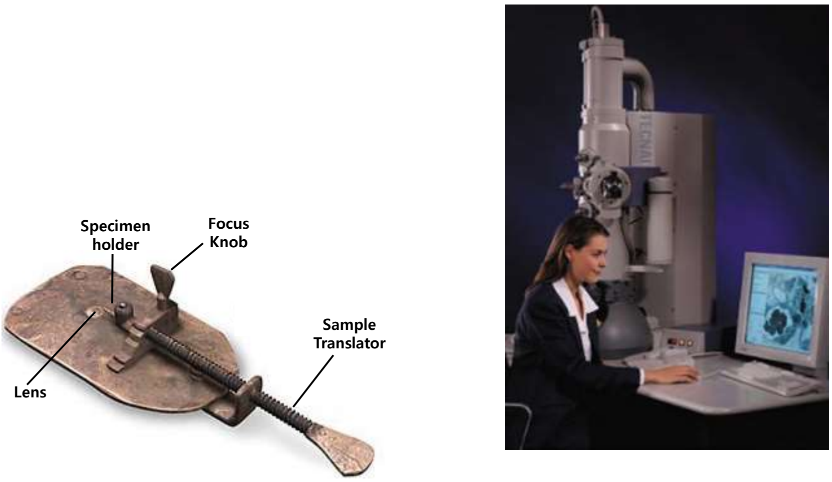

(a) (b)

Figure 1.9: (a) Leeuwenhoek Microscope (circa late 1600s) of hand-held size acknowledged as the first practical microscope [Smith 2010], (b) Transmission Electron Microscopy (TEM) as one of the most advanced types of microscope [Alberts 2007].

1.2.1 The mechanism and principle of QAM

QAM technology exhibited in Fig 1.10 generally attempts to yield an image estimating acoustic parameters from RF signals collected by mechanically scanning a biological tissue through the focused beam in a raster pattern [Lemons 1974, Quate 1979, Johnston 1979]. Hence the contrast of the image is directly associated with the acoustic properties of the tissues, and the outcome from this novel contrast mechanism offers invaluable evidences for quantitative clinical (*i.e.*, histological, anatomical or pathologic) analyses. This subsection briefly addresses the whole gamut of the process from the data acquisition to the image forming.

Working principle. A high-frequency (> 50 MHz), single-element, spherically-focused (*e.g.,* F-number < 1.3) transducer transmits a short US pulse and receives the RF echo signal reflected from the sample which consists of a thin section of soft tissue affixed to a microscopy slide. This single operation is repeated point-by-point by raster scanning with an transducer-dependent increment (*i.e.,* a fixed spatial interval) until entirely covering the specimen mounted on the QAM system in the upside down configuration (see the left bottom of Fig 1.10). In other words, high frequency transducers contribute to the enhancement of the spatial resolution permitting the dense scanning with a tiny step size of the motor stage in Fig. 1.10. The recent QAM studies pursue the fine resolution images by means of high frequency transducers (250 MHz with 2 µm scan increment [Mamou 2015a] or 500 MHz with 1 µm scan increment [Rohrbach 2017]), the acoustic lens of which is also a key component to determine the quality of an image by implementing a favorable focal zone *i.e.,* focal depth and focused diameter.

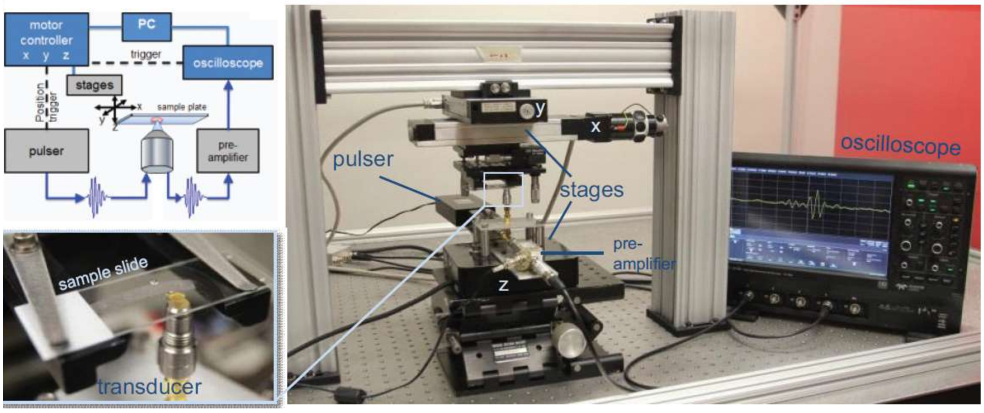

Figure 1.10: The block diagram on the left top position describes the working process of QAM system, and the left bottom photograph provides the closer view of the transducer and the sample in the photograph of the right side showing the whole QAM system [Mamou 2015b].

Meanwhile, the rim echo occurring around the edge of the lens generates an intense unfocused signal and consequently degrades the resulting image. Usually, to mitigate the undesirable effect, lenses with long focal length are adopted. But in this way, the received echo is likely to suffer from poor signal to noise ratio (SNR) caused by high frequency attenuation, which makes the fine resolution approach unfeasible. As a solution to circumvent this drawback, the fabrication of a customized lens is detailed in [Rohrbach 2017].
The cartoon in Fig 1.11(a) illustrates the individual components of a typical QAM transducer and the focused beam being generated from the acoustic lens covered with a matching layer.

QAM RF signals. As depicted in Fig. 1.11(a), the received RF signal consists of two main reflections, *i.e.,* h_1 and h_2 due to respectively the water-tissue and tissue-glass interfaces, which can be reckoned as the sum of two time-delayed, amplitude-decayed and frequency-dependent attenuated versions of the reference RF pulse h_0 obtained from a region devoid of sample presenting only one water-glass interface. The interactions between US waves and mediums are clearly visualized in Fig. 1.11(b) plotting the QAM RF signals recorded in time domain; the blue continuous line corresponds to the sum of two echoes (h_1, h_2) affected by the existence of the tissue, while the red dotted line describing the (h_0) made up of a single pulse. This observation on the physical phenomena arising from the interfaces allows one to build an explicit formula to express

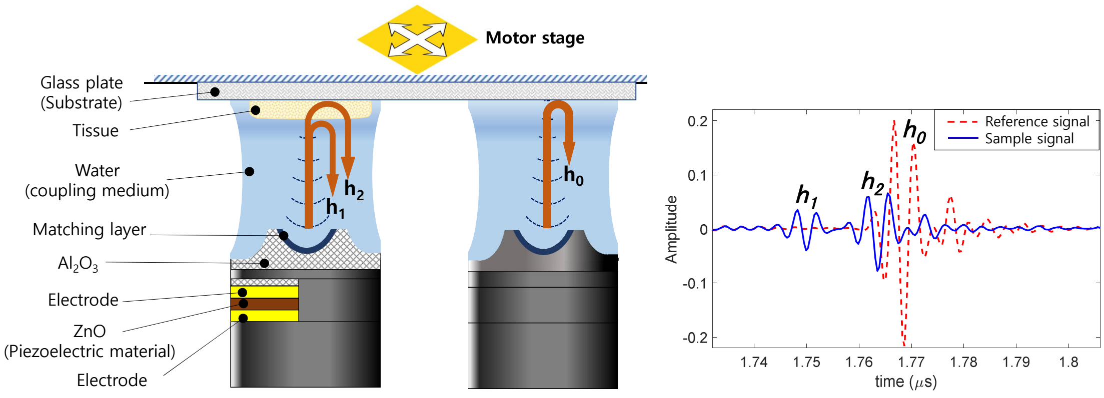

(a)

(b)

Figure 1.11: (a) The cartoon describes the structure of transducer and the process of data acquisition, (b) Reflected signals acquired by 250MHz transducer.

QAM RF signal using only the reference signal (h_0) as follows:

$$\begin{aligned} h(t) &= h_1(t) + h_2(t) \\ &= a_1 h_0(t - t_1) + a_2 h_0^{(*)}(t - t_2), \end{aligned} \tag{1.13}$$

where $a_{1,2}$ and $t_{1,2}$ respectively denote amplitude decays and time delays. Moreover, due to a round trip flight inside the sample, h_2 undergoes an additional effect of linear frequency dependent attenuation symbolized by the superscript $(*)$. The second equality of (1.13) paves the way for introducing the Finite Rate of Innovation (FRI) sampling and reconstruction in QAM imaging, as will be profoundly studied in Chapter 4.

Acoustic parameters. At each scan location, the RF data is digitized, saved, and processed offline to ultimately estimate the acoustic parameters: SOS ($\boldsymbol{c}$), acoustic impedance ($\boldsymbol{Z}$) or attenuation coefficient ($\boldsymbol{\alpha}$). In the previous sections, it was witnessed that the acoustic parameters mentioned above are independently defined from each other, and thus each parameter estimation enables to investigate the specimen in various medical perspectives by presenting its unique contrast. The following subsection exhibits the experimental results demonstrating that the parametric two-dimensional (2D) maps obtained by the QAM system can quantitatively characterize the elastic properties of biological soft tissues. Prior to observing the resulting images, we offer a brief insight about the parametric image forming recently established in [Rohrbach 2018] for achieving more advanced parameter estimation than the existing Hozumi model [Hozumi 2004]. The ratio between the Fourier transforms of the sample signal (h) and the reference signal (h_0) is computed, and fit to a forward model to estimate the time lags of h_1 and h_2

with respect to h_0. These time differences are exploited to determine $\boldsymbol{c}$ and the tissue thickness d corresponding to the scanned location of the sample. The forward model fit also provides the amplitude of h_1, which is used to estimate $\boldsymbol{Z}$ in the sample. Finally, $\boldsymbol{\alpha}$ is obtained from the previously estimated time delay of h_2 and d.

$$\boldsymbol{c} = c_w \frac{\mathrm{imag}(\log(\lambda_1))}{\mathrm{imag}(\log(\lambda_1)) + \mathrm{imag}(\log(\lambda_2))} \tag{1.14}$$

$$\boldsymbol{\alpha} = \frac{\mathrm{real}(\log(\lambda_2))}{2d\Delta f} \tag{1.15}$$

$$d = \frac{c_w}{2} \frac{\mathrm{imag}(\log(\lambda_1))}{\Delta f} \tag{1.16}$$

$$\boldsymbol{Z} = Z_w \frac{1 + \frac{a_1}{R_{wg}}}{1 - \frac{a_1}{R_{wg}}} \tag{1.17}$$

More details about the notations in the formulae and computation of these acoustic parameters are given in Chapter 4.

1.2.2 Examination of soft tissue in ex-vivo with QAM

Fig. 1.12 shows QAM 2D maps of the same tissues in a human lymph node in three acoustic parameter modes, each of which is determined by two different parameter estimators [Hozumi 2004, Rohrbach 2018]. This figure demonstrates that the QAM parametric 2D-maps show different contrasts depending on the choice of acoustic parameters, and the image quality is affected by the performance of parameter estimators.

1.3 Open challenges and motivation of this thesis

Currently, QAM requires a complete 2D raster scan of the sample to form images, and thus yields a large amount of RF data cube when using conventional spatial and temporal sampling methods, particularly in accordance with the requirement for the fine resolution image. For instance, given the operating configuration where an area of 1 mm^2 is scanned with an imaging system having the 250 MHz of center frequency and the 6-dB bandwidth of 300 MHz, each RF signal is sampled at 2.5 GHz every scan step-size of 2 µm, and the resulting RF data cube is made up of 501 × 501 × 200 RF samples [Rohrbach 2015b]. As a consequence, this arouses a number of practical issues, such as the cost and the complexity of the A/D converters and other fast electronic components. Also the three dimensional dataset enormously expanded might impose a burden on the signal post processing for the parameter estimation. On the other hand, the scanning time is directly dependent on the sample size and can range from less than one minute to possibly tens of minutes. Taking into account a thin sectioned tissue sensitive to the temperature variations in the coupling medium, the scanning time can greatly effect SOS estimates. Accordingly, it is imperative to maintain constant experimental conditions for

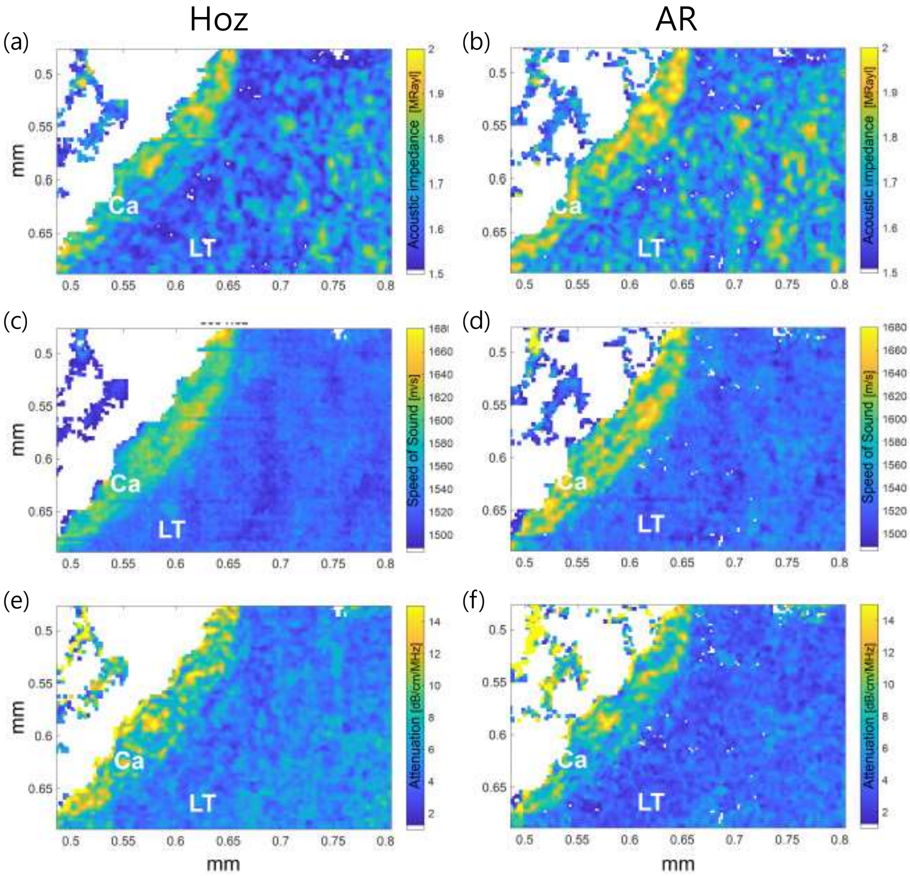

Figure 1.12: The left column (a,c,e) of the figure illustrates the acoustic parameter maps ($\boldsymbol{Z}$, $\boldsymbol{c}$ and $\boldsymbol{\alpha}$ from the first row) estimated using the Hozumi model [Hozumi 2004], whereas the right column (b, d, f) corresponds to the acoustic parameter maps ($\boldsymbol{Z}$, $\boldsymbol{c}$ and $\boldsymbol{\alpha}$ from the first row) estimated using the AR model [Rohrbach 2018]. The abbreviation (ca) and (LT) in the maps respectively stand for *capsule* and *Lymphocyte* tissue in a human lymph node.

ensuring the reliability of the imaging modality, and it should be indeed a worthwhile challenge to revolutionize the traditional data acquisition manner to reduce both the scanning time and the data amount.

In this regard, we pay our attention to the property of the QAM data that many naturally occurring signals and images like QAM 2D maps have a sparse representation in certain transform domains [Candès 2006a], and QAM RF signals can be characterized as a parametric model [Rohrbach 2018]. These two key factors motivated us to take advantage of Compressed Sensing (CS) [Donoho 2006b] and Finite Rate of Innovation (FRI) [Vetterli 2002] framework as a breakthrough able to overcome the challenges stated above. Nevertheless, there is a catch that measurement matrices typically used in the CS framework are impractical to the QAM scanning system. This is due to the use of random sampling schemes which are not feasible in practice. As well as, existing parameter estimators adopted in the FRI studies do not serve as appropriate solvers for the problem setting of the QAM RF signals due to an additional unknown parameter, *i.e.*, frequency attenuation coefficients. Chapters 3, 4 and 5 of this thesis are devoted to the development of the solutions to the problems, and further details about the contributions of the thesis are presented in the following section.

1.4 Contribution and outline

1.4.1 Contributions

The objective of this thesis is to propose novel approaches to tackle the current challenges described in Section 1.3. These contributions are listed below.

1. We proposed novel techniques for QAM data sampling in spatial domain with the objective of reducing both acquisition time and the amount of samples required. Our goal was supported by choosing compressive sampling (CS) measurement matrices that meet CS requirements, and simultaneously take into account the constraints imposed by the design of current experimental QAM systems. For image reconstruction, we designed and tested a wavelet domain AMP-based approach, which exploits underlying data statistics through the use of a Cauchy-based MAP (maximum a posteriori) algorithm. The spiral scanning approach could be implemented on cheap and potentially less precise servo motors, which implicates that QAM systems would be lower costs and simpler to use.

2. The second contribution of this work consists in combining a low rate RF signal sampling procedure with an AR model-based parametric acoustic map reconstruction in QAM imaging. The FRI-based AR approach leads to reconstructing accurate acoustic maps from a markedly reduced number of samples, since the QAM RF signals are defined as a parametric model with a limited number of degrees of freedom: the amplitude decays, time delays and frequency-dependent attenuation coefficients. Thus it would allow the use of much slower A/D cards than those currently used. This would drastically reduce costs, and leads to easy manufacturing of such systems and also increased data quality and lower sensitivity to noise.

3. Finally, we provided the solution for spatio-temporally implementing the undersampling in QAM data acquisition process by combining the spatial CS framework with FRI-based temporal approach. The simulation results showed huge potential of our approach proposed to cope with the current issues.

1.4.2 Thesis outline

This thesis is structured as follows. Chapter 2 presents the necessary theoretical background behind the undersampling measurements in spatial domain and the innovation rate sampling in temporal domain. In the first section assigned to CS framework, the properties of transform domains will be explained focusing on the ability to extract the sparse representation of natural images, together with incoherence relationship with the measurement bases, followed by the exploration of recovery strategies. The second section of the chapter provides the overview of FRI scheme well related to the parametric model of QAM RF signals in time domain. Chapter 3 introduces the derivation of the wavelet-based Cauchy denoiser and, three practical sensing patterns adopted for QAM data acquisition. The performance of the proposed approach is evaluated through the comparison with those of existing CS reconstruction techniques. In Chapter 4, the problem formulation for associating FRI framework with QAM RF signals is elaborated, which is linked to autoregressive (AR) inverse model to estimate acoustic parameters. Simulation results are presented with quantitative assessments of the acoustic parameter maps reconstructed by the FRI-based AR estimator. Chapter 5 combines the two separated sparse sampling schemes proposed in the previous chapters. The results demonstrate that combining both CS and FRI theory contributes to the significant reduction of the scanning time and the size of the QAM data cube. Finally, conclusive remarks and perspectives are reported, and possible future work directions are detailed in Chapter 6.

Chapter 2

State-of-the-art

Contents

This second chapter focuses on describing compressive sampling (CS) and finite rate of innovation (FRI), two frameworks that will play a pivot role throughout this thesis. From a practical viewpoint, CS is used in this work to decrease the amount of acquired data and the acquisition time in the spatial domain. Its fundamental theories and the state of the art methods for encoding and decoding are reported in this chapter. Furthermore, the main principles of FRI are provided, which are the basis of the proposed methodology to decrease the number of temporal samples acquired in QAM. General FRI background is presented, and prototypical parametric model-based signals are discussed. Finally, in the last section of this chapter we conclude by highlighting the significance of these frameworks as the novel paradigm to revolutionize the conventional data acquisition manner in QAM systems.

2.1 Compressed sensing

The key idea of CS is that many real-world signals and images can be faithfully reconstructed from by far lower number of transform coefficients than the original number of samples (*i.e.* acquired according to Nyquist–Shannon sampling theorem) [Donoho 2006b, Candès 2008]. Inspired by this attractive hypothesis, CS has been vigorously studied as an approach to decrease the amount of data and to accelerate the acquisition process at potentially no cost of image quality. Hereafter we recall the insight of CS framework based on its underlying theories, and subsequently address sensing modalities and recovery schemes. In particular, we intensively focus on the characteristics of Approximate Message Passing (AMP) algorithm due to the strikingly fast and accurate recovery performance compared with its counterparts.

2.1.1 Overview of CS

CS is based on measuring a dramatically reduced number of samples than what is dictated by the Nyquist–Shannon theory [Shannon 1984]. Given a signal or an image, the traditional transform-based compression method performs the following steps: (i) acquires all N samples complying with the sampling theorem, (ii) computes a complete set of transform coefficients (*e.g.*, DCT or wavelet), (iii) selectively quantizes and encodes only the $K \ll N$ most significant coefficients. This procedure is highly inefficient since the majority of the output of the analogue-to-digital conversion (ADC) process ends up with being discarded. CS is concerned with sampling signals more parsimoniously, acquiring only the relevant signal information rather than sampling followed by compression. The main hallmark of this methodology is that, given a sparse or compressible signal, a small number of linear projections of an input data directly acquired contains sufficient information to effectively carry out the processing of interest (signal reconstruction, detection, classification, etc).

In terms of signal approximation, the authors in [Candès 2006a, Donoho 2006b] have demonstrated that if a signal is K-sparse in one basis (meaning that the signal is exactly or approximately represented by K components of this basis), then it can be recovered

from $M = cst \cdot K \cdot \log(N/K) \ll N$ fixed (non-adaptive) linear projections onto a second basis called the measurement basis, where $cst > 1$ is a small overmeasuring constant. The related essential theories underpinning the former formula, *i.e.,* sparsity, incoherence, and restricted isometric property (RIP) will be recalled in Section 2.1.2.
The CS measurement model is as follows:

$$\mathbf{y} = \mathbf{\Phi}\mathbf{x} + \mathbf{n}, \tag{2.1}$$

where $\mathbf{y} \in \mathbb{R}^M$ is the observation or measurement vector, $\mathbf{x} \in \mathbb{R}^N$ is the signal to be reconstructed, $\mathbf{\Phi} \in \mathbb{R}^{M \times N}$ is the sensing matrix leading an underdetermined linear system, *i.e.*, $M \ll N$, and $\mathbf{n} \in \mathbb{R}^M$ is an additive white Gaussian noise. As stated previously, recovering $\mathbf{x}$ from $\mathbf{y}$ is possible due to the sparse property of $\mathbf{x}$ in a given basis, *i.e.*, $\mathbf{x} = \mathbf{\Psi}\mathbf{s}$, where $\mathbf{s}$ is a K-sparse vector having only K components different from zero. The majority of recovery approaches solve constrained optimization problems. Commonly used approaches are based on convex relaxation (Basis Pursuit [Emmanuel 2004]), non-convex optimization (re-weighted l_p minimization [Chartrand 2008]) or greedy strategies (Orthogonal Matching Pursuit (OMP) [Tropp 2007]). On the other hand, alternative algorithms such as iterative thresholding approaches [Daubechies 2004, Beck 2009] have attracted intense interest, owing to faster reconstruction than what can be done by convex optimization. The authors in [Herrity 2006, Blumensath 2009] proved that correct solutions could be obtained via soft or hard thresholding of observations measured from sparse signals. However in spite of the low computational complexity, such fast iterative thresholding methods show considerably worse sparsity-undersampling tradeoff than the one achieved by basis pursuit [Maleki 2009]. As a relatively recent achievement to satisfy both aspects simultaneously, [Donoho 2010] proposed AMP algorithm that is detailed in Section 2.1.5.

2.1.2 Theory and premise

CS success is conditioned on the choice of the sensing procedure and the use of non-linear recovery algorithms, which is only possible given the sparsity of the signal under consideration and the incoherence of sensing modality [Candès 2008]. We herein delve into these prerequisites.

2.1.2.1 Sparsity

Most signals and images present in nature can faithfully express the underlying information with small number of nonzero values in an appropriate transform domain (including identity matrices in the case of naturally sparse signals or images), which is referred to as sparsity and has the following mathematical implication:

$$x_n = \sum_{i=1}^{N} s_i \psi_{i,n} \tag{2.2}$$

where $\mathbf{\Psi} = [\psi_1, \psi_2, \ldots, \psi_N]$ is a set of certain sparsifying bases able to fully represent $\mathbf{x}$, and could be a known basis such as wavelet, Fourier, curvelet or wave atoms transform that have been widely exploited in the literature due to the robust sparsifying ability and fast implementation [Candès 2005, Candes 2006b, Candès 2008, Mallat 1999]. It implies that if all entries of the vector $\mathbf{s} \in \mathbb{R}^N$ but K largest values are equal to or close to zero, the signal is called K-sparse and can be approximated with K nonzero values as follows:

$$\hat{x}_n = \sum_{j=1}^{K} s_j \psi_{j,n} \tag{2.3}$$

Given the expressions of (2.2) and (2.3) based on the definition of sparsity, it is arguable that the error $||\mathbf{x} - \hat{\mathbf{x}}||_2$ could be negligible.
Fig. 2.1 illustrates this argument. Fig. 2.1 (c) was reconstructed with only the 5% largest coefficients in the wavelet transform (Haar wavelet, three levels) of Fig. 2.1 (a) of the original images with 537 × 358 pixels, yet the loss of salient information is not noticeable. Fig. 2.1 (b) depicts the wavelet coefficients of Fig. 2.1 (a) sorted with the descending order of magnitude, and all of coefficients are nearly zero after the symbol $*$ indicating the 5% of total amount of coefficients.

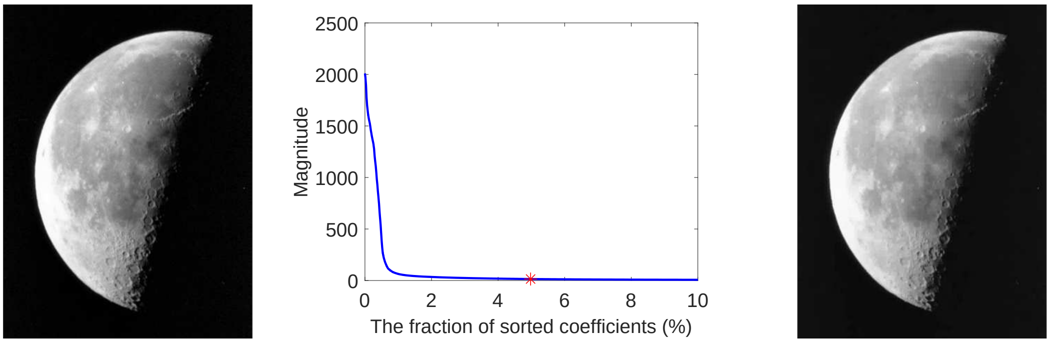

(a) (b) (c)

Figure 2.1: (a) The original image with 537 × 358 pixels. (b) The sorted magnitudes of wavelet coefficients show a steep decay, and the large fraction of coefficients are nearly zero. (c) The image is acquired by the inverse wavelet transform after setting all wavelet coefficient of (a) but the 5% largest (marked with $*$ in (b)) to zero using hard thresholding.

Relying on the characteristic of signals or images, the most relevant sparsifying basis can be chosen among the known transform bases exemplified above.
In the previous work [Kim 2016], we compared the sparsifying capability with respect to US images among three different domains (Time, DCT and wavelet domain), and confirmed that an effective sparse representation has a significant influence on the recovery quality in the CS framework. In Chapter 3, we will seek the enhancement of the

recovery performance by introducing the most compatible sparse signal estimator with wavelet domain.

2.1.2.2 Incoherence

In the previous section, it was shown that there exist appropriate sparse representations for any signal or image, and thus (2.1) also can be written as follows:

$$\mathbf{y} = \mathbf{\Phi} \underbrace{\mathbf{\Psi s}}_{\mathbf{x}} + \mathbf{n}, \tag{2.4}$$

where $\mathbf{\Psi}$ denotes a representation domain letting the signal of interest $\mathbf{x}$ be transformed to a sparse sequence of $\mathbf{s}$ as shown in (2.2), for which commonly orthogonal bases are used in most of the applications. In accordance with the introduction of the new basis, CS needs to regulate the relationship of the two set of bases $(\mathbf{\Phi}, \mathbf{\Psi})$, which is achieved by introducing the measure of the incoherence.

In the CS context, the coherence is rephrased as measuring the largest correlation between any two elements taken from the first $(\mathbf{\Phi})$ and second basis $(\mathbf{\Psi})$. Accordingly, if $\mathbf{\Phi}$ and $\mathbf{\Psi}$ contain correlated elements, the coherence is large, and vice versa. The coherence measurement between the two bases is given by [Donoho 2001, Candès 2008]:

$$\mu(\mathbf{\Phi}, \mathbf{\Psi}) = \sqrt{N} \cdot \max_{1 \leq k, i \leq N} |\langle \varphi_k, \psi_j \rangle| \tag{2.5}$$

where $\langle \varphi_k, \psi_j \rangle$ represents the inner product between k-th and j-th column vectors of $\mathbf{\Phi}$ and $\mathbf{\Psi}$ respectively. One may obtain the intuition for the formula (2.5) from the example that given a pair $(\mathbf{\Phi}, \mathbf{\Psi})$ of orthonormal bases of $\mathbb{R}^N$, the measure μ is compactly confined to $[1, \sqrt{N}]$.

CS is generally concerned with low coherence, and the extreme example having a perfect incoherence, namely $\mu(\mathbf{\Phi}, \mathbf{\Psi}) = 1$, is found for the pair of the Dirac delta function $\varphi_k(t) = \delta(t - k)$ and Fourier transform function $\psi_i(t) = \frac{1}{\sqrt{N}} e^{j2\pi it/N}$ [Candès 2008]. Aside from that, noiselets also reveals low coherence with many filters used in wavelet decomposition irrespective of sample size N, such as $\sqrt{2}$ with Haar wavelets, 2.2 with Daubechies D4 and 2.9 with Daubechies D8. Finally, sensing matrices based on randomness, like Gaussian following a normal distribution or Bernoulli consisting of ± 1 binary entries, proved to have low coherence with any fixed basis attaining $\mu \approx \sqrt{2\log N}$ with high probability. Therefore, when it comes to the design of sensing system, a random measurement matrix $\mathbf{\Phi}$ can be universally adopted without considering the structure of a representation basis $\mathbf{\Psi}$, and such property is called the universality.

The aforementioned two random-based measurements will be tested as a sensing modality for the undersampling of QAM in Chapter 3.

2.1.2.3 Sparse signal recovery

Searching for the sparsest solution to underdetermined systems ($M \ll N$) of linear equations is equivalent to solving the ℓ_0-minimization problem:

$$(P_0) \quad \min_{\tilde{\mathbf{s}} \in \mathbb{R}^N} \|\tilde{\mathbf{s}}\|_0 \quad \text{subject to} \quad \mathbf{y} = \boldsymbol{\Theta}\tilde{\mathbf{s}}, \quad \boldsymbol{\Theta} = \boldsymbol{\Phi}\boldsymbol{\Psi} \tag{2.6}$$

where $\|\cdot\|_0$ indicates the total number of nonzero elements in a vector.
Indeed, the problem in (2.6) is NP-hard [Donoho 2006a, Natarajan 1995] and intractable since it requires exhaustive searches for over all subsets of columns of $\boldsymbol{\Theta}$. Furthermore, as far as a large-scale signal is concerned, the procedure clearly is combinatorial, and consequently the complexity increases exponentially. Hence, the relaxation to ℓ_1-norm known as Basis Pursuit (BP) [Chen 2001, Candès 2005] is generally used within CS reconstruction, turning into optimization problems; ℓ_1 norm is convex unlike ℓ_0 norm requiring to enumerate non-zero coordinates:

$$(P_1) \quad \min_{\tilde{\mathbf{s}} \in \mathbb{R}^N} \|\tilde{\mathbf{s}}\|_1 \quad \text{subject to} \quad \mathbf{y} = \boldsymbol{\Theta}\tilde{\mathbf{s}}, \quad \boldsymbol{\Theta} = \boldsymbol{\Phi}\boldsymbol{\Psi} \tag{2.7}$$

where $\|\cdot\|_1$ indicates the summation of the absolute values of elements.
As a condition for (P_1) to accomplish the successful recovery, **Theorem 1** in [Candès 2007b] remarks that if, for some positive constant C, M measurements selected randomly in $\boldsymbol{\Phi}$ domain obey:

$$M \geq C \cdot \mu^2(\boldsymbol{\Phi}, \boldsymbol{\Psi}) \cdot K \cdot \log N, \tag{2.8}$$

a K-sparse signal of $\mathbb{R}^N$ in basis $\boldsymbol{\Psi}$ is exactly found by solving (P_1) with overwhelming probability. From the formula of (2.8), one may also observe the significance of incoherence that the smaller μ, the fewer measurements are needed.
Nevertheless, (2.7) only takes into account the noiseless scenario unlike (2.4), and thus we will deal with more general case considering noise effect in the forthcoming subsection.

2.1.2.4 Restricted Isometry Property

In practice, the data acquisition process necessarily entails noise effects due to various reasons, *e.g.*, quantization error. Therefore, in general our interest is in dealing with the noisy setting (2.4), and it turns out that the optimal solution to the corresponding problem is found by solving the ℓ_1 norm minimization with relaxed constraints well known as LASSO named after Leasst Absolute Shrinkage and Selection Operator [Tibshirani 1996, Candès 2008]:

$$(P_2) \quad \min_{\tilde{\mathbf{s}} \in \mathbb{R}^N} \|\tilde{\mathbf{s}}\|_1 \quad \text{subject to} \quad \|\mathbf{y} - \boldsymbol{\Theta}\tilde{\mathbf{s}}\|_2 \leq \boldsymbol{\epsilon}, \quad \boldsymbol{\Theta} = \boldsymbol{\Phi}\boldsymbol{\Psi} \tag{2.9}$$

where $\|\cdot\|_2$ is the Euclidean distance ($:= \sqrt{\sum_i \cdot_i^2}$) of a vector, and $\boldsymbol{\epsilon}$ bounds the amount of noise in the measurements [Candès 2008].
As a method to evaluate the reconstruction fidelity, [Candès 2005, Baraniuk 2008, Candès 2006a] proposed the restricted isometry property (RIP), which also allows to study the general robustness of CS given by [Candès 2005]:

$$(1-\delta_K)\|\mathbf{s}\|_2^2 \leq \|\boldsymbol{\Theta}\mathbf{s}\|_2^2 \leq (1+\delta_K)\|\mathbf{s}\|_2^2 \tag{2.10}$$

where δ_K is the isometry constant of a measurement matrix $\boldsymbol{\Theta}$ defined as the smallest number for each integer $K = 1, 2, \ldots$, which holds for all K-sparse vector $\mathbf{s}$. We say that given $\delta_K \in (0, 1)$, a matrix $\boldsymbol{\Theta}$ obeys RIP of order K. This statement implies that if δ_K is equal to zero in an extreme case, the Euclidean norm of K-sparse vector is intactly preserved in the measurement; in that case, $\boldsymbol{\Theta}$ should be an orthogonal matrix, namely square matrix. However the CS measurement is supposed to hire inherently a short or fat matrix, *i.e.*, $\mathbb{R}^{M\times N}$ ($M \ll N$). Thus, RIP postulates an approximately orthogonal matrix for $\boldsymbol{\Theta}$, and correspondingly the equivalent description for a matrix to obey RIP is introduced; all subsets of K columns taken from $\boldsymbol{\Theta}$ are nearly orthogonal.
In order to recover an unique K-sparse vector from compressive measurements, one wants to guarantee that all pairwise distances between K-sparse vectors must be well preserved in the measurement space, like when they are in the original vector space. This concept is formulated as follows [Candès 2008]:

$$(1-\delta_{2K})\|\mathbf{s}_1-\mathbf{s}_2\|_2^2 \leq \|\boldsymbol{\Theta}\mathbf{s}_1-\boldsymbol{\Theta}\mathbf{s}_2\|_2^2 \leq (1+\delta_{2K})\|\mathbf{s}_1-\mathbf{s}_2\|_2^2 \tag{2.11}$$

If δ_{2k} is sufficiently lower than 1, one can design recovery algorithms able to discriminate all K-sparse vectors from compressive measurements, which indicates the implication of RIP regarding CS.
If the RIP holds for $\delta_{2K} < \sqrt{2}-1$, (P_1) problem achieves an accurate reconstruction [Candes 2006b, Candès 2008, Cohen 2009], whose solution $\mathbf{s}^*$ obeys the following **Theorem 2** in [Candès 2007a]:

$$\|\mathbf{s}^*-\mathbf{s}\|_2 \leq C_0\cdot\|\mathbf{s}-\mathbf{s}_K\|_1/\sqrt{K} \quad \text{and} \quad \|\mathbf{s}^*-\mathbf{s}\|_1 \leq C_0\cdot\|\mathbf{s}-\mathbf{s}_K\|_1 \tag{2.12}$$

where C_0 is some constant, and $\mathbf{s}_K$ is the vector $\mathbf{s}$ with all but the K largest components set to 0 [Candès 2007a]. Theorem 2 offers stronger conclusions than those of Theorem 1 in (2.8). If $\mathbf{s}$ is K-sparse, $\mathbf{s} = \mathbf{s}_K$ and thus the solution $\mathbf{s}^*$ to (P_1) is exact.
On the other hand, in the case of noisy scenario when the RIP holds for $\delta_{2K} < \sqrt{2}-1$, the solution $\mathbf{s}^*$ to (P_2) obeys the following **Theorem 3** [Candès 2007a]:

$$\|\mathbf{s}^*-\mathbf{s}\|_2 \leq C_0\cdot\|\mathbf{s}-\mathbf{s}_K\|_1/\sqrt{K} + C_1\cdot\boldsymbol{\epsilon} \tag{2.13}$$

where C_0 and C_1 are some constants. This shows that the reconstruction error is proportional to the noise level of data.

2.1.3 Sensing matrices

When it comes to a successful CS recovery in the sense of RIP, one wants to find the matrices with the property that column vectors taken from arbitrary subsets are nearly orthogonal, and thus it is intuitive that the larger subsets are better. In this regard, Candès *et al.* considered the following family of sensing matrices built on randomness [Candès 2008]:

(1) form $\mathbf{\Phi}$ by sampling N column vectors uniformly at random on the unit sphere of $\mathbb{R}^M$,

(2) form $\mathbf{\Phi}$ by sampling independent and identically distributed (i.i.d.) entries from the normal distribution $\sim \mathcal{N}\left(0, \frac{1}{M}\right)$ [Candes 2004],

(3) form $\mathbf{\Phi}$ by sampling a random projection $\mathbf{P}$ as in “Incoherent Sampling” and normalize: $\mathbf{\Phi} = \sqrt{\frac{N}{M}}\mathbf{P}$,

(4) form $\mathbf{\Phi}$ by sampling i.i.d. entries from a symmetric Bernoulli distribution ($P(\phi_{i,j} = \pm\sqrt{M}) = \frac{1}{2}$) or other sub-Gaussian distribution [Baraniuk 2008, Mendelson 2008].

All these matrices satisfy RIP with overwhelming probability, provided that the following condition holds:

$$M \geq C \cdot K \log(N/K) \tag{2.14}$$

where C is some constant varying with each instance (1)-(4) enumerated above. (2.14) reveals how RIP is linked to CS defining the relationship between the sparsity K and the amount of measurement M as glimpsed in Section 2.1.1.

We hereby learned that random matrices formed following incoherence and RIP can guarantee stable and accurate reconstruction of sparse or approximately sparse signals from dramatically undersampled measurements bounded by (2.8), (2.14).

However, even though the random matrices are underpinned by the well-established theories, it is apparent that considering particularly large-scale setup, it could pose impractical issues such as high computational complexity or huge memory buffering. As the alternatives to take the compromise between the computational efficiency (fast recovery) and randomness (exact recovery), the class of structured random matrices and their performance are studied in [Rauhut 2010].

On the other hand, one needs to pay attention to the specificity of the CS measurement problem that will arise being applied to the QAM system; QAM motor stage for a raster scanning should be consecutively operated from a point to the adjacent point with an uniform step size (see Fig. 1.10). Therefore, it is essential to develop a dedicated sensing manner under consideration of this particular mechanism. In Chapter 3, we propose the undersampling scanning patterns motivated by Bernoulli trial process.

2.1.4 Sparse recovery algorithms

As mentioned previously, the ideal pair of encoding and decoding for CS framework, finding an unique sparse vector ($\mathbf{s}$) from an incomplete information ($\mathbf{y}$), lies in a random-based sensing followed by a recovery using (P_1) or (P_2) classified as a linear program (LP) [Powell 1984]. Also, on the purpose of improving the recovery accuracy, the LP idea has inspired the development of many derivatives such as ℓ_1-magic [Candès 2007c] or ℓ_1-ls [Kim 2007]. However, these approaches do not exploit the true statistical distribution of the data, and are motivated by the inability of the classical least-squares approach to estimate the reconstructed signal. Moreover, in terms of a large scale problem in most practical cases, the LP based algorithms suffer from enormously expensive complexity of $\mathcal{O}(N^3)$ [Qaisar 2013]. Consequently, the main contribution of these recovery schemes is to a benchmark for evaluating the performance of brand new sparse recovery algorithms. In the subsection, we review and examine various existing algorithms developed to overcome the limitation of the LP in fast, accurate or stable aspects.

2.1.4.1 Iteratively Reweighted Least Squares (IRLS)

$\mathcal{S}\alpha\mathcal{S}$-IRLS [Achim 2010] is one of the examples achieving the enhancement of the reconstruction quality by taking advantage of actual statistics of US data. It was inspired by [Chartrand 2008, Tsaig 2006] which is based on ℓ_p norm optimization approach (2.15) approximating the ideal ℓ_0 case with $p < 1$.

$$\min_{\tilde{\mathbf{s}}\in\mathbb{R}^N} \|\tilde{\mathbf{s}}\|_p \quad \text{subject to} \quad \mathbf{y} = \boldsymbol{\Theta}\tilde{\mathbf{s}} \tag{2.15}$$

The ultimate goal of the work is to find the optimal p to satisfy (2.15), and the novelty of [Achim 2010] is to relate the optimum value of p to the statistics of US data, as detailed in the following sentences.

When it comes to US image formation, RF echoes have been commonly assumed to follow Gaussianity until [Kutay 2001] showed that RF echoes can be more exactly characterized as a power-law shot noise model. The discovery can be further associated with alpha-stable distribution [Petropulu 2000]. Particularly, when its characteristic function follows (2.16), random variables are called symmetric α stable ($\mathcal{S}\alpha\mathcal{S}$):

$$\varphi(\omega) = \exp(j\delta\omega - \gamma|\omega|^{\alpha}) \tag{2.16}$$

where α denotes the characteristic exponent ranging from 0 to 2, and a location parameter $\delta(-\infty < \delta < \infty)$ becomes the mean of $\mathcal{S}\alpha\mathcal{S}$ distribution if α belongs to the interval $(1, 2]$. Otherwise, (*i.e.*, for $0 < \alpha \leq 1$) δ is the median of the distribution. $\gamma(\gamma > 0)$, determining the spread of the distribution, is analogous to the variance of Gaussian distribution.

$\mathcal{S}\alpha\mathcal{S}$-IRLS utilizes α in (2.16) to find the optimum value of p with which the ℓ_p-norm minimization (2.15) is solved using iteratively reweighted least squares approach (IRLS)

[Lawson 1961, Beaton 1974]. The simulation results demonstrated that the images recovered with this method have much more improved PSNR than those of BP and Orthogonal Matching Pursuit (OMP). On the contrary, in terms of the execution time, it turned out that the method has no advantage compared to its counterparts, (for the detailed results, see [Achim 2010]). In chapter 3, $\mathcal{S}\alpha\mathcal{S}$-IRLS is hired as a comparative method for the assessment of our proposed approach.

2.1.4.2 Orthogonal Matching Pursuit (OMP)

Orthogonal Matching Pursuit (OMP) [Tropp 2007] is an appealing method to tackle the huge computational burden occurring in CS recovery of high-dimensional sparse signals, the fundamental operation of which is inspired by greedy algorithms [Leiserson 2001]. At each iteration, OMP collects the most correlated atom with the current residual vector ($\mathbf{x}^t = \mathbf{y} - \mathbf{\Theta}\hat{\mathbf{s}}^t$) over all column vectors ($\boldsymbol{\theta}_i$ with $i \in \{1, \dots, N\}$) of the sensing matrix. The stepwise subset consisting of the selected column vectors is updated every iteration and utilized to estimate the non-zero components of the sparse vector by computing least square error, which is iterated until the predefined stop criterion is reached. The stopping rule plays a pivot role to avoid the selection of zero components. [Cai 2011] offers a fruitful discussion with respect to setting of the reasonable stopping rule. OMP is obviously easy to implement and shows fast convergence with computational simplicity. Aside from OMP, there are diverse iterative greedy methods: Stagewise OMP (StOMP) [Donoho 2012], Compressive sampling MP (CoSaMP) [Needell 2009a] and regularized OMP methods [Needell 2009b, Needell 2010]. However if the signal to be recovered is not strictly sparse, the methods would be ineffective. In other words, they commonly show considerably worse sparsity-undersampling tradeoff than convex optimization approaches, which will be illustrated in the Fig. 2.3.

2.1.5 Approximate Message Passing (AMP)

In this thesis, we adopted an approximate message passing (AMP)-based algorithm [Donoho 2009, Donoho 2010] to reconstruct QAM images from spatially undersampled measurements. AMP is a simplified version of MP (message passing) derived from belief propagation [Baron 2009, Yedidia 2005, Kabashima 2003] in graphical models, and is characterized not only by dramatically reduced convergence times but also by a reconstruction performance equivalent to ℓ_p-based methods. AMP uses an iterative process of a sparse representation-based image denoising algorithm performed at each iteration. Hence, the selection of a robust denoiser and of the most efficient sparsifying basis are crucial issues to be addressed in order to achieve fast convergence and high recovery quality [Tan 2015].

In what follows, we explore the mathematical structure of AMP through the derivation from belief propagation, and then explain the role of denoiser in AMP algorithm.

2.1.5.1 Derivation of AMP from belief propagation

Here, in order to illustrate the power of AMP in producing fast and exact recovery, we look into the process to derive AMP from sum-product belief propagation algorithm.

Construction of the graphical model

Utilizing the sparse characteristic of a vector $\mathbf{s}$ and the fact that $\mathbf{y}$ is its observation through a system A, the joint PDF is constructed over all variables $s_i, i \in \{1, 2, \ldots, N\}$ making up the sparse signal as follows:

$$p(s) = \frac{1}{C} \prod_{i=1}^{N} \exp(-\beta |s_i|) \prod_{a=1}^{M} \delta_{y_a=(As)_a} \tag{2.17}$$

where C denotes a normalizing constant to make $\int_{-\infty}^{\infty} p(s)ds = 1$ and $\delta(\cdot)$ represents a Dirac delta function. The subscripts are indices following $\{a, b \ldots\} \in \{1, \ldots, M\}$, $\{i, j \ldots\} \in \{1, \ldots, N\}$, and the (a, i) element of the matrix A is denoted by A_{ai}. Finally β is a parameter to determine the dispersion of the distribution.

In addition, in order to comprehend the architecture of the message passing model, it might be helpful to familiarize with the notations used in belief propagation. $G := (V, F, E)$ represents a complete bipartite factor graph illustrated in Fig. 2.2 consisting of variable nodes $V := [N]$, factor nodes $F := [M]$ and edges connecting the two nodes $E := [N] \times [M] = \{(i, a) : i \in [N], a \in [M]\}$.

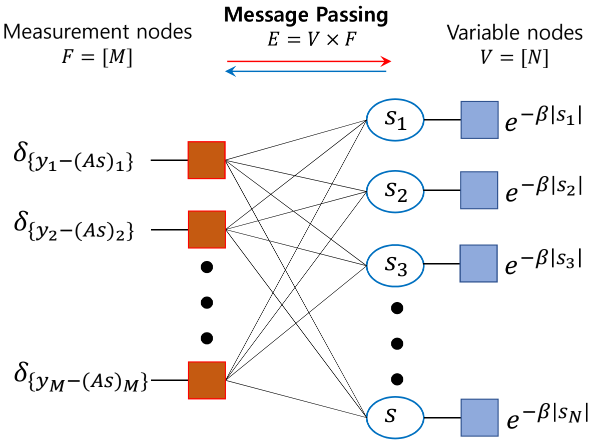

Figure 2.2: The factor graph showing message passing between factor and variable nodes

The update rule of belief propagation messages is given by computing the marginals at each node, namely $\{\nu_{i\to a}\}_{i\in V,a\in F}$ and $\{\hat{\nu}_{a\to i}\}_{a\in F,i\in V}$:

$$\begin{aligned}\nu_{i\to a}^{t+1}(s_i) &\cong \exp(-\beta|s_i|)\prod_{b\neq a}\hat{\nu}_{b\to i}^{t}(s_i)\\ \hat{\nu}_{a\to i}^{t}(s_i) &\cong \int\prod_{j\neq i}\nu_{j\to a}^{t}(s_i)\delta_{\{y_a-(As)_a\}}ds_i\end{aligned}\tag{2.18}$$

Simplification of messages in large system limit

With respect to large N, the central limit theorem allows the messages in (2.18) to be converted into mean and variance. The detailed derivation procedures can be found in [Donoho 2011], and consequently the classical message passing (MP) algorithm is as follows:

$$x_{i\to a}^{t+1} = \eta_t\left(\sum_{b\in[n]\setminus a} A_{bi}z_{b\to i}^{t}\right)\tag{2.19}$$

$$z_{a\to i}^{t} = y_a - \sum_{j\in[N]\setminus i} A_{aj}x_{j\to a}^{t}\tag{2.20}$$

where η function plays the role of soft thresholding, given the setting of $\beta\to\infty$; as $\beta\to\infty$, the density of (2.17) concentrates on the basis pursuit solution [Donoho 2011]. These are evidently simplified version of (2.18), and this recursive concept [Richardson 2008, Pearl 2014] has inspired the design of many MP-based algorithms. However, the computational cost is still expensive since this update rule forces to track the MN messages every iteration.

From MP to AMP

In order to reduce the algorithm complexity of the MP methods, conventional fast iterative thresholding approaches [Herrity 2006, Indyk 2008, Maleki 2009] exploit the fact that, in large system, the right terms of (2.19) and (2.20) weakly depend on the index a and i respectively. In other words, the difference made by a single index can be neglected on the summation of (2.19) and (2.20), which leads to the assumption that messages sent from a variable node are all equal regardless of factor nodes, *i.e.*, $x_{i\to a}^{t}\approx x_i^t$ and the reverse is also valid, *i.e.*, $z_{a\to i}^{t}\approx z_a^t$. As a result, the approaches cited above are established with the following basic structures:

$$\begin{aligned}\mathbf{x}^{t+1} &= \eta\left(\mathbf{A}^{\mathbf{T}}\mathbf{z}^{t}+\mathbf{x}^{t}\right)\\ \mathbf{z}^{t} &= \mathbf{y}-\mathbf{A}\mathbf{x}^{t}\end{aligned}\tag{2.21}$$

Owing to the large system assumption, the MN messages demanded in MP algorithms can be remarkably decreased to $M+N$ every iteration.

Meanwhile, AMP algorithm pursues more careful analysis than the derivation process performed to obtain (2.21). Specifically, AMP introduces the first order Taylor approximation of (2.19) considering the correction of the error caused by the assumptions of $x_{i\to a}^t \approx x_i^t$ and $z_{a\to i}^t \approx z_a^t$, the result of which produces the additional term as follows [Donoho 2011]:

$$\begin{aligned} \mathbf{x}^{t+1} &= \eta\left(\mathbf{A}^{\mathbf{T}}\mathbf{z}^t + \mathbf{x}^t\right) \\ \mathbf{z}^t &= \mathbf{y} - \mathbf{A}\mathbf{x}^t + \underbrace{\frac{1}{\delta}\mathbf{z}^{t-1}\left\langle \eta'\left(\mathbf{A}^{\mathbf{T}}\mathbf{z}^{t-1} + \mathbf{x}^{t-1}\right)\right\rangle}_{\textit{Onsager reaction term}} \end{aligned} \tag{2.22}$$

which is called the Onsager reaction term in statistics physics [Thouless 1977]. The authors in [Donoho 2011] proved, through the analysis of dynamical behavior with state evolution (SE) formalism, that the error correction term is a decisive factor allowing AMP to overwhelmingly outperform other fast iterative algorithms in the sparsity-undersampling tradeoff, and even be comparable to the performance of LP-based reconstructions. That is demonstrated in Fig. 2.3 which shows the comparison of the phase transition graphs among three different recovery methods, where the upper area of the graph represents the successful recovery of the algorithm.

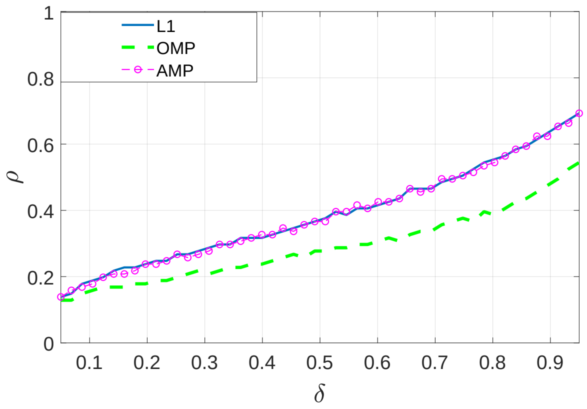

Figure 2.3: The phase transitions of reconstruction algorithms are compared. δ and ρ denote the undersampling rate (M/N) and sparsity (K/N) respectively. AMP demonstrates the equivalent recovery performance to L1 reconstruction. AMP used in this simulation adopted the soft thresholding as the η function.

2.1.5.2 Remark on η function

We end the preliminary study of CS briefly inspecting the nature of η function turning out to perform soft thresholding as stated previously, whereby we realize that the role of the function is equivalent to the manner that a normal denoiser works in the modern signal processing.

Suppose that we are interested in solving the inverse problem of $\mathbf{y} = \mathbf{A}\mathbf{x}$. When introducing an operator $\mathbf{H} = \mathbf{A}^{\mathbf{T}}\mathbf{A} - \mathbf{I}$, $\mathbf{A}^{\mathbf{T}}\mathbf{y} = \mathbf{x}_0 + \mathbf{H}\mathbf{x}_0$ makes sense with respect to the estimate $\mathbf{x}_0$ of $\mathbf{x}$. If $\mathbf{A}$ is orthogonal, $\mathbf{H} = 0$ and the solution is immediately found from $\mathbf{A}^{\mathbf{T}}\mathbf{y}$. However in the undersampling setting, *i.e.*, when $\mathbf{A}$ is an $M \times N(M < N)$ random matrix, the inverse of $\mathbf{A}$ does not exist. Therefore, rather than $\mathbf{H}\mathbf{x}_0 = 0$, $\mathbf{H}\mathbf{x}_0$ acts like a sort of noisy random vector, and $\mathbf{A}^{\mathbf{T}}\mathbf{y}$ can be recast as $\mathbf{x}_0 + \boldsymbol{\epsilon}$ denoting the noise by $\boldsymbol{\epsilon}$. In order to denoise $\mathbf{A}^T\mathbf{y}$ with typical iterative methods, when beginning from an initial setup that elements of $\mathbf{x}^0$ are all zero, the second iteration leads to $\mathbf{A}^T(\mathbf{y} - \mathbf{A}\mathbf{x}^1) = \mathbf{x}_0 - \mathbf{x}^1 + \mathbf{H}(\mathbf{x}_0 - \mathbf{x}^1)$. Consequently, one may anticipate to keep on reducing the noise level by iterating the operation; the initial noise level with the variance of $M^{-1}\|\mathbf{x}_0\|_2^2$ will be reduced, at the next step, to the variance of $M^{-1}\|\mathbf{x}_0 - \mathbf{x}^1\|_2^2$.

In this regard, all iterative thresholding approaches including AMP are dedicated to the design of denoising technique to fast and effectively remove $\boldsymbol{\epsilon}$ for the exact sparse recovery. Provided that the noise vector is accurately modeled as i.i.d. normal distribution, [Donoho 1994] demonstrated that the soft thresholding having the appropriate threshold value can show the best performance in denoising of a sufficiently sparse vector. The standard AMP algorithm proposed by [Donoho 2009] have been devised with the soft thresholding, and we will extend the original model by adopting more robust denoiser and introducing more powerful sparsity expression in Chapter 3.

2.1.6 Applications of CS to US imaging

Fig. 2.4 compares the US images reconstructed by different recovery algorithms with the measurement rate of 60%. In particular, the figure highlights the superiority of $\mathcal{S}\alpha\mathcal{S}$-IRLS [Achim 2010] introduced in section 2.1.4.1, demonstrating that RF echoes can be best recovered with the optimal p determined exploiting the characteristic exponent α of US data. Furthermore, [Achim 2015] shows in Fig. 2.5 that the recovery performance of the approach in [Achim 2010] can be more enhanced, when being implemented in Fourier domain where the distribution of US RF echoes is more heavy-tailed and using prior knowledge from the acquisition process, *i.e.*, the frequency of acquisition and transducer bandpass.

2.2 Finite rate of innovation

This section is devoted to delivering the theoretical background underlying the second contribution of this thesis. Whereas the focus of the preceding section is on finding the breakthrough of the conventional data acquisition of QAM in the spatial domain, henceforth we introduce a leading-edge sampling framework able to drastically reduce the number of samples per QAM RF signal in the temporal domain.

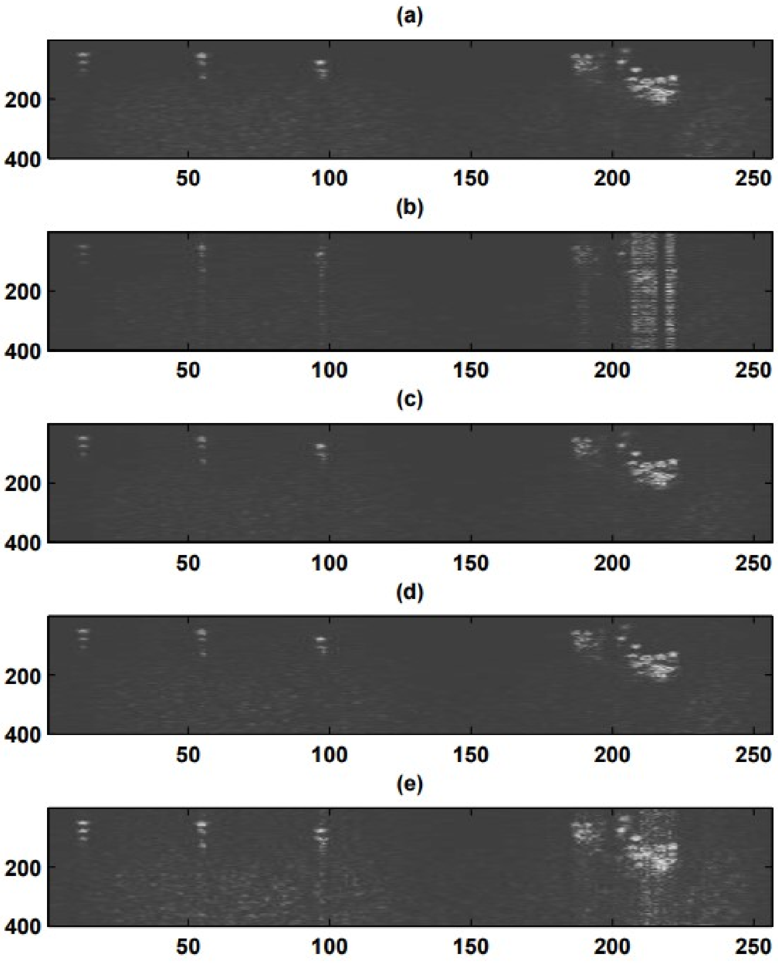

Figure 2.4: Comparison of original and reconstructed patches. (a) Original (RF) ultrasound image. Reconstructions with (b) $\ell_{p_{opt}}$-norm (c) $\ell_{\alpha-0.01}$-norm (d) BP and (e) OMP [Achim 2010].

2.2.1 Overview of FRI

The approach that will be proposed in Chapter 4 is based on the finite rate of innovation (FRI) theory [Vetterli 2002] that provides theoretical guarantees for reconstructing FRI signals, *i.e.* described by a limited number of parameters, from a small number of samples acquired at the innovation rate. Interestingly, it has been shown that relevant recovery schemes are even possible in the case of non-bandlimited signals such as stream of Diracs, nonuniform splines and piecewise polynomials [Vetterli 2002, Urigüen 2013a, Wei 2016]. The key concept making the approach feasible is that the aforementioned class of signals can commonly be modeled as union of subspaces instead of a single linear vector space

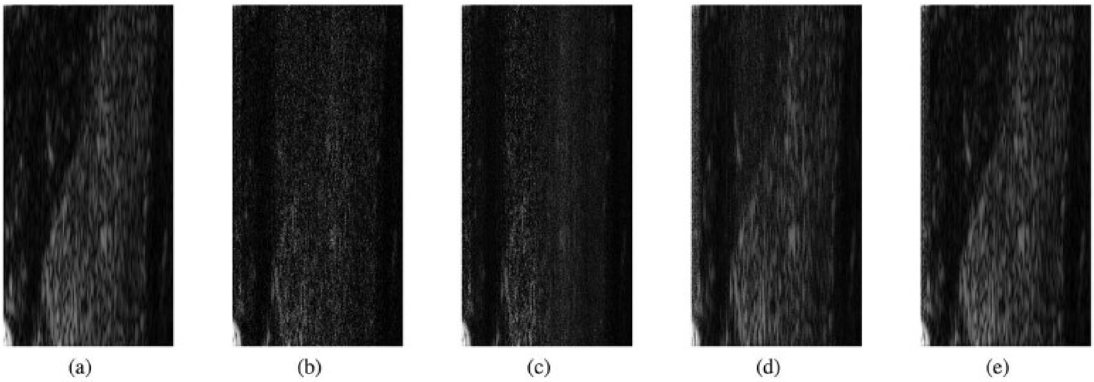

Figure 2.5: Reconstruction results for a thyroid ultrasound image using 33% of the number of samples in the original (a) B-mode ultrasound image (b) Reconstruction with Lasso (c) $\mathcal{S}\alpha\mathcal{S}$-IRLS reconstruction (d) $\mathcal{S}\alpha\mathcal{S}$-IRLS in the Fourier domain (e) Fourier domain IRLS with dual prior [Achim 2015].

forcing an input signal to be bandlimited [Lu 2008]. Specifically, in the context of FRI, the signals can be interpreted as living in a shift-invariant subspace spanned by a set of parameters with a known basis. As such, given the basis function as a prior information, the novel sampling process carries out an uniform sampling at a dramatically reduced sampling rate, *i.e.* the rate of innovation, corresponding to the degree of freedom able to completely characterize the considered signal. The reconstruction strategy consists of identifying the innovation part of the signal that is equivalent to finding the locations and amplitudes of frequencies in a standard problem of spectral analysis [Stoica 2005]. The annihilating filter technique [Stoica 2005, Blu 2008] or the matrix pencil method [Hua 1990, Sarkar 1995, Golub 1999] has been verified as the reliable solvers leading the exact recovery in the FRI setup [Dragotti 2007, Maravic 2005].

2.2.2 Preliminary theory

Here, we clarify the notion of FRI signals by understanding the fundamental difference from the conventional sampling theorem.

2.2.2.1 FRI interpretation of classical sampling theory

We herein figure out the potential of FRI by witnessing the intrinsic limitation of the classical sampling theory.
When storing or processing real-world continuous-time signals with a digital device, the analog to digital conversion (ADC) is involved, the first stage of which is sampling as illustrated in Fig. 2.6. In terms of the classical sampling mechanism, the signal of interest

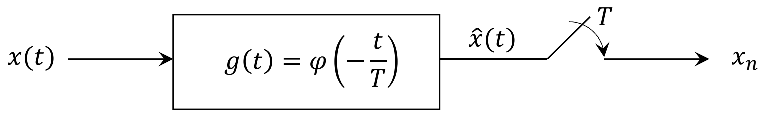

Figure 2.6: The schematic diagram shows the canonical sampling setup where $x(t)$ is a continuous-time signal. It is filtered by $g(t)$ and then uniformly sampled with interval T seconds. The resulting samples are given by $x_n = \langle x(t), \varphi\left(\frac{t}{T} - n\right)\rangle$.

$x(t)$ is filtered by the sampling kernel $\varphi(t)$ which is the scaled and time reversed version of $g(t)$, and then uniformly sampled every T seconds. The sampled discrete sequence x_n are given by:

$$\begin{aligned} x_n = (x * g)(t)|_{t=nT} &= \left\langle x(t), \varphi(\frac{t}{T} - n)\right\rangle \\ &= \int_{-\infty}^{\infty} x(t)\varphi(\frac{t}{T} - n)dt \end{aligned} \tag{2.23}$$

Here, the key concern of this process is whether x_n can preserve sufficient information allowing the unique recovery of the original signal $x(t)$. In order to provide more rigorous answer, we need to comprehend the physics of the sampling process. x_n is acquired by orthogonal projection of $x(t)$ onto the shift-invariant subspace V spanned by sampling kernel $\varphi(t)$ having the bandwidth of $[-\frac{B}{2}, \frac{B}{2}]$. In addition, the sampling period T is determined by the reciprocal of twice the maximum frequency of the kernel $\varphi(t)$, *i.e.*, $\frac{1}{B}$. Therefore, if $x(t)$ does not contain any frequency component exceeding the maximum frequency $\frac{B}{2}$, namely $x(t) \in V$, the perfect recovery is guaranteed as follows:

$$x(t) = \sum_{n=-\infty}^{\infty} x(nT)\tilde{\varphi}\left(\frac{t}{T} - n\right) \tag{2.24}$$

where $\tilde{\varphi}(t)$ is chosen from any function satisfying the pair of $\langle\varphi(t-n), \tilde{\varphi}(t-k)\rangle = \delta_{n-k}$. Unless this is the case, the recovery process produces merely an approximate reconstruction $\hat{x}(t)(\neq x(t))$ which is the projection onto the subspace of the bandlimited signals, *i.e.*, span$\{\tilde{\varphi}\left(\frac{t}{T} - n\right)\}_{n \in Z}$. Note that real-life signals are never exactly bandlimited, and thus the conventional sampling scheme inevitably gives rise to a loss of information in input signals. Instead, the subspace interpretation paves the way for the introduction of a novel sampling scheme (FRI) allowing a lossless recovery irrespective of the constraint of bandlimit; if and only if they are classes of signals belonging to the union of subspace spanned with an arbitrary function, as well as the measurement is equivalent to the degree of freedom of the signal called the innovation rate denoted by ρ.

From the perspective of FRI, the twice maximum frequency (B) of a bandlimited signal within $\left[-\frac{B}{2}, \frac{B}{2}\right]$ is interpreted as the innovation rate of the signal, *i.e.*, $B = \rho$. There-

fore, the argument of the classical sampling theory for achieving a faithful recovery is equivalent to indicating the classes of signals with finite number of parameters per unit of time in the viewpoint of FRI.
In the following, we present the explicit definition of the innovation rate and the typical expressions defining the parametric form of FRI signals.

2.2.2.2 Parametric modeling of FRI signals

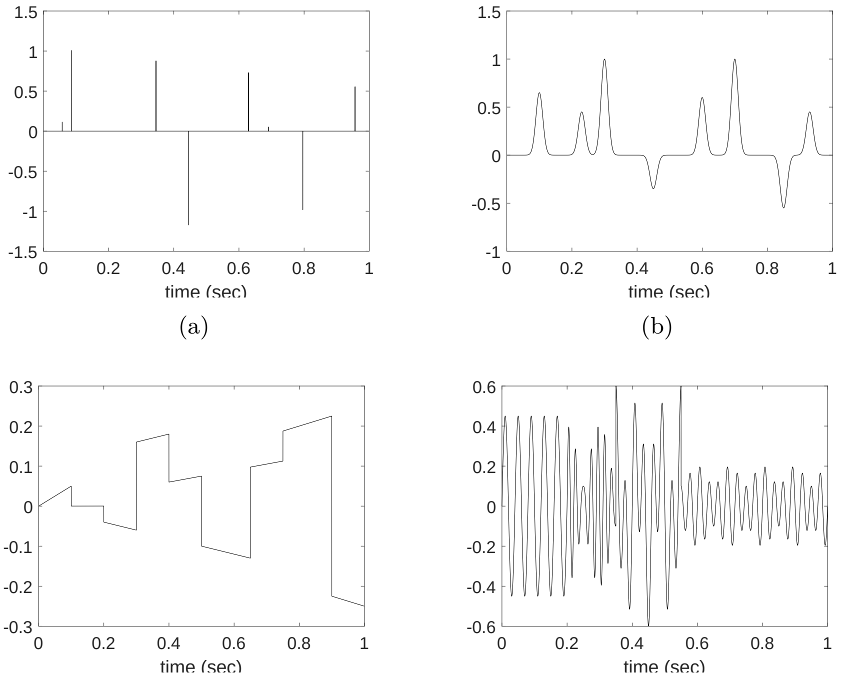

(a) (b)

(c) (d)

Figure 2.7: The figures display prototypical FRI signals: (a) train of Diracs, (b) stream of pulses, (c) piecewise polynomial and (d) piecewise sinusoidal.

Starting from the seminal paper of Vetterli *et al.* [Vetterli 2002], a rich literature exists on the reconstruction of this type of signals from a limited number of samples. The number of measurements required for FRI signals is dictated by the rate of innovation as mentioned before, *i.e.*, the number of parameters defining $x(t)$ over one period. The innovation rate ρ of a signal $x(t)$ is defined as follow:

$$\rho = \lim_{\tau \to \infty} \frac{1}{\tau} C_x \left(-\frac{\tau}{2}, \frac{\tau}{2} \right), \tag{2.25}$$

where $C_x[t_a, t_b]$ represents a counting function that counts the number of parameters of

$x(t)$ over the interval of time $[t_a, t_b]$. Signals with a limited number of degrees of freedom occur in various applications such as astronomy [Pan 2017], radar [Rudresh 2017], medical imaging [Oñativia 2013] or wideband communications [Maravic 2003, Maravic 2004]. Fig 2.7 depicts examples of the signals with FRI, and particularly Fig 2.7 (a-b) can be characterized with the following τ-periodic parametric form:

$$x(t) = \sum_{m \in Z} \sum_{l=0}^{L-1} a_l h(t - t_l - m\tau) \tag{2.26}$$

where $h(t)$ is a possibly non-bandlimited pulse considered known, *e.g.* Dirac delta function, and located at times $\{t_l\}_{l \in L}$ and scaled by the amplitudes $\{a_l\}_{l \in L}$. Thus, these signals have $2L$ degrees of freedom.

The signal shown in Fig 2.7 (c) is piecewise polynomial and expressed as the following form [Dragotti 2007]:

$$x(t) = \sum_{l=0}^{L-1} \sum_{r=0}^{R-1} a_{l,r} \left(t - t_l\right)_+^r \tag{2.27}$$

where $x(t)$ consists of L pieces of maximum degree $R-1$ $(R > 0)$, and $t_+^r = \max(t, 0)^r$. Furthermore, Rth derivative of $x(t)$ is given by a stream of differentiated Diracs, $x^{(R)}(t) = \sum_{l=0}^{L-1} \sum_{r=0}^{R-1} r! a_{l,r} \delta^{(R-r-1)}(t - t_l)$. In this case, the rate of innovation is $L + RL = L(1+R)$, and the samples of $x(t)$ obtained by a polynomial reproducing sampling kernel are related to those of $x^{(R)}(t)$ to reconstruct $x(t)$ [Dragotti 2007].

[Berent 2009] extended FRI theory to piecewise sinusoidal functions which are concatenated by multiple pieces of oscillating functions containing time and frequency components as shown in Fig. 2.7 (d), and also has the parametric expression as:

$$x(t) = \sum_{l=0}^{L-1} \sum_{d=0}^{D-1} a_{l,d} \cos\left(\omega_{l,d} t - \theta_{l,d}\right) \xi_d(t) \tag{2.28}$$

where $a_{l,d}$, $\omega_{l,d}$, and $\theta_{l,d}$ are unknown parameters, and denote respectively amplitudes, frequencies and phases. On the other hand, $\xi_d = u(t - t_d) - u(t - t_{d+1})$ defines the duration of summation of individual sinusoids, $u(t)$ is the Heaviside step function, and t_d is the instant of time to be determined.

Also, it should be noted that the QAM RF signal of our interest in Fig 1.11 (b) is amenable to FRI framework since the physical phenomenon dominating the formation of the signal can be explained in the view of the FRI parametric modeling. The in-depth discussion of the above implication is presented in Chapter 4.

We have defined FRI signals and observed various examples, for which the sampling and reconstruction processes are resumed hereafter.

2.2.3 Sampling kernels and FRI sampling

In the previous subsection, it was shown that FRI acquisition process is akin to the classical sampling process for a bandlimited signal due to the fact that, in this case, the rate of innovation is consistent with the Nyquist rate. Thus, the ideal low-pass filter can be considered as one of FRI sampling kernels. In fact, the authors of [Blu 2008] showed that the FRI signal with τ-periodic K Diracs is sampled with a sinc function of the bandwidth $B\tau$[Hz], and the $2M+1$ samples corresponding to $B\tau$ are enough for perfectly estimating $2K$ parameters of the input signal using annihilating filter. However, the sampling method has an infinite support, and consequently is impractical in real systems. In this regard, finding the appropriate sampling kernel is the central objective of several existing studies [Vetterli 2002, Maravic 2005].
In what follows, we explore FRI sampling kernels compactly supported in time, and their properties letting a sequence of numbers x_n to be the exact representation of an original signal $x(t)$.

2.2.3.1 Polynomial reproducing kernel and Strang-Fix condition

A polynomial reproducing kernel of order $(P+1)$ is any function $\varphi(t)$ that can reproduce polynomials of maximum degree P via a linear combination of its shifted versions. That can be expressed with proper coefficients $c_{m,n}$ as follows:

$$\sum_{n\in\mathbb{Z}} c_{m,n}\varphi(t-n) = t^m, \quad m = 0,\dots,P \tag{2.29}$$

The family of polynomial reproducing kernels obeys the so-called Strang-Fix conditions [Strang 2011], namely (2.29) for $\varphi(t)$ holds if and only if

$$\Phi(0) \neq 0 \quad \text{and} \quad \Phi^{(m)}(2j\pi l) = 0, \quad \text{for} \quad m = 0,\dots,P \quad l \in \mathbb{Z}\setminus\{0\} \tag{2.30}$$

where $\Phi(\omega)$ denotes Fourier transform of $\varphi(t)$, and $\Phi^{(m)}(\omega)$ represents its mth derivative. B-spline [Schoenberg 1946] is one example of functions meeting Strang-Fix condition, and $(P+1)$ order $\beta_P(t)$ is obtained by the convolution of $(P+1)$ box functions $\beta_0(t)$ having 1 for $t \in (0,1]$ and zero otherwise, and its Fourier transform $B_0(j\omega) = \frac{1-e^{-j\omega}}{j\omega}$ [Unser 1999]:

$$\beta_P(t) = \underbrace{(\beta_0 * \beta_0, \cdots * \beta_0)}_{P+1\,\text{order}}(t) \tag{2.31}$$

A function $\varphi(t)$ of order $(P+1)$ satisfying (2.29) can be created by a linear combination of shifted versions of B-spline in (2.31), and therefore such a polynomial reproducing kernel has a $(P+1)$ compact support in time. Next we discover another kernel having a finite duration, which is reckoned as a generalized form with respect to $\varphi(t)$ in (2.29).

2.2.3.2 Exponential reproducing kernel

Exponential reproducing kernels [Dragotti 2005] have been most commonly used for sampling FRI signals owing to various advantages. First and foremost, it is of compact support, and thus physically applicable for many existing sampling applications, furthermore the property of which plays a key role to derive a novel FRI sampling strategy permitting to use arbitrary kernels [Urigüen 2013b]. Finally, it is also worth mentioning that the characteristic of the kernel allows the stable and robust design of a sampling device with respect to a noise scenario [Urigüen 2013a]. That can be any function satisfying the following:

$$\sum_{n\in\mathbb{Z}} c_{m,n}\varphi(t-n) = e^{\alpha_m t}, \quad m = 0, \dots, P \tag{2.32}$$

where $c_{m,n}$ are proper coefficients able to reproduce complex exponentials, *i.e.*, $e^{\alpha_m t}$ with complex value parameters α_m, via linear combination of shifted versions of any function $\varphi(t)$. (2.32) hold for the family of the exponential reproducing kernels if and only if $\varphi(t)$ obeys the so-called generalized Strang-Fix conditions [Khalidov 2005, Vonesch 2007, Urigüen 2013b]:

$$\Phi(\alpha_m) \neq 0 \quad \text{and} \quad \Phi(\alpha_m + 2j\pi l) = 0, \quad \text{for} \quad m = 0, \dots, P \quad l \in \mathbb{Z}\setminus\{0\} \tag{2.33}$$

where $\mathit{\Phi}(\alpha_m)$ represents the Laplace transform of $\varphi(t)$ evaluated at α_m.
Note that if the specific kernel $\varphi(t)$ meeting the above conditions is known, the coefficients $c_{m,n}$ can be numerically computed as follows:

$$\begin{aligned} c_{m,n} &= \int_{-\infty}^{\infty} e^{\alpha_m t}\tilde{\varphi}(t-n)dt \\ &= \int_{-\infty}^{\infty} e^{\alpha_m x}e^{\alpha_m n}\tilde{\varphi}(x)dx \\ &= e^{\alpha_m n}\underbrace{\int_{-\infty}^{\infty} e^{\alpha_m x}\tilde{\varphi}(x)dx}_{c_{m,0}} = e^{\alpha_m n}c_{m,0} \end{aligned} \tag{2.34}$$

where the dual analysis function $\tilde{\varphi}(t)$ is biorthogonal to $\varphi(t)$, *i.e.*, $\langle\tilde{\varphi}(t-n), \varphi(t-m)\rangle = \delta_{m-n}$[Unser 2005].
The authors in [Urigüen 2013a] established the condition of the coefficients $c_{m,n}$ for the kernel $\varphi(t)$ to guarantee the stable and accurate recovery that the absolute values of $c_{m,0}$ are equal to entrywise, *e.g.*, $|c_{m,0}| = 1$, and α_m should be purely imaginary exponents able to span an entire unit circle. In addition, complex conjugate exponential pairs in α_m lead to practical real valued analog filters.
In order to obtain $\varphi(t)$ satisfying (2.32), it is necessary to figure out the notion of exponential splines, *i.e.*, E-spline, the first order of which by definition is β_α having $e^{\alpha t}$ for $t \in (0, 1]$ and zero otherwise, and its Fourier transform is given by $B_\alpha(j\omega) = \frac{1-e^{\alpha-j\omega}}{j\omega-\alpha}$.

Higher order of E-splines can be obtained by the successive convolution of lower ones with specific parameters $\vec{\alpha} = (\alpha_0, \alpha_1, \ldots, \alpha_P)$ as follows [Unser 2005]:

$$\beta_{\vec{\alpha}}(t) = (\beta_{\alpha_0} * \beta_{\alpha_1}, \cdots * \beta_{\alpha_P})(t) \tag{2.35}$$

where we notice that in the case of $\alpha = 0$, (2.35) is identical to (2.31), and therefore the family of E-splines is a generalized form of that of B-spline. Also note that since the exponential reproduction property is kept through convolution as proven in [Unser 2005], any composite function $\psi(t)$ produced by $(h * \varphi)(t)$ relative to an arbitrary function $h(t)$ is still able to reproduce exponentials, and consequently $\sum_{n\in\mathbb{Z}} \hat{c}_{m,n}\psi(t-n) = e^{\hat{\alpha}_m t}$ [Urigüen 2011].
In the following, we will show how to sample FRI signals with the exponential reproducing kernel, and examine how the resulting samples are related to the unknown parameters.

2.2.3.3 Exponential moments

Let x_n be a finite set of N uniform samples acquired by low-pass filtering an FRI signal $x(t)$ with the exponential reproducing kernel $\varphi(t)$ in (2.32), and uniformly sampling at intervals of T seconds:

$$x_n = \left\langle x(t), \varphi\left(\frac{t}{T} - n\right)\right\rangle \tag{2.36}$$

For estimating the unknown parameters of the signal $x(t)$, the discrete numbers x_n are converted into a sequence of moments S_m as follows:

$$\begin{aligned} S_m &= \sum_{n=0}^{N-1} c_{m,n} x_n \\ &= \left\langle x(t), \sum_{n=0}^{N-1} c_{m,n}\varphi\left(\frac{t}{T} - n\right)\right\rangle \\ &= \int_{-\infty}^{\infty} x(t) e^{\frac{\alpha_m t}{T}} dt \end{aligned} \tag{2.37}$$

where it is obvious that S_m is equivalent to the projection of $x(t)$ onto the subspace spanned by $\{e^{\alpha_m}\}_{m=0}^{P}$, and thus it is exactly the bilateral Laplace transform of $x(t)$ evaluated at $\{\alpha_m\}_{m=0}^{P}$, or is the Fourier transform $X(\omega_m)$ of $x(t)$ at $\omega = \{\omega_m\}_{m=0}^{P}$ when α_m is purely imaginary, $\alpha_m = -j\omega_m$.
In order to make the implication of (2.37) clearer in the perspective of the parameter estimation, we apply the specific FRI signal of (2.26) to $x(t)$ in the last equality of (2.37), which is characterized as the weighted and delayed periodic signal of a known pulse $h(t)$ with τ-period. For the simplicity, the period τ is considered as one second, and we confine the exponential moments S_m to Fourier domain respecting the constraints for

coefficients $c_{m,n}$ in [Urigüen 2013a].

$$\begin{aligned} S_m &= \int_{-\infty}^{\infty} \underbrace{\sum_{l=0}^{L-1} a_l h(t-t_l)}_{\text{one period of } x(t)} e^{\frac{-j\omega_m t}{T}} dt \\ &= \int_{-\infty}^{\infty} \sum_{l=0}^{L-1} a_l h(u) e^{\frac{-j\omega t_l}{T}} e^{\frac{-j\omega_m u}{T}} du = \sum_{l=0}^{L-1} a_l e^{\frac{-j\omega_m t_l}{T}} \int_{-\infty}^{\infty} h(t) e^{\frac{-j\omega_m t}{T}} dt \\ &= H(\omega_m) \sum_{l=0}^{L-1} a_l u_l^m \end{aligned} \tag{2.38}$$

where u_l^m stands for $e^{\frac{-j\omega_m t_l}{T}}$. By normalizing the left-hand side with the prior knowledge $H(\omega_m)$, we obtain the power sum series form:

$$\mathcal{N}_m = \frac{S_m}{H(\omega_m)} = \sum_{l=0}^{L-1} a_l u_l^m \tag{2.39}$$

where determining innovation parameters $\{a_l, t_l\}_{l=0}^{L-1}$ from $\{\mathcal{N}_m\}_{m=0}^{P}$ can be solved by conventional tools from spectral estimation [Stoica 2005] such as annihilating filter method (Prony's method) [Vetterli 2002, Dragotti 2007].
In the sequel, we review some of the existing recovery strategies.

2.2.4 Parameter estimation

A power series form such as (2.39) commonly appears at signal decomposing problems with linear combination of complex exponentials. The Annihilating filter proposed by Gaspard de Prony is known as the first solution to the parametric spectral estimation, and has been extensively employed as a tool to not only determine unknown parameters in FRI area but also decode the CS information [Hormati 2007]. Hereinafter, we review the annihilating filter structure and its properties, and additionally address recovery methods in noisy setting.

2.2.4.1 Annihilating filter

Based on the definition of the annihilating filter $\{\mathcal{A}_m\}_{m=0}^{L}$ to null out $\mathcal{N}_m$ and its Z-transform $\hat{\mathcal{A}}(z)$ given in (2.40) and (2.41), the estimation of the u_l's is equivalent to finding the zeros of Z-transform $\hat{\mathcal{A}}(z)$ such that the location t_l's are distinct.

$$\hat{\mathcal{A}}(z) = \sum_{m=0}^{L} \mathcal{A}_m z^{-m} = \prod_{l=0}^{L-1} (1 - u_l z^{-1}) \tag{2.40}$$

$$\begin{aligned}\mathcal{A}_m * \mathcal{N}_m &= \sum_{i=0}^{L} \mathcal{A}_i N_{m-i} = \sum_{i=0}^{L-1} \mathcal{A}_i \sum_{l=0}^{L-1} a_l u_l^{m-i} \\ &= \sum_{l=0}^{L-1} a_l u_l^{m} \underbrace{\sum_{i=0}^{L} \mathcal{A}_i u_l^{-i}}_{\hat{\mathcal{A}}(u_l)=0} = 0\end{aligned} \tag{2.41}$$

Consequently the time instance u_l's are determined by the roots of the filter coefficients following the next steps.
(2.41) can be recast as a matrix-vector form $\mathbf{Na} = 0$ as follows:

$$\underbrace{\begin{pmatrix} \mathcal{N}_L & \mathcal{N}_{L-1} & \dots & \mathcal{N}_0 \\ \mathcal{N}_{L+1} & \mathcal{N}_L & \dots & \mathcal{N}_1 \\ \vdots & \vdots & \ddots & \vdots \\ \mathcal{N}_P & \mathcal{N}_{P-1} & \dots & \mathcal{N}_{P-L} \end{pmatrix}}_{\mathbf{N}} \underbrace{\begin{pmatrix} \mathcal{A}_0 \\ \mathcal{A}_1 \\ \vdots \\ \mathcal{A}_L \end{pmatrix}}_{\mathbf{a}} = \begin{pmatrix} 0 \\ 0 \\ \vdots \\ 0 \end{pmatrix}, \tag{2.42}$$

where $\mathbf{N}$ is a Toeplitz matrix of $\mathcal{N}_m$ of size $(P - L + 1) \times (L + 1)$ provided that the sampling kernel's order $(m = 0, \dots, P)$ satisfies $P + 1 \geq 2L$, and vector $\mathbf{a}$ denotes the annihilating filter coefficients. Following the convention of $\mathcal{A}_0 = 1$, (2.42) is restructured as the system having L equations. Thus, for identifying $\{\mathcal{A}_1, \dots, \mathcal{A}_L\}$, at least $2L$ consecutive values of $\mathcal{N}_m$ are required. The time delays t_l are found by the roots of the vector $\mathbf{a}$, and the amplitudes a_l are retrieved by a linear problem solving L consecutive equations in (2.39).
Fig. 2.8 depicts that the two synthetic signals are exactly reconstructed by the annihilating filter method and the LSE solver.

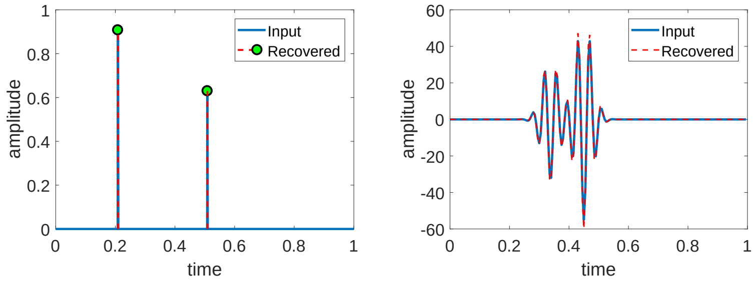

(a) (b)

Figure 2.8: Reconstruction results of a Stream of Diracs (a) and modulated Gaussian pulses, $e^{-\frac{(t-t_0)^2}{\sigma^2}}\cos(2\pi t f_c)$ (b).

2.2.4.2 Retrieval of FRI signals in a noisy setting

To deal with complex exponentials perturbed by noise, diverse advanced approaches derived from Prony's method have been developed [Maravic 2005, Urigüen 2013a, Wei 2016]. The total least squares (TLS) [Moor 1993] is one of these methods.
TLS attempts to find an optimal solution by minimizing $\| \mathbf{Na} \|^2$. In a nutshell, the singular value decomposition (SVD) with respect to the matrix $\mathbf{N}$ is performed, and in turn $\mathbf{N} = \mathbf{U}\Delta\mathbf{V}^H$ is acquired. The vector $\mathbf{a}$ is obtained by choosing the last column vector of the right unitary matrix $\mathbf{V}$ corresponding to the smallest singular value. Time delays t_l are determined from the roots u_l of coefficients of the filter $\mathbf{a}$. Finally, the amplitudes a_l can be obtained from the least square estimator (LSE) associated to (2.39), by solving $\mathcal{N}_m - \sum_{l=0}^{L-1} a_l u_l^m \approx 0$.
Furthermore, recent related studies [Blu 2008, Urigüen 2013a, Wei 2016] introduced TLS-Cadzow routine [Cadzow 1988] to achieve more robust reconstruction, which implements an iterative denoising for noisy measurements prior to a parameter estimation explained above. The approach is motivated by the fact that the matrix $\mathbf{N}$ formed by noisy moments is no longer rank-deficient rather close to a full rank. The main principle of the approach consists of two operations every iteration; the rank reduction by replacing all singular values with zero but L largest values, and then forcibly imposing a Toeplitz matrix structure on the matrix of the current stage by averaging diagonal elements.

2.3 Summary

In this chapter, we have presented an overview and general theory on the state-of-the-art data acquisition frameworks which must be the backbone of the contributions of this thesis. However, in order to cope with our problems related to the QAM system, we should further evolve the current technologies since, to the best of our knowledge, the data structure and system mechanism of QAM have never been considered in the realms of CS or FRI to date. In short, the raster scanning manner of QAM is not compatible to any sensing scheme devised in CS literature at all. In addition, the frequency attenuation effect occurring in QAM RF signals is a pretty intractable parameter in FRI context.
In this sense, the main original contributions of the thesis is disclosed in the following chapters.

Chapter 3

Approximate message passing algorithm for reconstruction of QAM 2D maps

Part of the work in this chapter has been published in [Hill 2016], [Kim 2016], [Kim 2017], and [Kim 2018a].

Contents

3.1 Introduction

A current QAM technique pursuing a fine resolution microscopic image necessarily exploits high frequency, *i.e.*, 250 MHz or 500 MHz, and performs a quite dense scanning which is time consuming and generates considerable amount of data.

This chapter proposes the novel approach to enhance the efficiency of the data acquisition process with respect to QAM by introducing Compressive Sampling (CS) framework in spatial domain. CS has been vigorously studied as an alternative of Nyquist sampling theorem for the last decade which, given particular conditions, proved to guarantee the perfect reconstruction of the undersampled data even below Nyquist rate. Recall that the CS measurement is modeled as:

$$\mathbf{y} = \mathbf{\Phi}\mathbf{x} + \mathbf{n} \tag{3.1}$$

The strategy to estimate the original image $\mathbf{x}$ from the observation $\mathbf{y}$ can be made up of the two separate procedures known as sensing and recovery which, in a classical manner, are commensurate with the construction of measurement matrix and the design of the recovery algorithm respectively. When it comes to the former, in the case of QAM the data acquisition fashion is not able to follow the conventional sensing matrix based on randomness because of the mechanical motion of QAM motor stage consecutively taking data by continuous raster scanning. On the other hand, as a method of the latter to find a sparse solution, this work employs Cauchy-AMP algorithm performing denoising in a wavelet domain, based on the hypothesis that wavelet coefficients of QAM images show heavy tailed PDF (probability density function) fit for Cauchy distribution.

Our proposed AMP-based QAM imaging framework consists of two major modules.: (i) In the data acquisition component of our system, we propose novel techniques for QAM data sampling, by choosing sensing matrices that meet CS requirements, and simultaneously take into account the mechanism of practical QAM acquisition devices based on raster scanning. (ii) In the image reconstruction component, we design and test a wavelet domain AMP-based approach, which exploits underlying data statistics through the use of a Cauchy-based maximum a posteriori (MAP) algorithm.[1]

We hereafter demonstrate that the proposed reconstruction algorithm is able to most accurately and fastest find the sparse solution of an QAM image represented in wavelet domain, compared with the counterparts. Using the novel recovery method, three realizable scanning patterns are simulated to figure out the most relevant undersampling tactic for QAM image formation. For this simulation, three histological images were utilized; one acquired from human cornea tissue by SOS mode with 500 MHz and the others from human lymph node by SOS mode and impedance mode with 250 MHz. The visual and numerical results are presented, and we conclude this chapter by discussing the experimental results.

---

[1] An initial version of this algorithm was presented in [Hill 2016], but the work therein was focused on natural images.

3.2 Denoiser in AMP

The AMP algorithm can be interpreted as recursively solving an image denoising problem. The authors in [Som 2012, Tan 2015] have extended AMP by embedding various image denoising algorithms into the AMP iterative structure. To be more specific, AMP reconstructs an original image from the reduced number of linear measurements by performing elementwise denoising at each iteration as we reviewed in section 2.1.5.2. Thus at each AMP iteration, one obtains a noise perturbed original image. Reconstructing the image amounts to successive noise cancellations until the noise variance decreases to a satisfactory level. Fig. 3.1 visualizes the process to recover an undersampled image by iteratively removing noise with a denoising method (soft thresholding) within the wavelet based AMP framework. It is clearly witnessed that as the iteration number increases, the resulting images become closer to the original one.

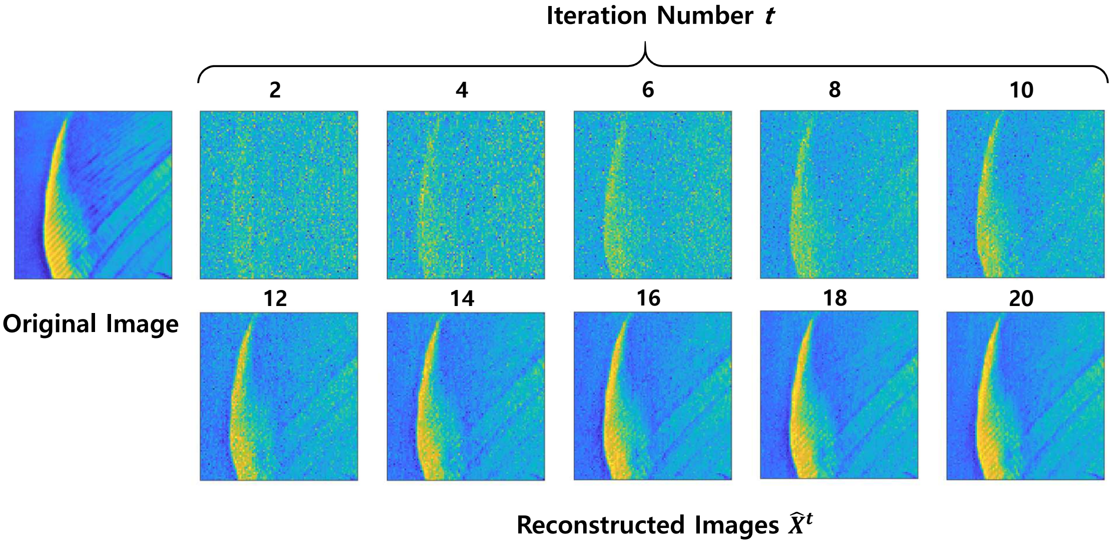

Figure 3.1: The figure shows the iterative denoising process to recover the original image (from Lena image) from 40% undersampled data within AMP reconstruction framework where the used denoiser is the soft thresholding function.

To solve (3.1), AMP iteratively implements the following two steps:

$$\mathbf{x}^{t+1} = \eta_t\left(\mathbf{\Phi}^{\mathbf{T}}\mathbf{z}^t + \mathbf{x}^t\right), \tag{3.2}$$

$$\mathbf{z}^t = y - \mathbf{\Phi}\mathbf{x}^t + \frac{1}{\delta}\mathbf{z}^{t-1}\left\langle \eta'_{t-1}\left(\mathbf{\Phi}^{\mathbf{T}}\mathbf{z}^{t-1} + \mathbf{x}^{t-1}\right)\right\rangle \tag{3.3}$$

where $\mathbf{x}, \mathbf{y}, \mathbf{z}$ and δ denote a sparse signal, observation, residual and undersampling ratio (M/N) respectively. $\eta(\cdot)$ is a function that represents the denoiser, $\eta'(\cdot)$ is its first derivative and $\langle \mathbf{x} \rangle = \frac{1}{N}\sum_{i=1}^{N}(x_i)$. The superscript t represents the iteration number and $(\cdot)^T$ is the classical conjugate transpose notation. Given that $\mathbf{x}$ is all zero vector and $\mathbf{z}$ is set to $\mathbf{y}$ as the initial conditions, the algorithm implements sequentially (3.2) and (3.3) until satisfying a stopping criterion or reaching a pre-set iteration number.

3.2.1 Model estimation of denoiser

From the observation in the Fig. 3.1, it is arguable that the most important consideration in AMP algorithm design consists in the choice of the robust and efficient shrinkage (denoising) function, η. A denoising function usually attempts to estimate the original PDF of signal via noise reduction on a transform domain which normally provides a sparse representation. Therefore, the performance of transform-domain based denoiser strongly relies on the distribution of coefficients that the transform function represents. For instance, wavelet transform is known as a effective method to attract the sparse characteristic of any signals or images present in the nature, and its coefficients are generally modeled as a heavy tailed Gaussian distribution. [Selesnick 2009] introduced the derivation process of the soft threshold function as the denoiser for a wavelet coefficients often modeled as a generalized (heavy-tailed) Gaussian [Simoncelli 1999], using maximum a posteriori (MAP) estimator. In the section 3.3, we will introduce the wavelet based Cauchy-AMP as the sparse reconstruction method, which is known to lead to heavier tails than the Gaussian density and has been derived in a similar way to the process described in [Selesnick 2009].

An extended wavelet-based AMP system can be generated by integrating a wavelet transform (denoted by W) into (3.2) and (3.3) using the following transformation.

$$\mathbf{y} = \mathbf{\Phi} \underbrace{W^{-1}\boldsymbol{\theta}_{\mathbf{x}}}_{\mathbf{x}} + \mathbf{n}, \tag{3.4}$$

where W^{-1} denotes the inverse wavelet transform of W, and $\theta_{\mathbf{x}}$ becomes the sparse representation of $\mathbf{x}$ within wavelet domain. Introducing $\mathbf{\Theta}$ as the new notation for $\mathbf{\Phi}W^{-1}$, we get the following expressions:

$$\theta_{\mathbf{x}}^{\mathbf{t+1}} = \eta_t\left(\mathbf{\Theta}^{\mathbf{T}}\mathbf{z}^{\mathbf{t}} + \theta_{\mathbf{x}}^{\mathbf{t}}\right), \tag{3.5}$$

$$\mathbf{z}^{\mathbf{t}} = \mathbf{y} - \mathbf{\Theta}\theta_{\mathbf{x}}^{\mathbf{t}} + \frac{1}{\delta}\mathbf{z}^{\mathbf{t-1}}\left\langle \eta_{t-1}'\left(\mathbf{\Theta}^{\mathbf{T}}\mathbf{z}^{\mathbf{t-1}} + \theta_{\mathbf{x}}^{\mathbf{t-1}}\right)\right\rangle. \tag{3.6}$$

Subsequently, the defined denoising algorithms seek to denoise the elements of $\theta_{\mathbf{q}}^{\mathbf{t}} = \mathbf{\Theta}^{\mathbf{T}}\mathbf{z}^{\mathbf{t}} + \theta_{\mathbf{x}}^{\mathbf{t}}$ corresponding to the contaminated wavelet coefficients. To simplify the following notation, the ith element of $\theta_{\mathbf{q}}^{\mathbf{t}}$ is defined as $\theta_{\mathbf{q},i}^{t} = v$ and the ith element of the denoised output $\theta_{\mathbf{x}}^{\mathbf{t+1}}$ is defined as $\theta_{\mathbf{x},i}^{t+1} = \hat{w}$ (a denoised estimate of the true coefficient

w). In the following, we review two previously defined denoising functions [Dabov 2007, Metzler 2016] which will be used as comparison methods in Section 3.4.

3.2.2 Soft Threshold (ST) denoiser

Soft threshold denoiser was adopted as the η function in the seminal AMP algorithm first proposed by [Donoho 2009].

$$\begin{aligned} \hat{w} = \eta(v) &= \operatorname{sign}(v)(|v| - \tau) \cdot \mathbb{1}_{(|v|>\tau)} \\ \eta^{'}(v) &= \mathbb{1}_{(|v|>\tau)} \end{aligned} \tag{3.7}$$

where $\mathbb{1}_{(\,\cdot\,)}$ is the indicator function, and τ denoting the threshold is defined as the M^{th} largest wavelet coefficient of $\theta_{\mathbf{q}}^{\mathbf{t}}$ when M is the number of measurement. Therefore, the coefficients less than τ are reckoned as noise and set to zero every iteration, otherwise shrunk as much as τ. The denoised coefficients $\hat{w}$ are used to update the residual $\mathbf{z}$ in the next iteration as shown in (3.6). The first derivative $\eta^{'}$ of the η function in the ST denoiser is equivalent to counting the number of non zero coefficients in the output of the η function, which is intuitively observed in Fig. 3.2.

3.2.3 Amplitude-scale-invariant Bayes Estimator (ABE) denoiser

$$\begin{aligned} \hat{w} = \eta(v) &= \frac{(v^2 - 3\sigma^2)_+}{v} \\ \eta^{'}(v) &= \mathbb{1}_{(v^2>3\sigma^2)} \cdot \left(1 + 3\left(\frac{\sigma}{v}\right)^2\right) \end{aligned} \tag{3.8}$$

where σ^2 is the noise variance at iteration t and $(\,\cdot\,)_+$ is the right handed function where $(u)_+ = 0$ if $u \leq 0$ and $(u)_+ = u$ if $u > 0$. As far as the CS reconstruction of conventional ultrasound images is concerned, the denoiser in (3.8) has proved to achieve better performance than IRLS and l_p programming [Kim 2016]. Therefore, we hypothesize that ABE should also be a successful solver for the reconstruction of QAM images, and consequently we shall use it for benchmarking our method. Fig. 3.2 illustrates the behavior of denoising for four different shrinkage functions, where ABE and the Cauchy-based denoisers (to be introduced in the subsequent section) can be regarded as a compromise between Soft-thresholding and Hard-thresholding [Figueiredo 2001]. The labels on the horizontal and vertical axes correspond to corrupted wavelet coefficient and their denoised version respectively. Subscript i represents the index of each element which implies element-wise denoising, as stated before.

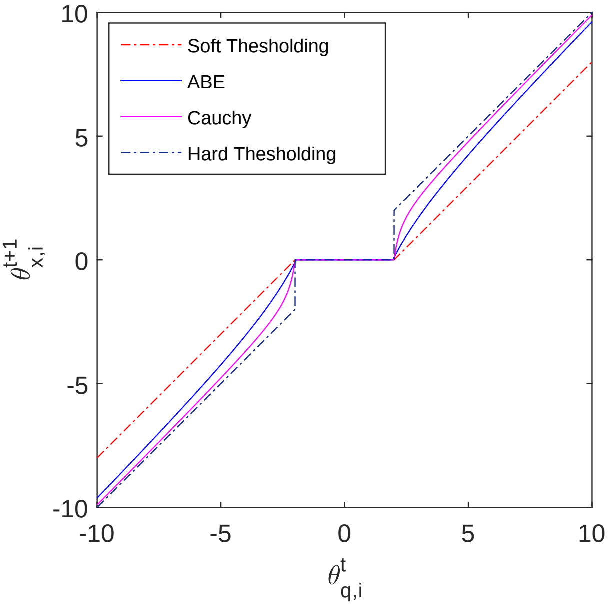

Figure 3.2: The comparison of behavior among four different denoisers.

3.3 Cauchy-AMP for compressed QAM imaging

This section describes the key features of wavelet-based Cauchy-AMP together with the practical sensing patterns as a novel approach for QAM CS reconstruction.

3.3.1 Wavelet based Cauchy-AMP

Wavelet coefficients provide a sparse representation for natural images. In addition, they can be accurately modeled using heavy tailed distributions such as the α-stable distribution [Achim 2001, Achim 2004]. The Cauchy distribution is a special case of the α-stable family which not only has a heavy tailed form but has a compact analytical probability density function given by [Hill 2016]:

$$P(w) = \frac{\gamma}{w^2 + \gamma^2}, \tag{3.9}$$

where w and γ are the wavelet coefficient value and the dispersion parameter (controlling the spread of the distribution) respectively. Given (3.9), a maximum *a posteriori* (MAP) estimator (3.10) can lead to the derivation of explicit formula to estimate a clean wavelet coefficient w from an observation v contaminated with additive Gaussian noise n having noise variance σ^2, *i.e.*, $v = w + n$.

$$\hat{w} = \arg\max_{w} P_{w|v}(w|v). \tag{3.10}$$

The posterior probability $P_{w|v}(w|v)$ can be expressed as (3.11) by means of Bayes' theorem, *i.e.*, $P_{w,v}(w,v) = P_{w|v}(w|v)P_v(v)$ and $P_{w,v}(w,v) = P_{v|w}(v|w)P_w(w)$.

$$P_{w|v}(w|v) = \frac{P_{v|w}(v|w)P_w(w)}{P_v(v)}. \tag{3.11}$$

Assuming $P_{v|w}(v|w) \sim N(0,\sigma^2)$ because $P_{v|w}(v|w)$ is equivalent to $P_n(v-w)$ of Gaussian noise [Selesnick 2009] and introducing the logarithmic form that is a monotonic function able to trace a peak point of $P_{w|v}(w|v)$, (3.10) is given in (3.12) which is mathematically more intuitive. The evidence $P_v(v)$ is constant for all inputs and therefore can be ignored.

$$\begin{aligned} \hat{w}(v) &= \arg\max_w \left[\log(P_{v|w}(v|w)P_w(w))\right] \\ &\overset{(a)}{=} \arg\max_w \left[-\frac{(v-w)^2}{2\sigma^2} + \log\left(P_w(w)\right)\right] \\ &= \arg\max_w \left[-\frac{(v-w)^2}{2\sigma^2} + \log\left(\frac{\gamma}{w^2+\gamma^2}\right)\right] \end{aligned} \tag{3.12}$$

where (a) comes from the Gaussianity assumption of $P_{v|w}(v|w)$, *i.e.*, $\frac{1}{\sigma\sqrt{2\pi}} \cdot \exp\left(-\frac{n^2}{2\sigma^2}\right)$ and the normalization constant is negligible. To find the solution to (3.12), take the first derivative of the terms in the bracket relative to w and set to zero:

$$\frac{v-w}{\sigma^2} - \frac{2w}{w^2-\gamma^2} = 0 \tag{3.13}$$

$$\hat{w}^3 - v\hat{w}^2 + (\gamma^2 + 2\sigma^2)\hat{w} - \gamma^2 v = 0 \tag{3.14}$$

Using Cardano′s formula, the estimate of w can be found in (3.15), the first derivative of which is (3.16).

$$\hat{w} = \eta(v) = \frac{v}{3} + s + t, \tag{3.15}$$

$$\hat{w}^{'} = \eta^{'}(v) = \frac{1}{3} + s^{'} + t^{'}, \tag{3.16}$$

where s and t are defined as:

$$\begin{aligned} s &= \sqrt[3]{\frac{q}{2} + dd}, \quad t = \sqrt[3]{\frac{q}{2} - dd} \\ dd &= \sqrt{\frac{p^3}{27} + \frac{q^2}{4}} \\ p &= \gamma^2 + 2\sigma^2 - \frac{v^2}{3} \\ q &= v\gamma^2 + \frac{2v^3}{27} - \frac{(\gamma^2 + 2\sigma^2)v}{3} \end{aligned} \tag{3.17}$$

s' and t' are found as follows:

$$\begin{aligned} s' &= \frac{q'/2 + dd'}{3(q/2 + dd)^{(2/3)}}, \quad t' = \frac{q'/2 - dd'}{3(q/2 - dd)^{(2/3)}} \\ dd' &= \frac{p'p^2/9 + q'q/2}{2dd}, \\ p' &= -\frac{2v}{3}, \\ q' &= -\frac{2\sigma^2}{3} + \frac{2\gamma^2}{3} + \frac{2v^2}{9} \end{aligned} \tag{3.18}$$

3.3.2 Practical sensing patterns for QAM

Random scanning schemes are theoretically optimal sensing modalities, but impractical for QAM data acquisition due to the intrinsic mechanical structure of the QAM system that a motor stage moves along a continuous path as stated previously. Therefore, in this thesis we investigated three practical sensing schemes, which can be easily implemented using servo motors. Firstly, the diagonal sensing schemes raster-scans oblique lines using a constant predefined angle which is used to vary the measurement rate, *i.e.*, a smaller angle leads to denser sampling. The row random sensing pattern, as the second suggestion, is a naive but practical attempt to preserve randomness. Data are collected using a practical raster scanning approach, but only on randomly selected rows. Finally, the spiral sensing scheme is also a practical sensing manner which originates in the center of area to be sampled and spreads out following a spiral pattern. The pace of the spreading is parameterized and used to prescribe the measurement rate.
Fig. 3.3 illustrates all sensing schemes used to sample data from a target composed of 256 × 256 pixel. A measurement rate of 20% is shown for all three schemes and the white pixels corresponds to the area to be spatially sampled.

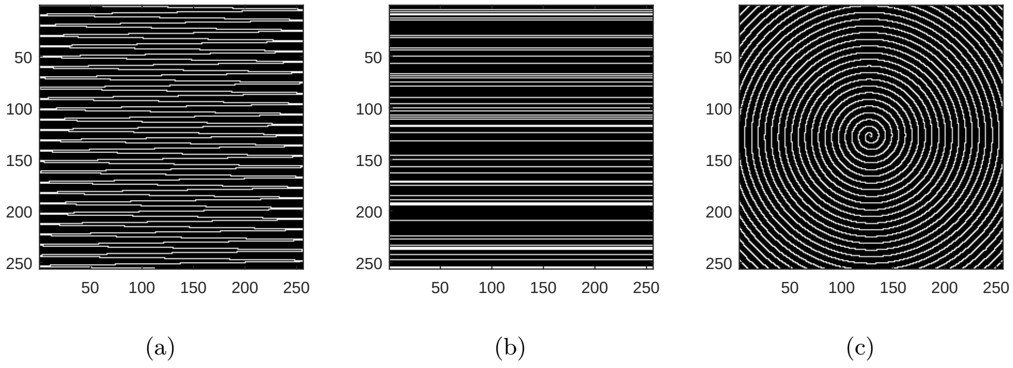

(a)

(b)

(c)

Figure 3.3: The proposed three different types of sampling masks, (a) Diagonal, (b) Row random and (c) Spiral.

3.4 Simulation results

Two different sets of experiments have been conducted and results are reported in Sections 3.4.1 and 3.4.2. The objective of the first set of experiments was to evaluate the performance of the proposed Cauchy-AMP algorithm. The second set of experiments shows the interest of the proposed sampling schemes in QAM and the ability of Cauchy-AMP algorithm to recover high quality images from the resulting under-sampled data. In addition to visual inspection, the peak signal to noise ratio (PSNR) and the structural similarity (SSIM) index [Wang 2004] were used to assess the quality of the reconstructed images by comparing them to the corresponding fully-sampled quantitative maps. SSIM is known as a perception-based metrics more suitable for disclosing the degradation or distortion of a recovered image.

$$\text{PSNR(dB)} = 10\text{log}_{10}\frac{\max(\mathbf{x},\hat{\mathbf{x}})^2}{\|\mathbf{x}-\hat{\mathbf{x}}\|} \tag{3.19}$$

$$\text{SSIM} = \frac{(2\mu_x\mu_{\hat{x}}+c_1)(2\sigma_{x\hat{x}}+c_2)}{(\mu_x^2+\mu_{\hat{x}}^2+c_1)(\sigma_x^2+\sigma_{\hat{x}}^2+c_2)} \tag{3.20}$$

where $\mathbf{x}$, $\hat{\mathbf{x}}$, μ and σ^2 denote an original image, recovered image, the mean of the data and the variance of the data respectively. c_1 and c_2 are variables to stabilize the division.

3.4.1 Simulation A: reconstruction results with random sensing schemes

The objective of this subsection is to validate the efficiency of the proposed Cauchy-AMP algorithm in comparison to alternative methods, previously proposed for CS reconstruction. Two of these were described in Section 3.2 and, while also AMP-based, they use ST and ABE as shrinkage functions in (3.2) and (3.3). In addition, we also compare to

conventional CS reconstruction algorithms, including the L1LS method and the IRLS algorithm for l_1-norm and ℓ_p minimization, respectively. These are succinctly outlined in the following:
L1LS (l_1-regularized Least Squares):
This l_1 based algorithm solves an optimization problem of the following form:

$$\min \|\Phi x - y\|^2 + \lambda \sum_{i=1} |x_i|, \tag{3.21}$$

where λ, a positive number, is a regularization parameter; set by cross validation to its best value, 0.01, in the results hereafter.
IRLS (iteratively reweighed least squares):

$$\hat{x} = \min_x \|x\|_p \quad \text{subject to} \quad y = \Phi x. \tag{3.22}$$

In the problem to estimate a sparse vector characterized by an alpha stable distribution, (3.22) finds a solution by solving an l_p norm minimization [Chartrand 2008]. Thus, in order to choose the optimum value of p in (3.22), we employed the approach described in [Achim 2010]. This approach was found to be superior to existing l_p solvers when applied to CS reconstruction of conventional ultrasound images.
In order to focus on evaluating the performance of the proposed reconstruction algorithm, the results in this subsection are obtained with two random sensing matrices known as ensuring the incoherence relationship with any transform domains: image projections on random Gaussian vectors and point-wise multiplication with Bernoulli vectors formed by uniformly random distributed zeros and ones.
Two experimental data volumes were used, from which impedance maps were estimated point-wise using the method in [Rohrbach 2017]. The first was acquired from a spatial-resolution target consisting of small bars of known width and spacing. Because the chrome used to form those bars is deposited using photolithography, the metal thickness (*i.e.*, ~ 0.12 μm) is much smaller than the wavelength at 250 MHz (*i.e.*, ~ 6 μm) and therefore only an effective acoustic impedance (z_{eff}) can be estimated. The amplitudes of the reflected signal (A) and the reference signal (B) were used to calculate z_{eff} using the following equation from the pressure reflection law [Kinsler 1999]:

$$z_{eff} = z_w \frac{(1 + R_{ref}\frac{A}{B})}{(1 - R_{Ref}\frac{A}{B})}, \tag{3.23}$$

where z_w is the known acoustic impedance of water and R_{ref} is the pressure reflection coefficient between water and glass slide:

$$R_{ref} = \frac{z_g - z_w}{z_g + z_w}, \tag{3.24}$$

where z_g is the known acoustic impedance of the glass slide. The second data volume was acquired from a 12-μm thick section obtained from a lymph node excised from a colorectal cancer patient using the 250-MHz QAM system. For both Gaussian and Bernoulli measurement matrices, the reconstruction results correspond to a measurement rate of 25%, *i.e.*, the ratio between the number of CS measurements and the number of pixels in the fully sampled QAM image.

Method	SSIM		PSNR (dB)	
	Lymph Node	USAF	Lymph Node	USAF
Cauchy	0.841	0.429	39.08	37.54
ABE	0.811	0.418	39.01	37.45
ST	0.724	0.380	38.41	35.95
IRLS	0.698	0.333	34.97	32.85
L1LS	0.457	0.290	32.14	31.30

Table 3.1: Numerical Results of recovery quality (Gaussian random sensing)

Method	Runtime (secs)	
	Lymph Node	USAF
Cauchy	3.32	3.47
ABE	2.86	3.00
ST	2.82	2.93
IRLS	62.88	333.61
L1LS	4.10	6.88

Table 3.2: The comparison of execution time: the averaged values over 30 trials

3.4.1.1 Gaussian random measurements

Figs. 3.4 and 3.5 illustrate the impedance images obtained with the five reconstruction algorithms from Gaussian random measurements. It highlights that IRLS and L1LS methods severely distorted the fully-sampled image compared to the AMP-based algorithms. By closely comparing the AMP-based methods, one may remark that Cauchy-AMP shows a tendency of noise removal with a slightly excessive smoothing effect, whereas ST-AMP and ABE-AMP suffer from several reconstruction artefacts. Table 3.1 regroups the PSNR and SSIM values corresponding to the results in Figs. 3.4 and 3.5. Additionally, Table 3.2 provides the runtime of the five methods, averaged over 30 trials. All the algorithms were implemented in Matlab R2014a environment and executed on a desktop computer equipped with a 2.6GHz Intel(R) CoreTM $i7-6500C$ processor with 8GB RAM. AMP algorithms outperform the two conventional recovery approaches IRLS and L1LS. Particularly, Cauchy-AMP yields the most accurate results compared to its AMP counterparts, at the cost of an execution time marginally higher than ABE-

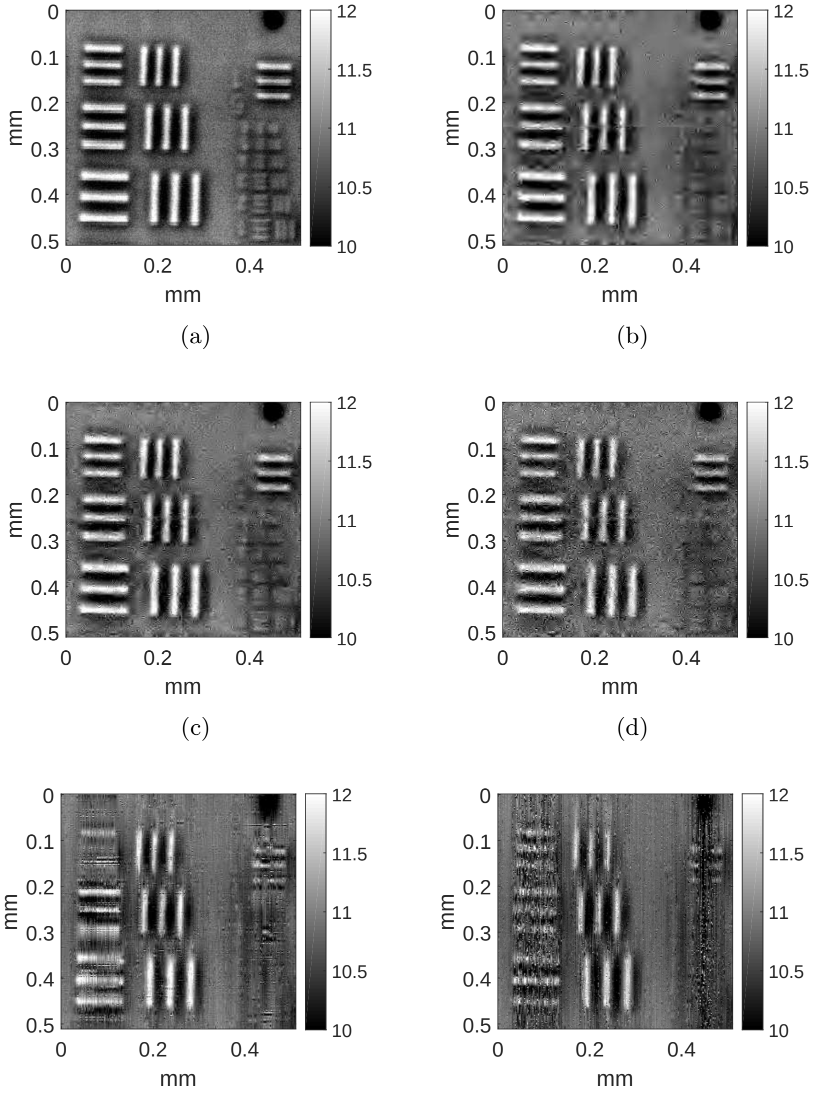

(a) (b)

(c) (d)

(e) (f)

Figure 3.4: (a) Fully-sampled impedance ($MRayl$) map estimated from RF data acquired on the USAF 1951 resolution test chart, reconstruction results from Gaussian random measurements for a measurement ratio of 0.25 with (b) proposed Cauchy-AMP, (c) ABE-AMP, (d) ST-AMP, (e) IRLS and (f) L1LS algorithms.

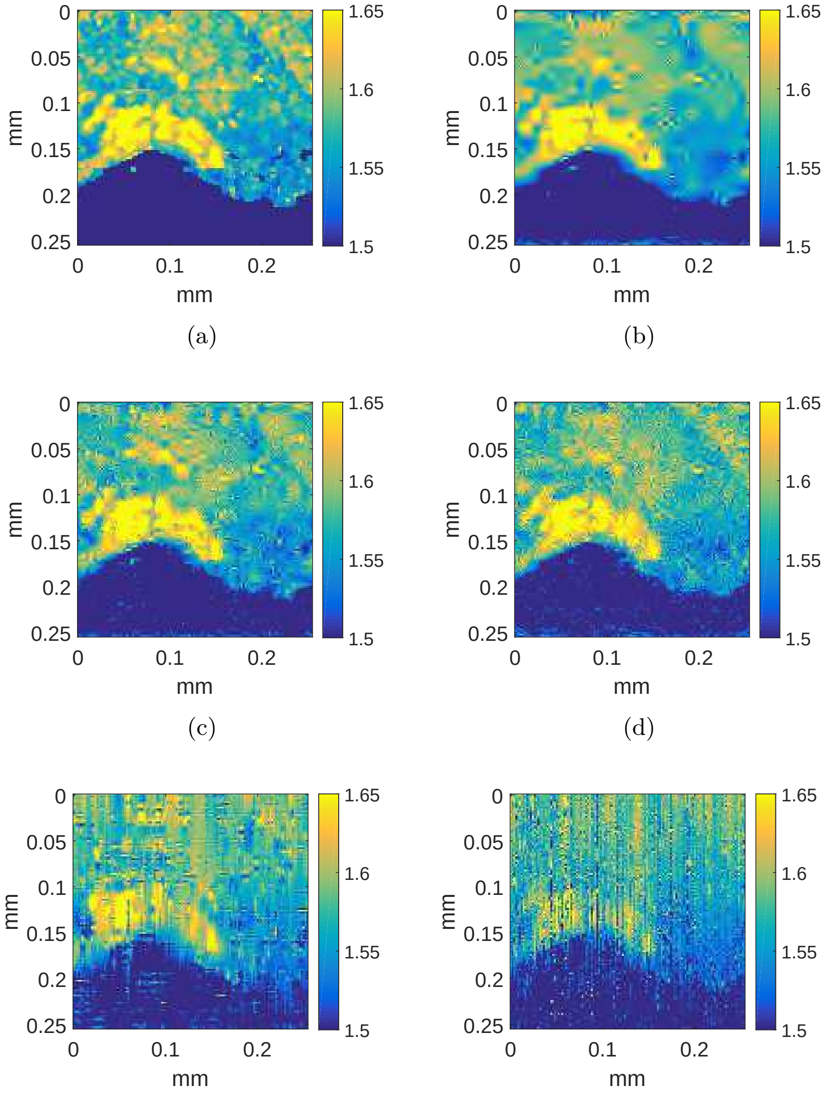

(a) (b) (c) (d) (e) (f)

Figure 3.5: (a) Human lymph node's fully-sampled impedance ($MRayl$) map representing a reconstruction results from Gaussian random measurements for a measurement ratio of 0.25 with (b) proposed Cauchy-AMP, (c) ABE-AMP, (d) ST-AMP, (e) IRLS and (f) L1LS algorithms.

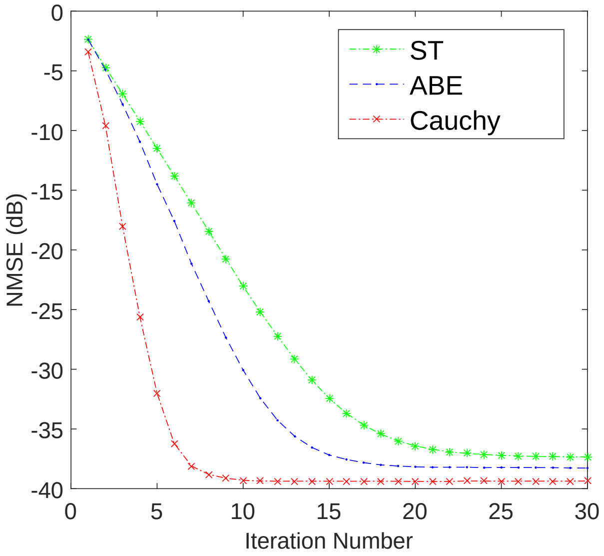

Figure 3.6: The comparison of NMSE according to iteration number for three AMP recovery methods: NMSE values are averaged over 30 simulated QAM images.

and ST-AMP. The execution time increase per iteration is explained by the number of parameters to be estimated during the denoising process. Indeed, Cauchy-AMP requires the estimation of an extra parameter compared to ST- and ABE-AMP,*i.e.*, the dispersion parameter γ in (3.9) which is updated at each iteration. Nevertheless, the extra computational cost per iteration is significantly mitigated by the faster convergence of Cauchy-AMP as revealed in Fig. 3.6.

3.4.1.2 Bernoulli random measurements

The above overall evaluation confirms that AMP-based algorithms are the most promising QAM recovery methods from under-sampled data. However, measurements obtained by linear projections on Gaussian vectors are not of practical use in QAM. As explained previously, QAM data is acquired point-wise by raster scanning the sample. Thus, Bernoulli random measurements corresponding to random spatial positions are further adapted to QAM acquisition system. Therefore, the three AMP-based methods are tested in this section on the same image used previously but on Bernoulli randomly sampled data. Similar to the previous results, the proposed Cauchy-AMP outperforms ABE- and ST-AMP algorithms. The three reconstructed images are shown in Figs. 3.7 and 3.8. The corresponding quantitative results are regrouped in Table 3.3.

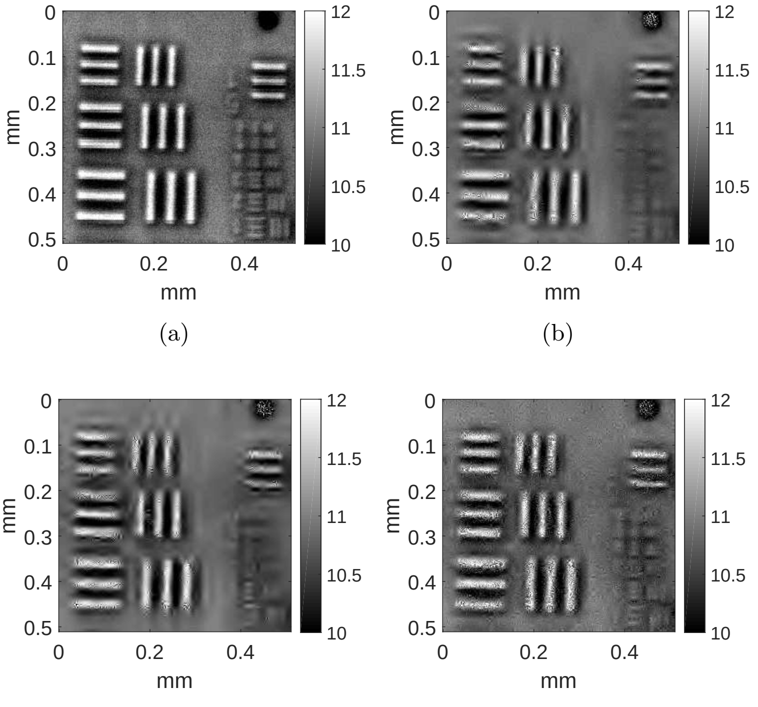

(a) (b)

(c) (d)

Figure 3.7: (a) Fully-sampled impedance ($MRayl$) map estimated from RF data acquired on the USAF 1951 resolution test chart, reconstruction results from Bernoulli random measurements for a measurement ratio of 0.25 with (b) proposed Cauchy-AMP, (c) ABE-AMP, (d) ST-AMP algorithms.

Method	SSIM		PSNR (dB)	
	Lymph Node	USAF	Lymph Node	USAF
Cauchy	0.851	0.424	38.72	34.56
ABE	0.837	0.417	38.56	34.33
ST	0.815	0.415	37.88	34.09

Table 3.3: Numerical Results of recovery quality (Bernoulli random sensing)

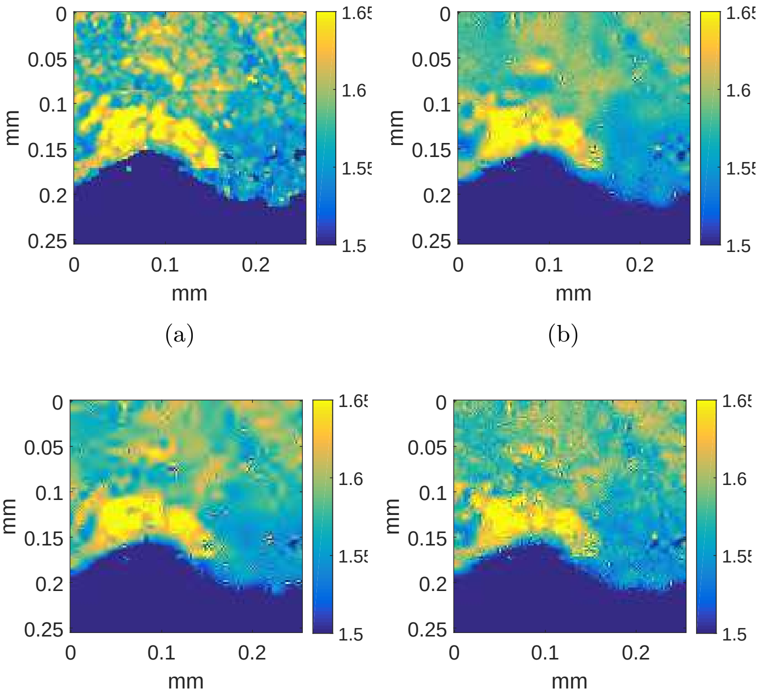

(a) (b)

(c) (d)

Figure 3.8: (a) Fully-sampled impedance ($MRayl$) map representing a reconstruction results from Bernoulli random measurements for a measurement ratio of 0.25 with (b) proposed Cauchy-AMP, (c) ABE-AMP, (d) ST-AMP algorithms.

3.4.2 Simulation B: reconstruction results with sensing schemes dedicated to QAM

The results shown in the previous section demonstrated, in the recovery of QAM image, the superiority of the proposed Cauchy-AMP algorithm to four well-established methods. However, Gaussian random measurements are impractical for QAM data acquisition. Similarly and although technically possible, it would be inefficient to move the transducer to transmit and receive ultrasound signals at spatial locations following a Bernoulli random measurements. Therefore, in this second set of simulations, the three AMP-based algorithms are employed to assess the relevance of the practical sensing patterns proposed in this study (see Section 3.3.2) for QAM imaging. The simulations used experimental results obtained from three real QAM maps. The first map corresponds to the SOS map obtained from a human cornea sample using the 500-MHz QAM system. The two other maps are SOS and impedance maps obtained using the 250-MHz QAM system on a human lymph node thin section obtained from a colorectal cancer patient. The fully sampled images correspond to standard raster scanning at conventional spatial scanning frequencies, resulting into a pixel size of 1 μm per 1 μm and of 2 μm per 2 μm for the 500 MHz and 250 MHz data respectively. All the AMP-algorithm investigations were performed using measurement ratios ranging from 20% to 60% of the data obtained using the conventional raster scanning approach. Blue regions in these images were not included in quantitative analyses because they were devoid of tissues. Figs. 3.9, 3.10 and 3.11 show the fully-sampled images and the ones recovered by the three algorithms from data generated with the three considered patterns for a measurement rate of 40%. Specifically, the results from the row random pattern show many artifacts appearing as “transverse” lines, and consequently this scheme is out of our interest. In contrast, the spiral and diagonal sensing patterns do not contain any visually-apparent artifacts. In order to determine which of these two sensing patterns performs better QAM recovery, one may observe Figs. 3.9-3.11 where the dense yellow area was better reconstructed using the spiral than the diagonal sensing pattern. Also for the sake of the quantitative evaluation to support the visual assessments, the numerical results are offered in the Table 3.4 and 3.5. From the tables, it can be seen that the spiral pattern combined with Cauchy-AMP based algorithm always provides the highest PSNR, followed by the diagonal pattern. Additionally, the PSNR values displayed in Fig. 3.12 compare the reconstruction qualities of the QAM images among the three proposed sensing patterns supported by Cauchy-AMP based algorithm with respect to the different measurement ratios ranging from 20% to 60%. In the whole range of measurement ratios, the spiral pattern scanning led to more accurate recovery than others. We discuss the implication of these results in section 3.5.

Along with the sensing ability to lead to the desirable recovery, another potential benefit of spiral pattern resides in significantly reduced scanning time. QAM estimation time is typically less important than QAM data acquisition time because tissue properties may change during scanning. Nevertheless, while the proposed AMP approach significantly decreases scanning time, it turns out that it also significantly decreases image formation time, because QAM parameter estimation is done independently on each RF line and is much more time consuming than AMP (cf. Table 3.2). For example, in the case of the 40% spiral, scanning time is reduced by more than 80% because in conventional raster scanning most of the time is spent accelerating and decelerating in each scan line, whereas the spiral is a smooth continuous curve which can be scanned at almost constant speed with servo motors. In addition, initial parameter estimation time is also reduced by 60% prior to the application of the AMP algorithm. The raster scanning and parameter estimation times for the lymph node example (Fig. 3.10 and Fig. 3.11) were approximately 20 and 15 minutes. The 40% spiral AMP approach would reduce these times to approximately 4 and 8 minutes.

Overall, these sets of simulations reveal that combining a spiral sensing pattern with a measurement ratio of 40%, and a Cauchy-AMP recovery is the best compromise between a practical spatial sampling pattern easily implementable with servo motors and image reconstruction quality for QAM imaging.

Image	Method	SSIM		
		SPIRAL	DIAGONAL	Y RANDOM
Conear 500MHz (SOS)	Cauchy	0.530	0.458	0.415
	ABE	0.509	0.435	0.393
	ST	0.502	0.373	0.306
Lymph Node 250MHz (SOS)	Cauchy	0.445	0.388	0.342
	ABE	0.438	0.374	0.323
	ST	0.418	0.351	0.301
Lymph Node 250MHz (Impedance)	Cauchy	0.911	0.884	0.868
	ABE	0.907	0.878	0.864
	ST	0.896	0.868	0.859

Table 3.4: Numerical results (SSIM) of recovery quality for the reconstructed images shown in Figs. 11, 12 and 13

3.5 Conclusions

In this chapter, a novel framework for compressive sampling reconstruction of QAM images was introduced, together with practically workable sampling patterns yet satisfying the theoretical requirement of CS.

We proposed and tested three compressive sampling measurement matrices, with a view of reducing both acquisition time and the amount of samples required, while taking into account the constraints imposed by the structure of current experimental QAM systems. We assessed the relative merits of diagonal, row random and spiral scanning as implementable patterns in designing a CS measurement matrix. When it comes to the results that the spiral pattern scanning showed the most advanced performance compared to other candidates, we carefully conjecture that the spiral sensing matrix may have lower

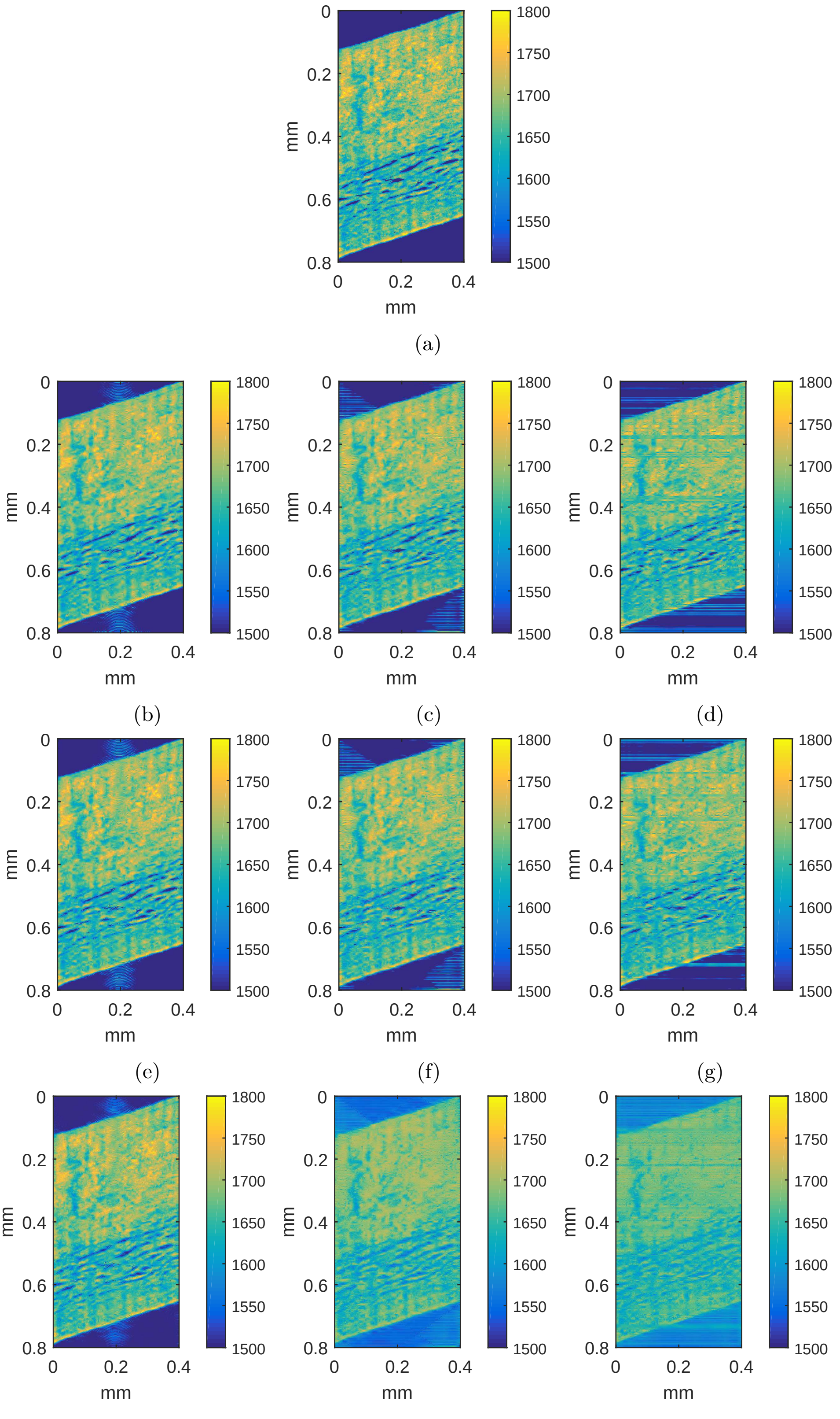

(a)

(b) (c) (d)

(e) (f) (g)

(h) (i) (j)

Figure 3.9: Reconstruction results of SOS (m/s) map estimated from human cornea data acquired at 500 MHz: (a) original fully sample data at pixel resolution of 1 μm per 1 μm, (b-d) reconstructed images with the proposed Cauchy-AMP algorithm for spiral, diagonal and row random sampling patterns, (e-g) reconstructed images with ABE-AMP algorithm for spiral, diagonal and row random sampling patterns, (h-j) reconstructed images with ST-AMP algorithm for spiral, diagonal and row random sampling patterns. All the results correspond to a measurement ratio of 40%.

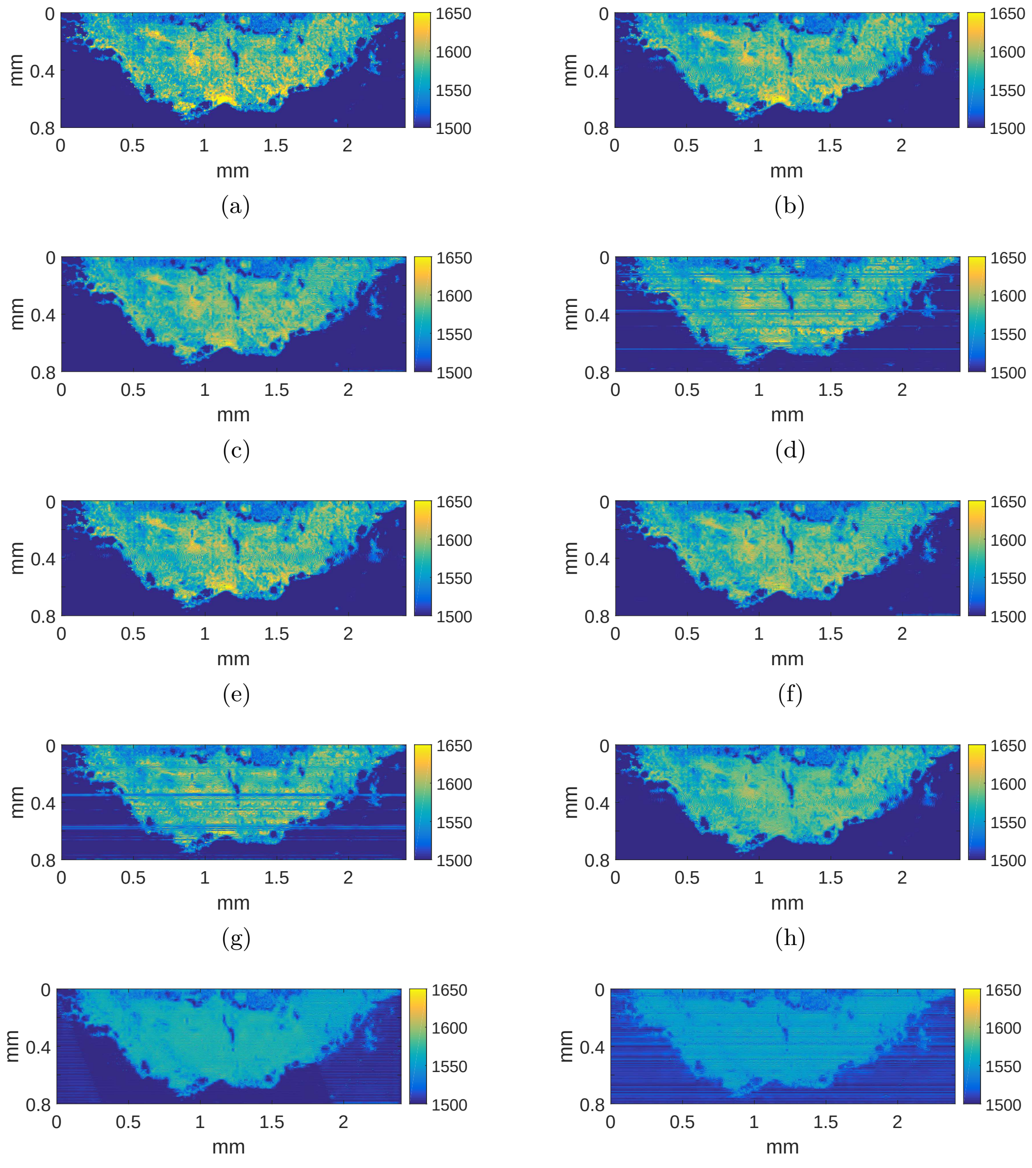

(a) (b) (c) (d) (e) (f) (g) (h) (i) (j)

Figure 3.10: Reconstruction results of SOS (m/s) map estimated from human lymph node data acquired at 250 MHz: (a) original fully sample data at pixel resolution of 2 μm per 2 μm, (b-d) reconstructed images with the proposed Cauchy-AMP algorithm for spiral, diagonal and row random sampling patterns, (e-g) reconstructed images with ABE-AMP algorithm for spiral, diagonal and row random sampling patterns, (h-j) reconstructed images with ST-AMP algorithm for spiral, diagonal and row random sampling patterns. All the results correspond to a measurement ratio of 40%.

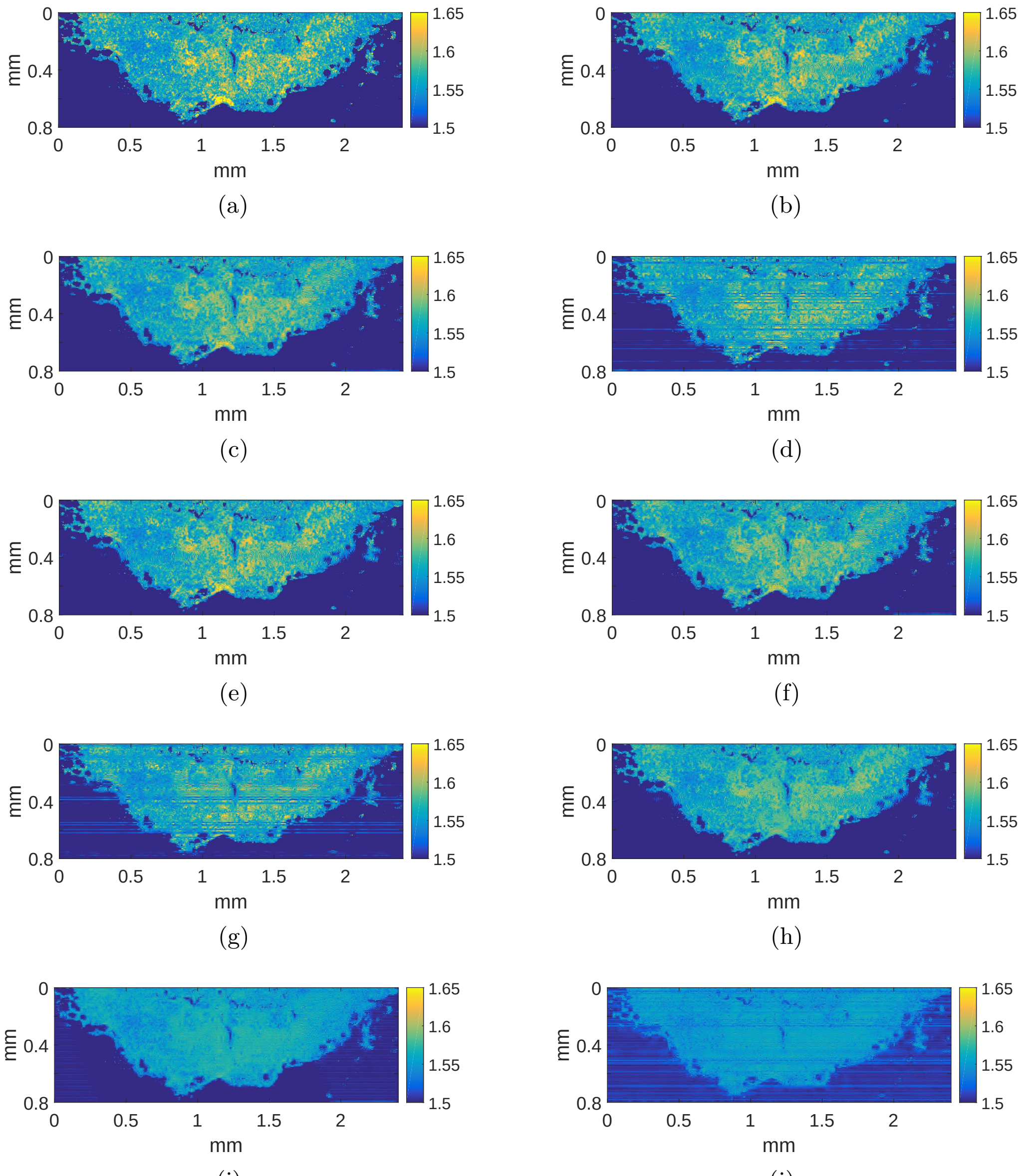

(a) (b) (c) (d) (e) (f) (g) (h) (i) (j)

Figure 3.11: Reconstruction results of impedance ($MRayl$) map estimated from human lymph node data acquired at 250 MHz: (a) original fully sample data at pixel resolution of 2 μm per 2 μm, (b-d) reconstructed images with the proposed Cauchy-AMP algorithm for spiral, diagonal and row random sampling patterns, (e-g) reconstructed images with ABE-AMP algorithm for spiral, diagonal and row random sampling patterns, (h-j) reconstructed images with ST-AMP algorithm for spiral, diagonal and row random sampling patterns. All the results correspond to a measurement ratio of 40%.

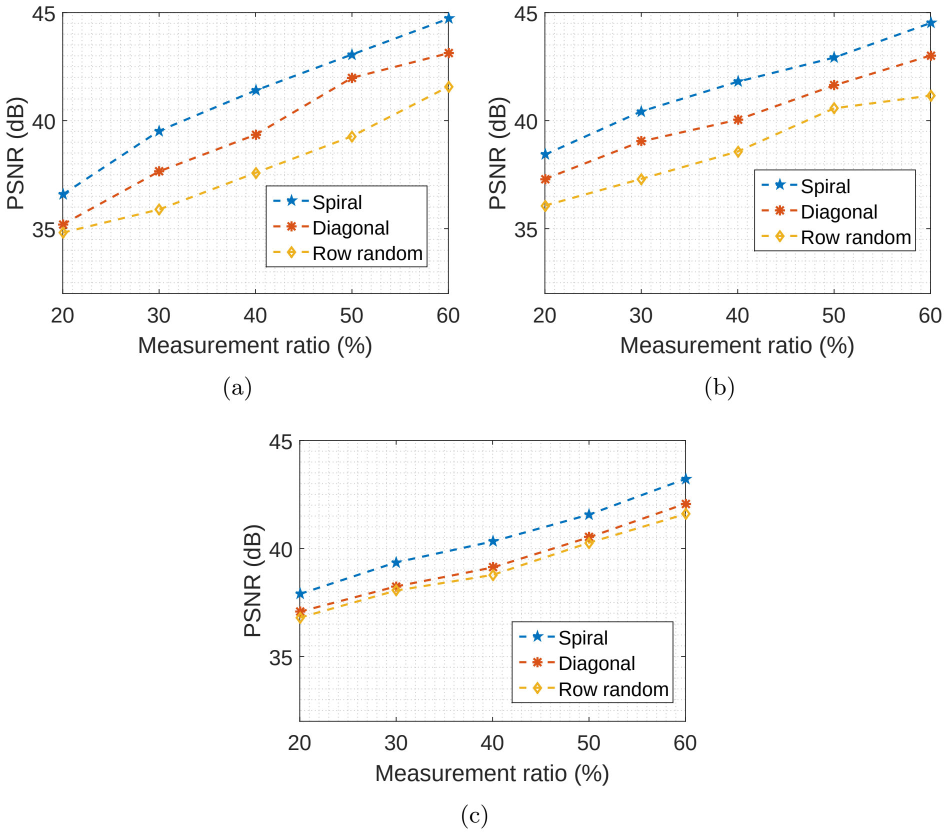

(a)

(b)

(c)

Figure 3.12: PSNR results as a function of the measurement rate, the sensing pattern (diagonal, random rows and spiral) and recovery algorithm (proposed Cauchy-AMP):(a), (b) and (c) are results of Cauchy denoiser with respect to respectively Human cornea at 500 MHz of SOS mode, Human lymph node at 250 MHz of SOS mode and Human lymph node at 250 MHz of impedance mode.

Image	Method	PSNR		
		SPIRAL	DIAGONAL	Y RANDOM
Conear 500MHz (SOS)	Cauchy	41.40	39.35	37.58
	ABE	40.97	39.03	37.54
	ST	40.54	37.39	35.28
Lymph Node 250MHz (SOS)	Cauchy	41.80	40.04	38.57
	ABE	41.42	39.72	37.95
	ST	40.22	34.50	36.53
Lymph Node 250MHz (Impedance)	Cauchy	40.32	39.12	38.27
	ABE	40.09	38.89	38.13
	ST	39.51	37.47	36.04

Table 3.5: Numerical results (PSNR) of recovery quality for the reconstructed images shown in Figs. 11, 12 and 13

coherence with wavelet transform than its counterparts. This perspective for the simulation results may open a possibility able to further improve the scanning manner proposed in this work by considering the incoherence relationship with a transform domain.

On the other hand, we adopted an approximate message passing strategy for the image reconstruction component of our framework, due to its comparable recovery fidelity to l_p minimization approaches. In particular, in the multiscale wavelet domain, a Cauchy-based MAP estimator was employed to perform the image denoising step as a core function for the recovery of a sparse solution within an AMP algorithm. We tested our methods in comparison with various compressive image reconstruction approach, and our results showed the superiority, in terms of the recovery quality and execution time compared to both alternative AMP techniques using different denoising strategies and classical approaches in CS framework namely, l_1-norm, or l_p minimization. The success of Cauchy denoiser should consist in the ability to faithfully estimate the heavy tailed distribution that the wavelet transform of QAM images shows. In this regard, the most attractive advantage of AMP algorithm can be said that its performance is able to be improved by testing other diverse conventional or emerging nonlinear shrinkage functions.

In the following chapter, we will show the QAM data acquisition making use of the cutting edge spare recovery approach in time domain.

Chapter 4

FRI-based AR model reconstruction for QAM RF signals

Part of the work in this chapter has been published in [Kim 2018b].

Contents

4.1 Introduction

This chapter demonstrates that finite rate of innovation (FRI) framework can be adopted to the QAM RF signals to achieve the exact recovery of the signals in time domain, and form acoustic parameter 2D maps *i.e.*, SOS, impedance and frequency attenuation with far less sampling rate than the traditional sampling approach. In particular, the novelty of this work is to show that the latter can be done by directly estimating the physical quantities of objects from the dramatically reduced number of samples without requiring the reconstruction of RF signals. The essence of the achievement lies in relating the outcome from FRI sampling to the construction of the autoregressive (AR) model [Rohrbach 2018].

This study is motivated by the inherent feature of QAM data acquisition that the distance between contiguous individual scanning points is constant, and determines a spatial resolution which depends on the center frequency of transducer; the higher frequency is, the smaller increment of scanning step size is. Thus, in order to yield a fine resolution microscopic image, recent researches on QAM technology have utilized enormously high frequencies approaching to even 500 MHz, and consequently the Analog to Digital Conversion (ADC) process demands much higher sampling frequency (*e.g*, 2.5 GHz relative to 250 MHz transducer) while complying with the classical sampling theorem.

In this regard, taking into account the fact that QAM RF signals can be parametrically expressed by two pulses varied with amplitude decay, time delay and frequency dependent attenuation of a known pulse, the low rate sampling based on the FRI manner could contribute to a significant reduction of the number of samples equivalent to the innovation rate in the context of FRI framework.

This work employs Sum of Sincs (SoS) kernel [Tur 2011] for carrying out the innovation rate sampling, which hands over the discrete Fourier coefficients of an input RF signal to AR estimator being in charge of determining the unknown model parameters to be used to compute the acoustic parameter 2D maps.

The collaboration of these two approaches allows the SOS and acoustic impedance 2D maps to be built with a few Fourier transform coefficients occupying only a small portion of whole spectrum, *e.g.*, 6 dB bandwidth. We perform the simulations with various sampling frequencies covering from the exact innovation rate of our QAM RF signal to the sampling rate corresponding to 12 dB of the input signal to find the smallest the number of samples not to cause the critical degradation of recovered 2D maps. The results from AR estimator are compared with those of annihilating filter method broadly hired as a reliable solver to the parameter estimation in contemporary FRI studies.

In conclusion, the implications and contributions of the results and are discussed.

4.2 Signal model

In QAM, RF signals consist of two primary reflections due to the water-tissue and tissue-glass interfaces as plotted with the continuous line in Fig. 4.1 (a). They can be modeled by the sum of two time-delayed, amplitude-decayed and frequency-dependent-attenuated versions of a reference RF pulse displayed with the dotted line in Fig. 4.1 (a). The non-attenuated reference pulse, denoted by $h(t)$ hereafter and corresponding to $S_0(t)$ in (1.13) is commonly measured at the same time, when the sample is scanned, from a region devoid of sample, *i.e.* presenting only one water-glass interface [Rohrbach 2017]. It is thus assumed to be known previously. The two frequency attenuated versions of h are denoted by $h^{(1)}$ and $h^{(2)}$ in time domain. Written in a τ-periodic version, the QAM RF signal model is as follows:

$$\begin{aligned} x(t) &= \sum_{m \in Z} \sum_{l=1}^{2} a_l h^{(l)}(t - \Delta t_l - m\tau) \\ &\overset{(a)}{=} \sum_{k \in Z} \left\{ \frac{1}{\tau} H\left[\frac{2\pi k}{\tau}\right] \sum_{l=1}^{2} a_l e^{\frac{-j2\pi k \Delta t_l - 2\pi k \beta_l}{\tau}} \right\} e^{\frac{j2\pi k t}{\tau}} \\ &\triangleq \sum_{k \in Z} X[k]\, e^{\frac{j2\pi k t}{\tau}}, \end{aligned} \tag{4.1}$$

where (a) is obtained applying the Poisson's summation formula [Porat 1997], β_l, a_l and Δt_l are the model parameters standing for the frequency attenuation coefficients, the amplitudes and the time delays respectively. In addition, the exponential terms in the second line, $e^{-j2\pi k \Delta t_l/\tau}$ and $e^{-2\pi k \beta_l/\tau}$, are caused by the phase shift and frequency attenuation. As a result, the unknown parameters to be identified are the set of $\{a_l, \Delta t_l, \beta_l\}_{l=1}^{2}$. Note that compared to the model in (2.26) representing a prototypical FRI signal, the QAM model has an additional degree of freedom associated with the frequency-dependent attenuation β_l. The unfamiliar parameter to the established FRI literature may require to introduce a different parameter estimation scheme from existing FRI recovery methods like annihilating filter or matrix pencil method. In section 4.4, we will attempt to find the model parameters using AR inverse model [Rohrbach 2018], and evaluate the recovery performance of the AR estimator and the annihilating filter with synthetic signals, where the results will demonstrate the validation of the proposed approach.

The last equality in (4.1) represents the Fourier series expansion of τ periodic signal $x(t)$, and the Fourier series coefficients $X[k]$ can be easily connected to the unknown parameters as follows:

$$X[k] = \frac{1}{\tau} H\left[\frac{2\pi k}{\tau}\right] \sum_{l=1}^{2} a_l e^{\frac{-j2\pi k \Delta t_l - 2\pi k \beta_l}{\tau}} \tag{4.2}$$

Assuming that one has access to $X[k]$, retrieving the unknown parameters from the sum of power series is closely related to the standard problem of identifying frequencies and amplitudes in spectral analysis [Stoica 2005].

The following sections explain how $X[k]$ can be obtained in practice, and the reconstruction method proposed is able to determine the parameters uniquely defining the QAM

RF signal model.

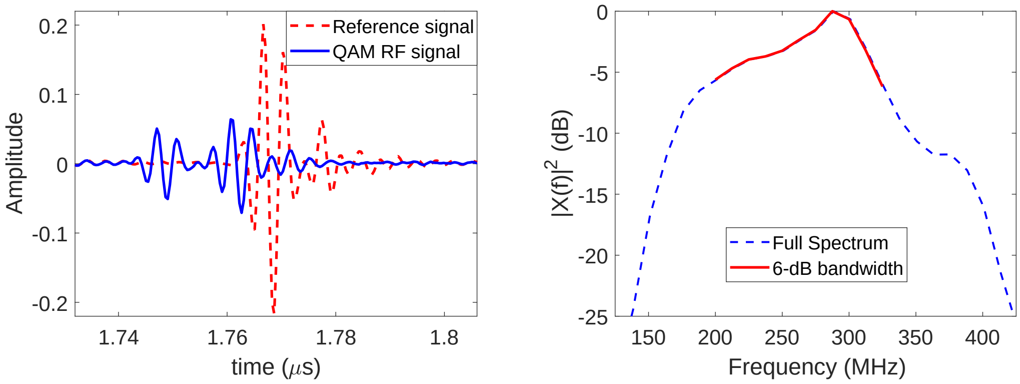

(a) (b)

Figure 4.1: (a) shows an example of reference and QAM RF signals in the time domain, (b) is the Fourier transform of the reference signal in (a), which is highlighted in the 6dB bandwidth with the red continuous line.

4.3 Sampling procedure

The sampling procedure used in this work was inspired by the one proposed in [Tur 2011] which proved that the data acquisition of ultrasound pulses could be an adequate application to FRI framework. The main idea is to uniformly sample the demodulated QAM RF signal using a compactly supported Sum of Sincs (SoS) sampling kernel and to relate these samples through a linear model to the Fourier series coefficients $X[k]$.

4.3.1 Sum of sinc (SoS) sampling kernel

In the Fourier domain, the SoS sampling kernel (denoted by $\varphi(t)$ in the time domain) is given by:

$$\Phi(\omega) = \frac{\tau}{\sqrt{2\pi}} \sum_{k \in \mathcal{K}} b_k sinc\left(\frac{\omega}{\frac{2\pi}{\tau}} - k\right), \tag{4.3}$$

where b_k is a smoothing function, and Hamming window, *i.e.*, $b_k = 0.54 - 0.46\cos\left(\frac{2\pi k}{\mathcal{M}}\right)$, was used in our experiments, which has a symmetric sequence ($b_k = b^*_{-k}$) of odd length $\mathcal{M}$, and thus leads to a real valued analog filter applicable to a continuous time domain. Furthermore, from the duality relationship between *sinc* and *rect* functions, (4.3) allows a time compact filter of τ support as:

$$\varphi(t) = rect\left(\frac{t}{\tau}\right) \sum_{k \in \mathcal{K}} b_k e^{j2\pi kt/\tau} \tag{4.4}$$

An example of SoS sampling kernel is plotted in Fig. 4.2 (a-b), in both temporal and frequency domains, where the applied sampling rate is 125 MHz corresponding to 11 samples over one period.

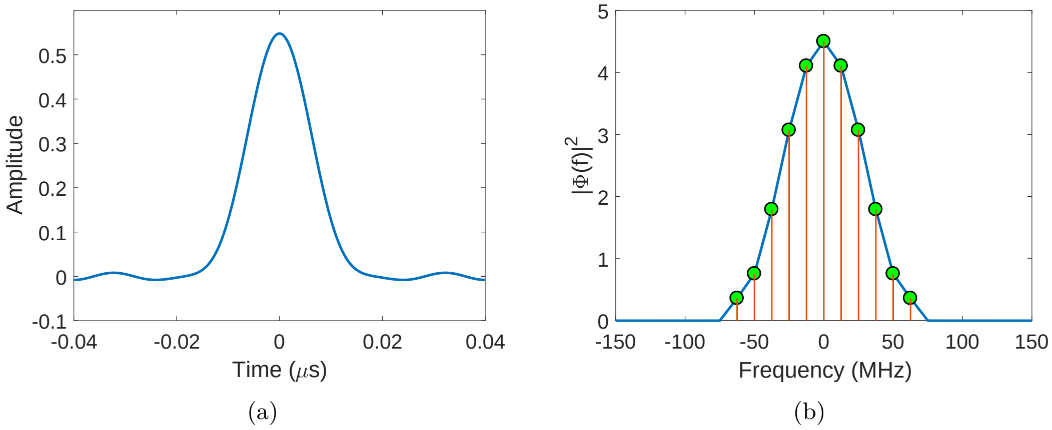

Figure 4.2: Example of SoS sampling kernel is illustrated in temporal (a) and frequency domain (b).

Note that the sampling kernel $\varphi(t)$ used within our sampling scheme is intrinsically a low pass filter, but the 6-dB bandwidth highlighted in Fig. 4.1 (b) to be sampled has the center frequency of 250 MHz. Therefore it should be shifted onto the baseband to be subjected to the low rate sampling. This requirement is accomplished by a standard I-Q demodulation [Kirkhorn 1999].

4.3.2 I-Q demodulation

The detail of the demodulation process is described in Fig .4.3. Fig. 4.3(a) is the Fourier transform of an input QAM RF signal, and (b-c) show two spectrums produced by the modulation where $f_{m_{1,2}}$ is a carrier frequency, and chosen considering the bandwidth of the RF signal to avoid the distortion of the spectrum by overlapping. (d-e) are obtained from lowpass filtering of previous signals (b-c), and (f) is formed by adding the two quadrature signals (d) and (e), the result of which is again modulated to be situated onto baseband as shown in (g). Finally, after the lowpass filtering, (h) is acquired. In the following developments, for the notational brevity, we regard $x(t)$ as the demodulated signal on behalf of $x_b(t)$ in Fig. (h).

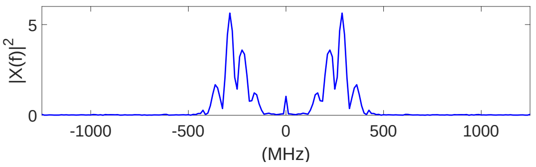

(a) $\mathcal{F}\{x(t)\}$

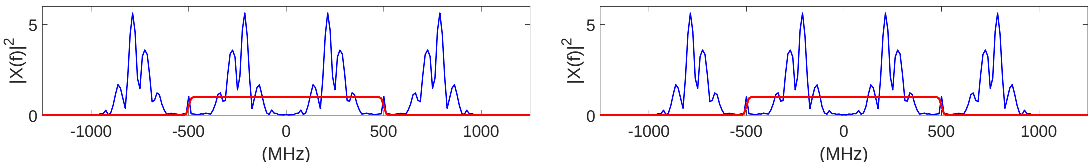

(b) $\mathcal{F}\{C(t) = x(t) \times cos(2\pi f_{m_1} t)\}$ (c) $\mathcal{F}\{S(t) = x(t) \times sin(2\pi f_{m_1} t)\}$

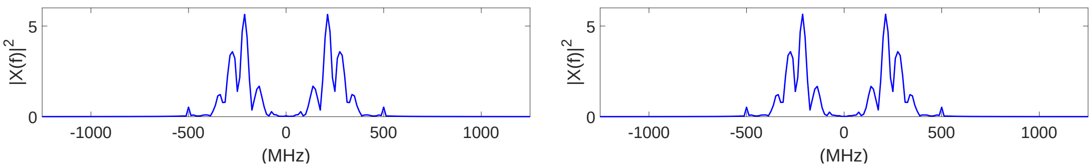

(d) $\mathcal{F}\{C_{LP}(t)\}$ (e) $\mathcal{F}\{S_{LP}(t)\}$

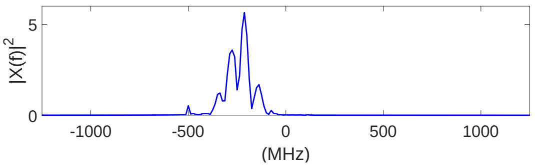

(f) $\mathcal{F}\{x_{iq}(t) = C_{LP}(t) + jS_{LP}(t)\}$

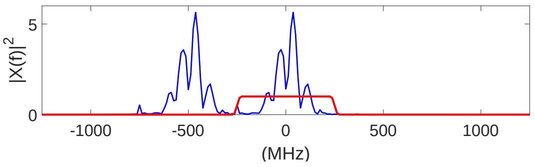

(g) $\mathcal{F}\{x_{sf}(t) = x_{iq}(t) \times cos(2\pi f_{m_2} t)\}$

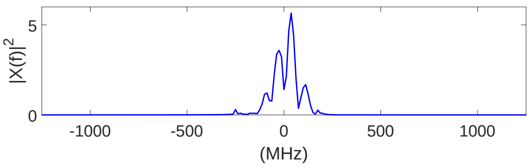

(h) $\mathcal{F}\{x_b(t)\}$

Figure 4.3: I-Q demodulation process is applied to an input RF signal $x(t)$, and the resulting spectrum of the process is located on the baseband as shown in (h). The red lines indicate low pass filtering.

4.3.3 Filtering and sampling

We denote by $x[n]$ the sampled version of $x(t)$ acquired with the sampling kernel $\varphi(t)$ and a sampling period T, which is defined as follows:

$$\begin{aligned} x[n] = \langle x(t), \varphi(t-nT)\rangle &= \int_{-\infty}^{\infty} x(t)\varphi^*(t-nT)dt \\ &\overset{(a)}{=} \sum_{k\in Z} X[k] \int_{-\infty}^{\infty} e^{\frac{j2\pi kt}{\tau}} \varphi^*(t-nT)dt \\ &\overset{(b)}{=} \sum_{k\in Z} X[k] e^{\frac{j2\pi knT}{\tau}} \int_{-\infty}^{\infty} e^{\frac{j2\pi kt}{\tau}} \varphi^*(t)dt \\ &\overset{(c)}{=} \sum_{k\in Z} X[k] e^{\frac{j2\pi knT}{\tau}} \varPhi^*\left[\frac{2\pi k}{\tau}\right] \end{aligned} \tag{4.5}$$

where (a) is obtained by substituting the Fourier series expansion form of $x(t)$ in (4.1), (b) results from a change of variable, and $\varPhi^*[2\pi k/\tau]$ in (c) denotes the discrete Fourier transform of $\varphi^*(t)$ evaluated at $[2\pi k/\tau]$. The superscript " $*$ " stands for complex conjugate. One may observe from (4.3) that $\varPhi^*[2\pi k/\tau]$ is different from zero only for k's belonging to a finite set $\mathcal{K}$ as follows [Tur 2011]:

$$\varPhi\left[\frac{2\pi k}{\tau}\right] = \begin{cases} 0, & k \notin \mathcal{K} \\ \text{nonzero}, & k \in \mathcal{K} \\ \text{arbitrary}, & otherwise \end{cases} \tag{4.6}$$

Then the summation in the last line of (4.5) becomes finite ($k \in \mathcal{K}$ instead of $k \in Z$), and can be rewritten as in (4.7). This nice property can be supported by any kernel $\varphi(t)$ satisfying the Strang-Fix condition elaborated in section 2.2.3.1.

$$x[n] = \sum_{k\in\mathcal{K}} X[k] e^{\frac{j2\pi knT}{\tau}} \varPhi^*\left[\frac{2\pi k}{\tau}\right] \tag{4.7}$$

Fig. 4.4 (a-c) display, in time and frequency, the process being filtered with a SoS kernel and uniformly decimated at an innovation rate with respect to an I-Q demodulated RF signal.

4.3.4 Estimation of Fourier coefficients

The first step to estimate the model parameters of the QAM RF signal sampled at the innovation rate is to recover the discrete Fourier coefficients $X[k]$ as described in the following.

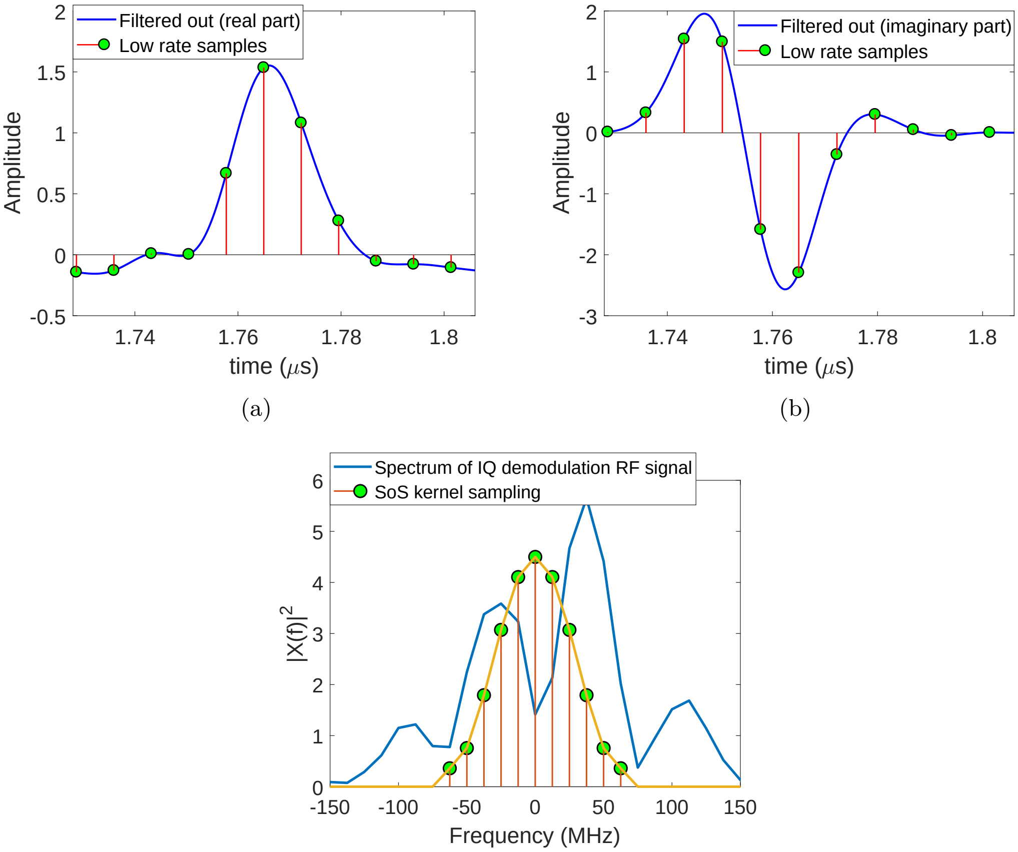

(a)

(b)

(c)

Figure 4.4: (a), (b) and (c) show respectively real and imaginary parts in time domain, and the spectrum in frequency domain after filtering and uniform sampling the demodulated RF signal using the SoS sampling kernel, where the applied innovation rate is 125 MHz (equivalent to 11 samples over one period).

(4.7) can be recast as a matrix-vector form as follows:

$$\boldsymbol{\chi} = \mathbf{VGX} \tag{4.8}$$

where $\boldsymbol{\chi}$ and $\mathbf{X}$ are column vectors that gather respectively the discrete samples $x[n]$ of the length $\mathcal{N}$ and the Fourier coefficients $X[k]$ of the length $\mathcal{M}$. On the other hand, $\mathbf{V}$ and $\mathbf{G}$ are a $\mathcal{N} \times \mathcal{M}$ Vandermonde matrix having $e^{\frac{j2\pi knT}{\tau}}$ as (nk)th elements and a $\mathcal{M} \times \mathcal{M}$ diagonal matrix with $\Phi^*(\frac{2\pi k}{\tau})$ as main diagonal entries respectively. From (4.8), the Fourier series coefficients $\mathbf{X}$ can be computed algebraically from the prior knowledge $\mathbf{G}$ and the measurement $\boldsymbol{\chi}$ as follows:

$$\mathbf{X} = \mathbf{G}^{-1}\mathbf{V}^{\dagger}\boldsymbol{\chi} \tag{4.9}$$

where $(\,\cdot\,)^{\dagger}$ denotes the Moore-Penrose pseudoinverse of $(\,\cdot\,)$, and $\mathbf{V}$ is left invertible as far as $\mathcal{N} \geq \mathcal{M}$. Moreover, provided that $\mathcal{N} = \mathcal{M}$ and $T = \tau/\mathcal{N}$, the Vandermonde matrix $\mathbf{V}$ can be the discrete Fourier transform (DFT) matrix with respect to $\boldsymbol{\chi}$. Thus, the following operation is also possible for determining $\mathbf{X}$:

$$\mathbf{X} = \mathbf{G}^{-1}DFT(\boldsymbol{\chi}) \tag{4.10}$$

The retrieved Fourier coefficients $\mathbf{X}$ is modulated again to restore the phase distorted by I-Q demodulation. Additionally, if we consider a real implementation, the re-modulation process would be simply completed by a phase shift in digital configuration. In the remaining reconstruction process, $X[k]$ plays a pivotal role to estimate the unknown model parameters in (4.2).
Fig. 4.5 evaluates the accuracy of the Fourier coefficients estimated by the introduced method adopting the innovation rate, *i.e*, 125 MHz via the comparison with those computed by the conventional sampling scheme using 2.5 GHz separately in the real and imaginary parts. The illustrative results demonstrate that there is no visually perceptible discrepancy caused by the FRI estimation method. Table 4.1 shows the average and the standard deviation (over $10,000$ recovered signals) of the normalized root mean squared error relative to the above results. Overall, the numerical comparison confirms that the Fourier coefficients are estimated nearly perfectly, which is consistent with the qualitative observations of Fig. 4.5. Evidently, it can be expected that the accurate recovery of the Fourier coefficients will contribute to the exact estimation of the model parameters as revealed in the following section. In addition, it turns out that the estimation error depends on the design of the SoS sampling kernel, in particular being affected by the selection of the window function, *i.e.* b_k's in (4.3), and the strategy for finding the optimal window coefficients is referred to in [Tur 2011].

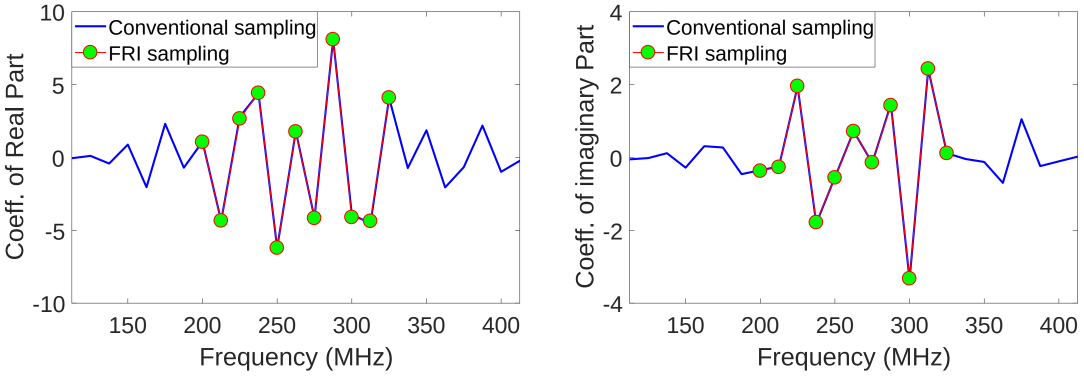

(a) (b)

Figure 4.5: Real parts (a) and imaginary parts (b) of FT coefficients estimated from FRI sampling scheme (11 samples, *i.e.* 125 MHz) are overlapped on the FT coefficients acquired by conventional sampling (200 samples, *i.e.* 2.5 GHz).

Number of samples	Sampling frequency (MHz)	Fraction of Nyquist rate (800 MHz) in %	Real part of FT coefficients		Imaginary part of FT coefficients	
			NRMSE	STD.	NRMSE	STD.
7	75	9.4	0.0137	0.0063	0.0064	0.0020
9	100	12.5	0.0126	0.0055	0.0062	0.0021
11	125	15.6	0.0132	0.0048	0.0067	0.0022
13	150	18.8	0.0116	0.0057	0.0060	0.0028
15	175	21.9	0.0100	0.0045	0.0058	0.0023
17	200	25.0	0.0090	0.0037	0.0056	0.0023
19	225	28.1	0.0089	0.0034	0.0059	0.0022
21	250	31.2	0.0089	0.0032	0.0058	0.0022

Table 4.1: The average and standard deviation of normalized root mean squared error (over 10,000 recovered signals) with respect to real and imaginary parts of FT coefficients retrieved from various innovation rates

4.4 Reconstruction method

In QAM, the acoustic parameters of the scanned tissue are acquired from the formulae supported by amplitudes, time delays and frequency attenuation coefficients, which are estimated in each RF signal reflected from each spatial location. To be more specific, the model parameters will be determined by the AR inverse model requiring the small set of Fourier coefficients of RF signals, which is detailed in what follows.

4.4.1 Auto regressive (AR) estimator

The discrete Fourier coefficients, estimated from a few samples taken by SoS kernel in previous section, are converted into a normalized form by dividing $X[k]$ by $\frac{1}{\tau}H[2\pi k/\tau]$ in (4.11), which is denoted by N_k and consequently contains only the terms associated with the model parameters to be identified as:

$$\begin{aligned} N_k &= \sum_{l=1}^{n} a_l \{\exp[2\pi\Delta f(-\beta_l - j\Delta t_l)/\tau]\}^k \\ &= \sum_{l=1}^{n} a_l \lambda_l^k, \end{aligned} \tag{4.11}$$

where Δf and n are the step size leading to discrete frequencies, *i.e.* $f_k = k\Delta f$ and the number of pulses to be reconstructed respectively, and λ_l stands for $\exp[2\pi\Delta f(-\beta_l - j\Delta t_l)/\tau]$. Taking into account the ultimate objective of our problem setting, one may notice that the parameters of the QAM RF signal model in (4.1) can be straightforwardly estimated by solving (4.11) without the need of reconstructing an original signal. The estimation is accomplished making use of an AR model which, unlike the previous setup in (4.2), supposes that QAM RF signals are composed of more than two reflections ($n \geq 2$) in order for providing robustness and stability to noise and estimation artifacts. Introducing the error term and the AR coefficients denoted by respectively ϵ and s, the AR inverse model for QAM proposed is formulated as follow:

$$N_k = \sum_{i=1}^{n} s_i N_{k-i} + \epsilon_k, \tag{4.12}$$

For the practical implementation, (4.12) is rewritten in matrix-vector form as:

$$\mathbf{n} = -\mathbf{R}\mathbf{s} + \boldsymbol{\epsilon}, \tag{4.13}$$

where provided that the normalized coefficients N_k are computed at the frequencies ranging from $k_{\max}\Delta f$ to $k_{\min}\Delta f$, $\mathbf{n}$ is the column vector of length $(k_{\max} - k_{\min} + 1)$ representing the values of N_k from $k_{\min}$ to $k_{\max}$, $\mathbf{R}$ is the matrix of size $(k_{\max} - k_{\min} + 1)$ by n whose entries are determined by N_{k-i}, and $\boldsymbol{\epsilon}$ is the column vector of length $(k_{\max} - k_{\min} + 1)$ composed of the values ϵ_k from $k_{\min}$ to $k_{\max}$. Together with the process to find the AR coefficients $\mathbf{s}$, the remaining steps regarding further derivations to reach our final goal basically follow the previous study in [Rohrbach 2018], which is also detailed in Appendix A. Therefore in what follows, we briefly summarize the remaining process. The AR model coefficients s_i are estimated by solving (4.13) with a least-square approach. Then, the coefficients λ_l are determined by the roots of polynomials formed from the AR model coefficients s_i. Subsequently, the coefficients a_l are obtained as a solution to (4.11) using a least-square approach.

Among the n pairs of λ_l and a_l estimated, we select the most relevant two sets of parameters corresponding to the echoes reflected from the water-tissue and tissue-glass interfaces. Choosing the parameter sets related to the two desirable pulses are achieved through the comparison with the time instance and amplitude of the reference pulse $h(t)$ or measuring the standard cross-correlation between $h(t)$ and single pulses formed by the p sets of parameters. The determined model parameters $\{a_l, \lambda_l\}_{l=l}^{2}$ are eventually utilized to estimate acoustic parameters in 4.4.3. The process that the AR inverse model estimates the unknown parameters from the compressed measurements is resumed in Algorithm 1.

Prior to the construction of acoustic 2D maps, we investigate the recovery fidelity of the proposed FRI-AR approach comparing with the annihilating filter technique in the following section.

Algorithm 1 FRI-based AR estimator

```
    Input: $N_k$
    Output: $\{\lambda_l, a_l\}_{l=1}^{2}$
Build the AR model, $N_k = \sum_{m=1}^{n} s_m N_{k-m} + \epsilon_k$
Estimate AR coefficients $s_m$ by least square error
Determine $\lambda_l$ as the roots of $P(z) = 1 + \sum_{m=1}^{p} s_m z^m = \prod_{m=1}^{n}(1 - \frac{1}{\lambda_m} z^{-1}) = 0$
Compute $a_l$ by solving $N_k - \sum_{l=1}^{n} a_l \lambda_l^k \approx 0$
Select two sets of $\{\lambda_l, a_l\}_{l=1}^{n}$ corresponding to $h_1$ and $h_2$
```

4.4.2 Evaluation of recovery quality of RF signal

We herein demonstrate the superiority of estimation performance of the proposed FRI-AR approach to the annihilating filter method using synthetic signals suffered by noise perturbation. The experimental signals are artificially produced by adapting arbitrary model parameters $\{\Delta t_l, a_l, \beta_l\}_{l=1}^{2}$ to a modulated Gaussian pulse $h(t) = \exp[-(t - t_0)^2/\sigma_g^2] \cdot \cos 2\pi t f_c$ on the basis of (4.1), where σ_g and f_c emulate the dispersion of the echo pulse and the center frequency of a transducer, and the time duration t is set to the range from 0 to 1 second for the computational convenience, and thus $\tau = 1$. The estimation process of the existing method to obtain the set of model parameters is briefly explained in what follows.

N_k in (4.11) is firstly denoised by TLS-Cadzow routine described in section 2.2.4.2, and annihilating filter $\mathcal{A}$ is acquired by finding a sequence of coefficients to null out Toeplitz matrix formed by the denoised N_k. The roots u_l of $\mathcal{A}$ are computed, and t_l and β_l are estimated considering phase and magnitude parts respectively from the complex values u_l. Lastly, a_l is estimated as a solution of least square error to (4.11). This is summarized on the Algorithm 2. Furthermore, in order to reduce the estimation error in the noisy situation, the denoising technique applied above entails oversampling [Dragotti 2007, Urigüen 2013a]. Thus instead of the degree of freedom corresponding to $\{t_l, a_l, \beta_l\}_{l=1}^{2}$ in our parametric model, we acquired 11 samples considering the 6dB

range of the signal. The test results were compared with those of our proposed approach elaborated in the previous section. The recovery trials for the two different methods was performed 100 times with respect to the synthetic signal corrupted with additive white Gaussian noise of SNR(dB) ranging from 5 to 30. The desired noise levels are given by Gaussian noise with variance σ_n^2 from $SNR = \frac{1}{N} \parallel \hat{x} \parallel_2^2 / \sigma_n^2$ when $\hat{\mathbf{x}}$ is a clean sample.
In Fig. 4.6(a-d) depict the synthetic signals recovered at the specific SNR levels, and on the other hand Fig. 4.6(e-f) are the results from the simulation applied to a real QAM RF signal. Fig. 4.7 compares the performance between two methods illustrating the average of root mean square errors computed at every noise level. As observed in the graphical results, as far as the noise perturbation is concerned, it is evident that the AR estimator is much more optimized solution to the parameter estimation of QAM RF signal than the typical FRI recovery manner.
The following section provides the resulting acoustic 2D maps formed by the proposed framework.

Algorithm 2 Annihilating filter with Cadzow denoising

```
Input: $N_k$
Output: $\{t_l, \beta_l, a_l\}_{l=1}^2$
1: Build Toeplitz matrix $S$ with $N_k$
2: Implement TLS-Cadzow routine for $S$
3: Obtain the annihilating filter coefficients $(\mathcal{A})$ by solving $\widetilde{S}\mathcal{A} \approx 0$
4: Compute the roots $u_l$ of $(\mathcal{A})$, $u_l = real(u_l) + imag(u_l) = \exp[(-j2\pi t_l - 2\pi\beta_l)/\tau]$
5: Estimate $t_l$ from $angle(u_l)/2\pi = t_l$ and $\beta_l$ from $abs(u_l) = \exp[-2\pi\beta_l/\tau]$
6: Estimate $a_l$ as the solution of LSE to (4.11)
```

4.4.3 Computation of acoustic parameters

From λ_l and a_l estimated in the previous sections, SOS ($\boldsymbol{c}$), acoustic impedance ($\boldsymbol{Z}$) and attenuation ($\boldsymbol{\alpha}$) are computed, and additionally the subscripts 1 and 2 are matched with the first interface (water-tissue) and the second interface (tissue-glass). Firstly, Δt_l and β_l are obtained by breaking down λ_l (defined in (4.11)) into real and imaginary parts as:

$$\Delta t_1 = \frac{\text{imag}(\log(\lambda_1))}{\Delta f}, \quad \Delta t_2 = \frac{\text{imag}(\log(\lambda_2))}{\Delta f} \tag{4.14}$$

$$\beta_1 = \frac{\text{real}(\log(\lambda_1))}{\Delta f}, \qquad \beta_2 = \frac{\text{real}(\log(\lambda_2))}{\Delta f} \tag{4.15}$$

Given that $\boldsymbol{c}_w$ is the known SOS in the water used as a coupling fluid between the transducer and the sample, the thickness ($\boldsymbol{d}$) of sample at a point irradiated by US

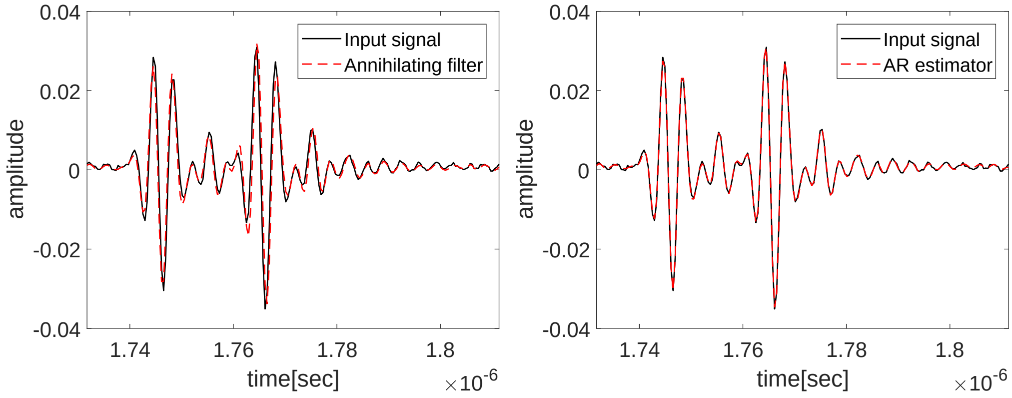

(a) SNR of 30 dB (b) SNR of 30 dB

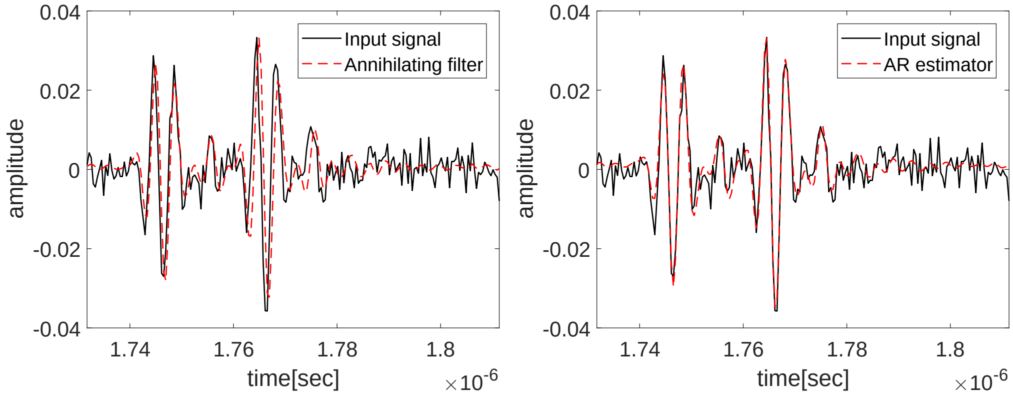

(c) SNR of 9 dB (d) SNR of 9 dB

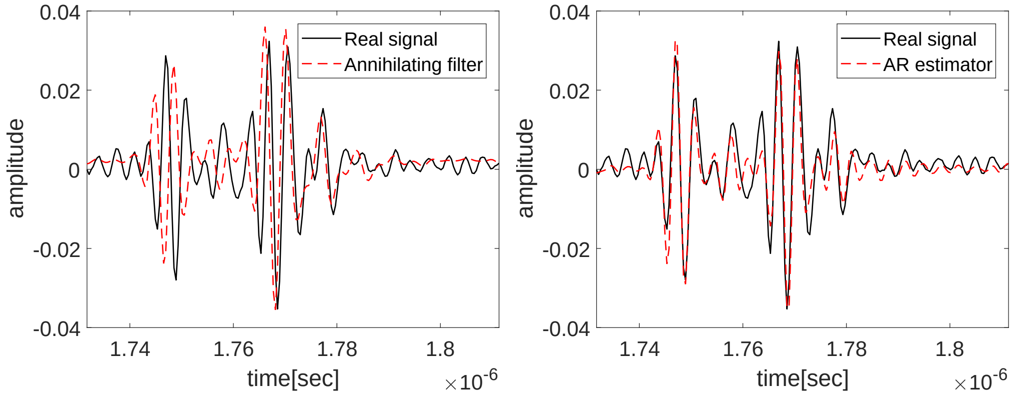

(e) Real QAM RF (f) Real QAM RF

Figure 4.6: (a-d) Reconstruction results with AR model and annihilating filter method for a synthetic signal corrupted by an additive white Gaussian noise corresponding to (a-b) 30dB and (c-d) 9 dB, (e-f) reconstructed experimental QAM RF signal with AR-model and annihilating filter.

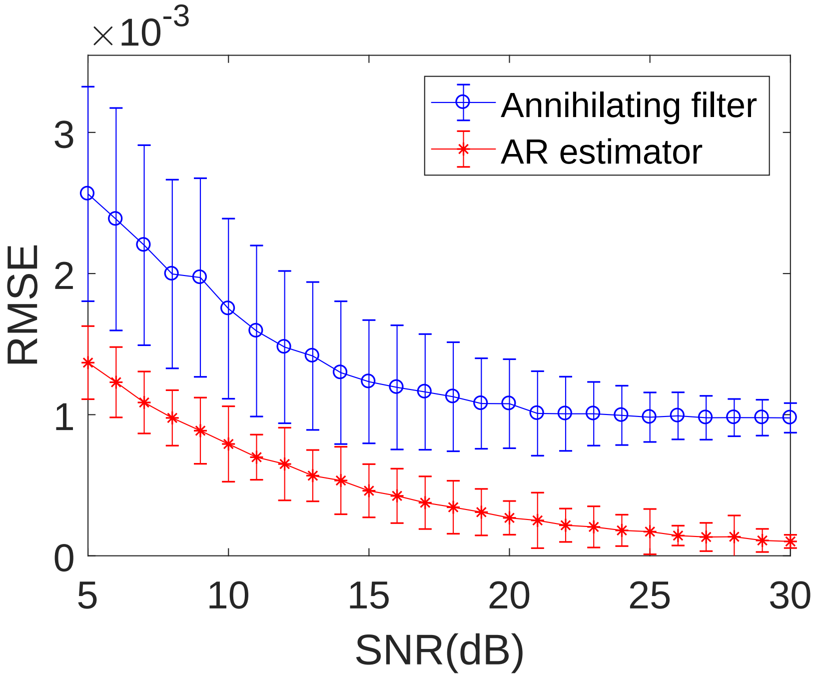

Figure 4.7: Averaged root mean square errors and standard deviations of the signals reconstructed using FRI-AR approach and annihilating filter depending on the different noise levels.

pulse is calculated by:

$$\boldsymbol{d} = \frac{\boldsymbol{c}_w}{2}\frac{\text{imag}(\log(\lambda_1))}{\Delta f} \tag{4.16}$$

Based on the physics of QAM RF signals observed in Fig. 1.11(a), the following equations are self-evident:

$$\Delta t_1 = \frac{2\boldsymbol{d}}{\boldsymbol{c}_w}, \quad \Delta t_2 = \frac{2\boldsymbol{d}}{\boldsymbol{c}} - \frac{2\boldsymbol{d}}{\boldsymbol{c}_w} \tag{4.17}$$

The formula for the SOS ($\boldsymbol{c}$) is built by means of (4.14), (4.16) and (4.17) as:

$$\boldsymbol{c} = \boldsymbol{c}_w \frac{\text{imag}(\log(\lambda_1))}{\text{imag}(\log(\lambda_1)) + \text{imag}(\log(\lambda_2))}, \tag{4.18}$$

The attenuation $\boldsymbol{\alpha}$ is acquired by dividing β_2 with $2\boldsymbol{d}$ commensurate with the round-trip path into a sample:

$$\boldsymbol{\alpha} = \frac{\beta_2}{2\boldsymbol{d}} \tag{4.19}$$

Finally, the acoustic impedance is determined with the amplitude decay (a_1) of the first reflection and prior knowledge as [Rohrbach 2018]:

$$\boldsymbol{Z} = \boldsymbol{Z}_w \frac{1 + \frac{a_1}{R_{wg}}}{1 - \frac{a_1}{R_{wg}}} \tag{4.20}$$

where R_{wg} is the known pressure reflection coefficient between water and glass.
In the following section, we provide the resulting acoustic maps yielded by $\boldsymbol{c}$ and $\boldsymbol{Z}$.

4.5 Simulation Results

Simulations were conducted with nine innovation rates chosen considering 6 dB bandwidth of the reference signal, and the results are reported in section 4.5.3 for the acoustic parameter estimation. More importantly, the outcomes lead to an instructive discussion on how the most preferable innovation rate could be selected in a sense of the sampling efficiency and the estimation accuracy.

4.5.1 Experimental data and QAM system

To evaluate the FRI-based AR approach, experimental QAM data were acquired from a chicken tendon sample using a QAM system equipped with a 250 MHz center frequency transducer. A fresh chicken tendon was fixed in formalin while loaded longitudinally then cryosectioned (16-μm thick) and affixed to a microscopy slide [Yang 2018]. The RF data cube was obtained by raster scanning the microscopy slide in two dimensions using 2-μm steps between adjacent scan lines. At each scan location, the RF signal was sampled at 2.5 GHz. The resulting RF data cube was of size 501 × 501 × 200 RF samples. The QAM system has been described in great details in previous publications (see, *e.g.*, [Mamou 2015a, Rohrbach 2015a, Rohrbach 2015b]) which were committed to identification of various elastic properties of soft tissues, *i.e.* attenuation ($\boldsymbol{\alpha}$), SOS ($\boldsymbol{c}$), acoustic impedance ($\boldsymbol{Z}$), bulk modules ($\boldsymbol{B}$) and mass density ($\boldsymbol{\rho}$). The -20 dB bandwidth of the QAM system extended to approximately 400 MHz. Therefore, in what follows, we define the Nyquist frequency of the QAM system to be 800 MHz. The experimental data were sampled using the FRI-based method with the same spatial step size but with temporal sampling frequencies ranging from 75 MHz to 250 MHz (25 MHz steps) yielding from 7 to 21 samples per RF line. These sampling frequencies correspond to a range from approximately 9.4% to 31.3% of the QAM system Nyquist frequency 800 MHz.

4.5.2 Similarity measures

Quantitative evaluations between the acoustic maps obtained with the proposed approach and their counterpart produced from fully sampled RF signals are performed using the normalized mean squared error (**NRMSE**= $\sqrt{\frac{\|\mathbf{x}-\hat{\mathbf{x}}\|^2}{\|\mathbf{x}\|^2}}$) and the peak signal to noise ratio (**PSNR(dB)**= $10\log_{10}\frac{\max(\mathbf{x},\hat{\mathbf{x}})^2}{\|\mathbf{x}-\hat{\mathbf{x}}\|^2}$), which are defined as the comparison between two images $\mathbf{x}$ and $\hat{\mathbf{x}}$.

4.5.3 Acoustic parameter maps

We herein evaluate the quality of the 2D acoustic maps, *i.e.* SOS map (2DcM) and acoustic impedance map (2DZM), reconstructed from QAM RF signals sampled following the proposed scheme against the one estimated from fully sampled RF data cubes. Fig. 4.8 (a) and (b-i) shows 2DcMs reconstructed from the conventional AR estimator (*i.e.*, applied to the data sampled at 2.5 GHz) and using the proposed FRI-based AR estimator applied at 8 different effective sampling rates. Similarly, Fig. 4.9 shows the red boxes of Fig. 4.8 to provide visual details at a finer scale. On the whole, in spite of the much lower sampling rate, the 2DcMs reconstructed using the FRI-based AR estimator shows no significant visual degradation except for the 2DcM built from 7 samples (*i.e.*, sampling at 75.0 MHz) of Fig. 4.8 (b). Additionally, Fig. 4.10 compares the single lines extracted at 0.4mm on the y-axis of each map in order to scrutinize the estimation accuracy of the acoustic parameter in the 2DcMs yielded from the innovation rates. It clearly illustrates two lines are exactly overlapped on most positions in the sampling schemes using over 125.0 MHz of Fig. 4.10 (c)-(h), whereas the result recovered from 75.0 MHz reveals the severe distortion as observed earlier. Figures 4.11, 4.12 and 4.13 present the 2DZM results in the exact same fashion as Figures 4.8, 4.9, and 4.10. Overall, the results follow the same trends as those of the 2DcMs. The above visual observations are quantitatively confirmed by standard quality metrics (*i.e.*, normalized root mean square

Number of samples	Sampling frequency (MHz)	Fraction of Nyquist rate (800 MHz) in %	SOS map		Acoustic impedance map	
			NRMSE	PSNR(dB)	NRMSE	PSNR(dB)
7	75	9.4	0.1064	17.73	0.1073	18.41
9	100	12.5	0.0771	20.68	0.0842	21.42
11	125	15.6	0.0529	24.50	0.0591	24.51
13	150	18.8	0.0498	25.00	0.0631	23.94
15	175	21.9	0.0500	25.00	0.0498	25.99
17	200	25.0	0.0498	25.07	0.0464	26.60
19	225	28.1	0.0493	25.16	0.0461	26.66
21	250	31.2	0.0509	24.87	0.0456	26.74

Table 4.2: Quantitative results computed between the 2D map from fully sampled RF data cube and those obtained from QAM RF signal sampled at low rates: 262.5 MHz (21 samples per RF signal), 237.5 MHz (19 samples per RF signal), 212.5 MHz (17 samples per RF signal), 187.5 MHz (15 samples per RF signal),162.5 MHz (13 samples per RF signal), 137.5 MHz (11 samples per RF signal), 112.5 MHz (9 samples per RF signal) and 87.5 MHz (7 samples per RF signal) .

error and peak signal to noise ratio) shown in the Table 4.2 (which were computed in the zoomed in areas, *i.e.*, red rectangle). As expected, the results obtained with 7 samples show large NRMSE and low PSNR. Small improvement exists in these metrics when 9 samples are used. Interestingly, NRMSE and PSNR results for between 11 and 21 samples are all satisfactory and nearly identical. No further improvement is obtained even when more samples are used, which will be discussed in the following section.

4.6 Discussion and conclusions

The objective of this work was to combine a low rate RF signal sampling procedure with an AR model-based parametric acoustic map reconstruction in QAM imaging. Both approaches were based on a parametric model of the QAM RF signals with a limited number of degrees of freedom, *i.e.* the amplitudes, time delays and frequency-dependent attenuation coefficients. We showed encouraging results by proving that the proposed FRI-based AR approach can reconstruct 2D acoustic maps with an accuracy comparable to the conventional QAM technology, despite using sampling frequency 18 times lower than the one (2.5 GHz) classically used within existing imaging systems and 6 times lower than the rate (800 MHz) required by the Nyquist criterion.

Taking into account a model mismatch caused by noise, artifacts or scattering in the tissue structure, the FRI-based AR estimator is able to obtain the most desirable two echoes in the manner of screening out such noise perturbations with the dedicated logic. In this sense, increasing n in (4.12) implies that we can construct more individual pulses, and two correct reflections are more likely to be separable from the noise effects. However, because this requires the increase of Fourier coefficients, *i.e.* higher innovation rate, we need to find a compromise. Except for the results acquired from the sampling rates below 6-dB bandwidth, *i.e.* 7 and 9 samples, the overall numerical assessments on the Table 4.2 reveal no noticeable improvement even though the number of samples increases. This is likely to result from the fact that, as illustrated in the Fig. 4.1(b), the coefficients away from the center frequency have less contribution to the signal information. Accordingly, the analysis of the power distribution of a reference signal could offer a critical insight to determine the most relevant innovation rate of an QAM RF signal featured by five parameters. Likewise, the estimation failure in less innovation rates than 11 samples could be explained in this perspective. To conclude, the simulation results legitimize that the innovation rate (125 MHz) of 11 samples, equivalent to 6 dB bandwidth showing the estimation performance comparable to its counterparts (*i.e.* over 125 MHz), can be considered as the optimal operating in this experiment, *i.e.* the compromise between the sampling cost and the image quality as stated above.

Strang-Fix condition [Khalidov 2005, Vonesch 2007] defines the property of a sampling kernel able to perfectly represent the moments of an FRI signal in a subspace spanned with a maximum order corresponding to the innovation rate. In the simulations, we used SoS sampling kernel in [Tur 2011] since it respects this property. However, other sampling kernels could also be considered such as B-splines that reproduce polynomials other than exponentials [Unser 1999, Dragotti 2007].

The FRI-based AR approach to QAM presented in this paper has tremendous implications for QAM systems. For instance, it would allow the use of much slower A/D cards than those currently used. This would drastically reduce costs. Furthermore, slower A/D cards are much easier to manufacture and therefore can be made with higher bit counts (*e.g.*, 16 bits sampling at 250 MHz is much easier to manufacture than 12 bits at 2.5 GHz) yielding increased data quality and lower sensitivity to noise. Currently, most QAM systems do not fully operate in real-time and require a few seconds to process the data and form images. The FRI-based AR approach completely short circuits the process of forming images by not only providing much less data overall, but, more importantly, by directly providing normalized Fourier coefficients used in the AR algorithm thus saving precious computation time.

Based on this achievement, we plan to propose an approach able to further reduce the data acquisition time and the size of the data cube from spatio-temporally under-sampled measurements by combining both the compressed sensing framework [Emmanuel 2004, Donoho 2006b] and the finite rate of innovation signal theory. The integration of two methods is straightforward thanks to the previous study [Kim 2018a]; the compressed scanning scheme in spatial domain followed by the FRI sampling in temporal domain will lead to extremely squashed data cube compared to the conventional QAM technique.

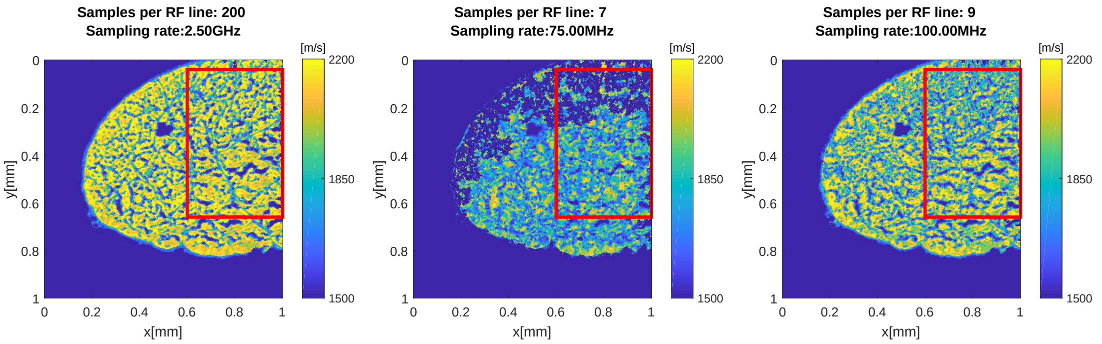
Samples per RF line: 200 Sampling rate:2.50GHz

Samples per RF line: 7 Sampling rate:75.00MHz

Samples per RF line: 9 Sampling rate:100.00MHz

(a) (b) NRMSE(0.1064),PSNR(17.73dB) (c) NRMSE(0.0771),PSNR(20.68dB)

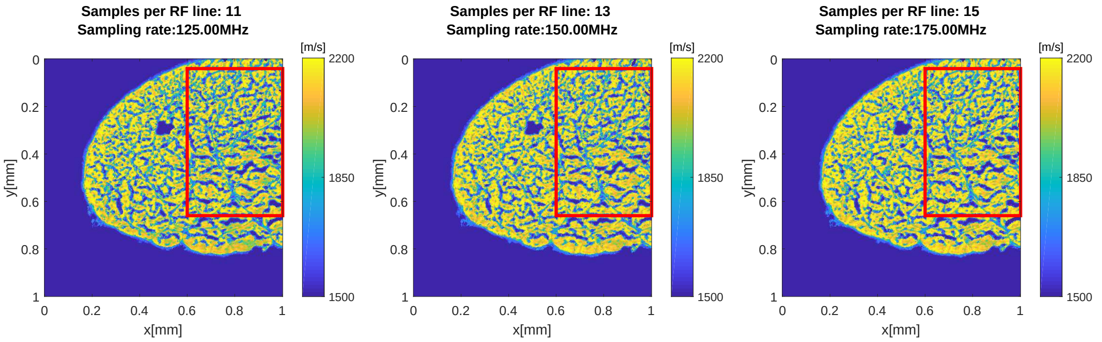
Samples per RF line: 11 Sampling rate:125.00MHz

Samples per RF line: 13 Sampling rate:150.00MHz

Samples per RF line: 15 Sampling rate:175.00MHz

(d) NRMSE(0.0529),PSNR(24.50dB) (e) NRMSE(0.0498),PSNR(25.00dB) (f) NRMSE(0.0500),PSNR(25.00dB)

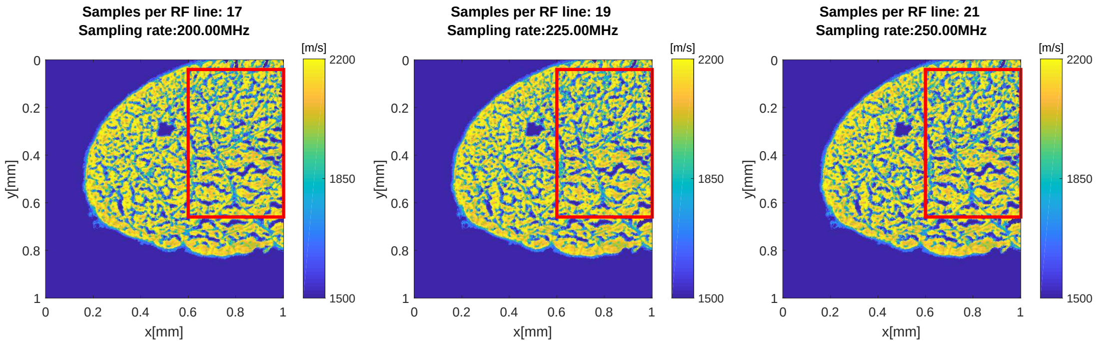
Samples per RF line: 17 Sampling rate:200.00MHz

Samples per RF line: 19 Sampling rate:225.00MHz

Samples per RF line: 21 Sampling rate:250.00MHz

(g) NRMSE(0.0498),PSNR(25.07dB) (h) NRMSE(0.0493),PSNR(25.16dB) (i) NRMSE(0.0509),PSNR(24.87dB)

Figure 4.8: (a) and (b-i) are SOS maps estimated from fully-sampled RF data cube (200 samples per RF signal), and from samples acquired following the proposed approach corresponding to respectively 7, 9, 11, 13, 15, 17, 19 and 21 samples per RF signal. Quantitative accuracy measurements computed from the red box in these SOS maps are given in Table 4.2.

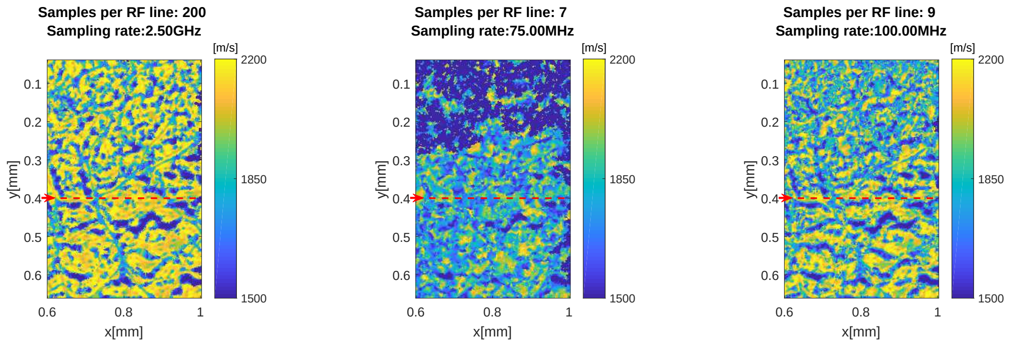

(a)

(b) NRMSE (0.1064), PSNR (17.73dB)

(c) NRMSE (0.0771), PSNR (20.68dB)

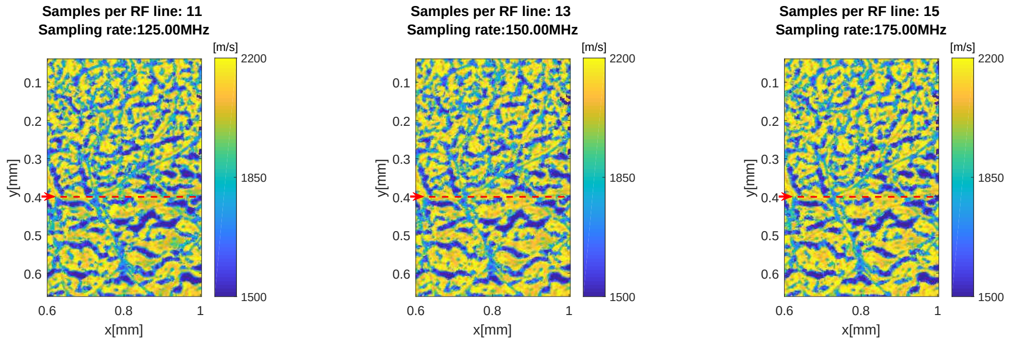

(d) NRMSE (0.0529), PSNR (24.50dB)

(e) NRMSE (0.0498), PSNR (25.00dB)

(f) NRMSE (0.0500), PSNR (25.00dB)

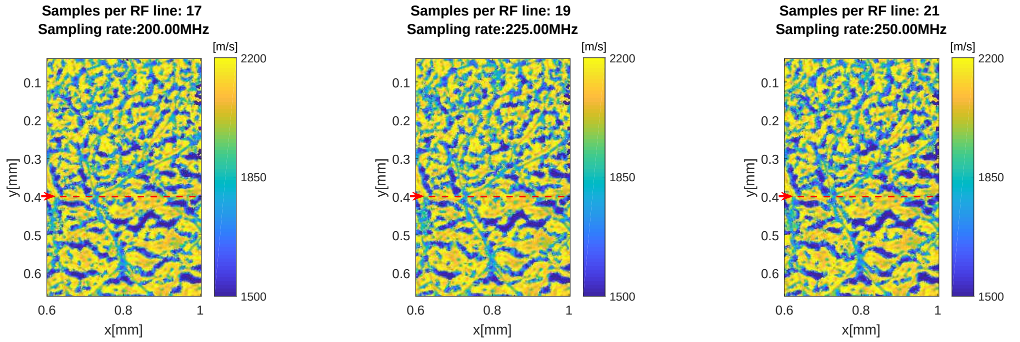

(g) NRMSE (0.0498), PSNR (25.07dB)

(h) NRMSE (0.0493), PSNR (25.16dB)

(i) NRMSE (0.0509), PSNR (24.87dB)

Figure 4.9: Magnified maps of the red boxes in Fig. 4.8. (a) is the SOS map created from fully-sampled RF data cube (200 samples per RF signal), (b-i) are the SOS maps estimated following the proposed approach corresponding to respectively 7, 9, 11, 13, 15, 17, 19 and 21 samples per RF signal. The red dotted line indicates the cross sectioned location of profiles in Fig. 4.10.

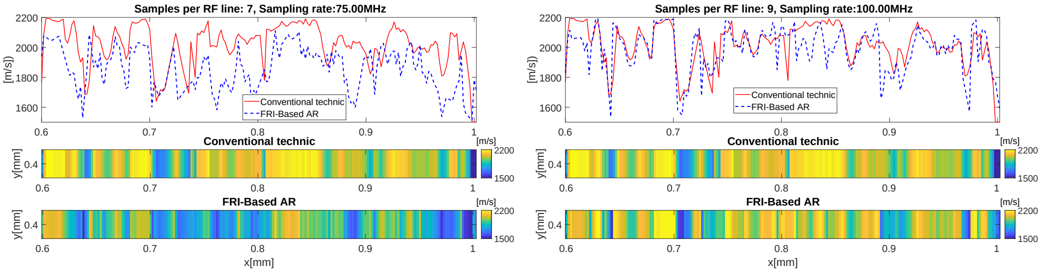

(a) NRMSE (0.1140), PSNR (18.89)

(b) NRMSE (0.0520), PSNR (25.61)

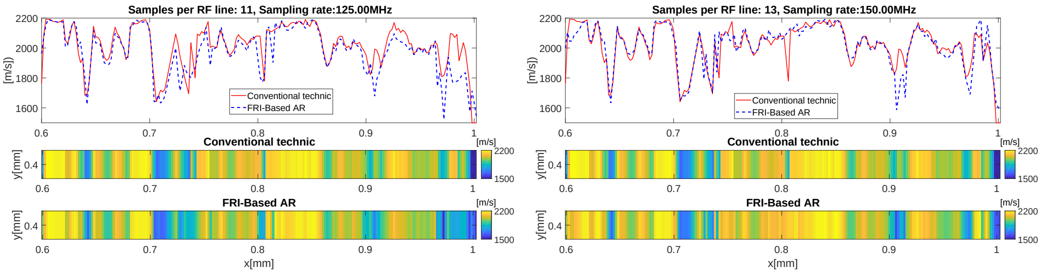

(c) NRMSE (0.0300), PSNR (30.33)

(d) NRMSE (0.0274), PSNR (31.24)

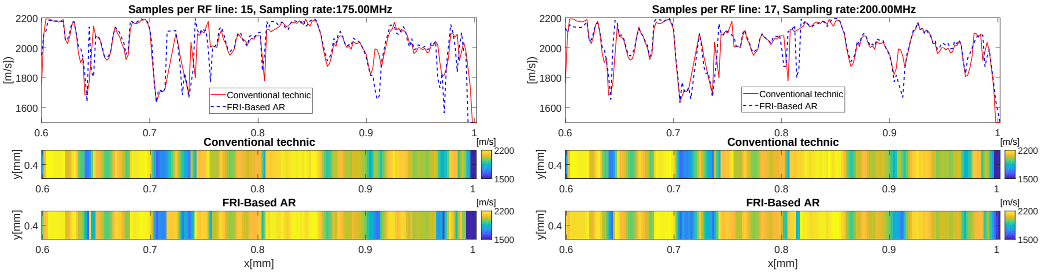

(e) NRMSE (0.0354), PSNR (29.10)

(f) NRMSE (0.0284), PSNR (31.02)

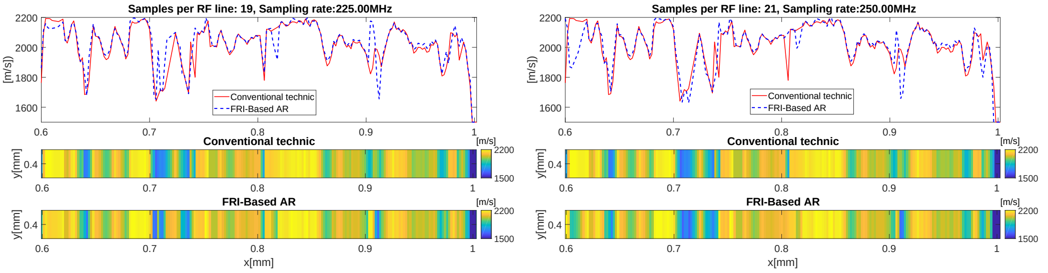

(g) NRMSE (0.0243), PSNR (32.45)

(h) NRMSE (0.0267), PSNR (31.54)

Figure 4.10: Horizontal cross sections and single lines of 2DcM at 0.4mm of y-axis in Fig. 4.9. The red continuous lines are a cross section from fully sampled map, *i.e.* Fig. 4.9(a) which is used as the criterion for comparison. The blue dotted lines of (a-h) represent the cross sections of Fig. 4.9(b-i) respectively.

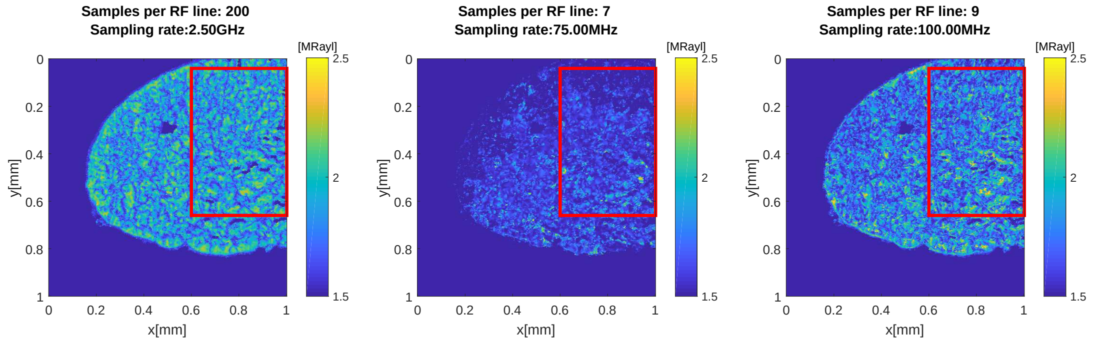

(a) (b) NRMSE (0.1073), PSNR (18.41dB) (c) NRMSE (0.0842), PSNR (21.42dB)

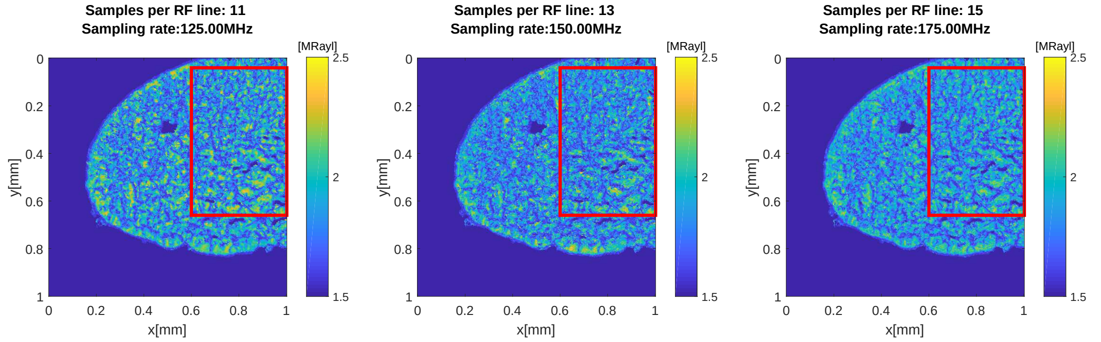

(d) NRMSE (0.0591), PSNR (24.51dB) (e) NRMSE (0.0631), PSNR (23.94dB) (f) NRMSE (0.0498), PSNR (25.99dB)

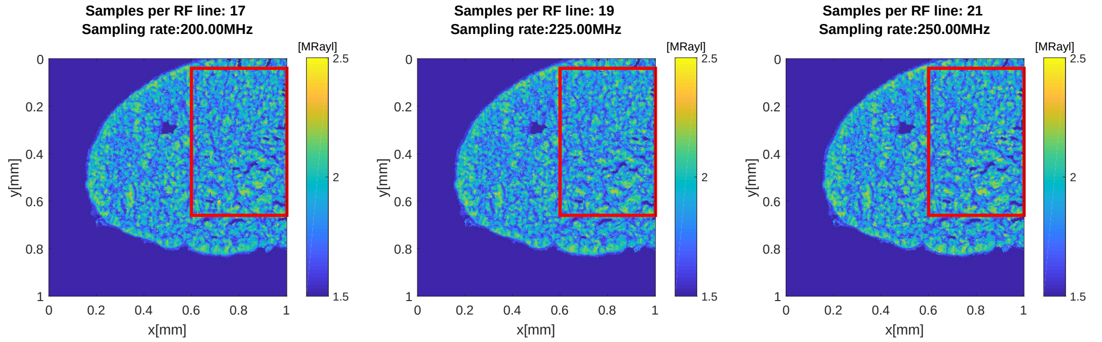

(g) NRMSE (0.0464), PSNR (26.60dB) (h) NRMSE (0.0461), PSNR (26.66dB) (i) NRMSE (0.0456), PSNR (26.74dB)

Figure 4.11: (a) and (b-i) are acoustic impedance maps estimated from fully-sampled RF data cube (200 samples per RF signal), and from RF signals sampled following the proposed approach corresponding to respectively 7, 9, 11, 13, 15, 17, 19 and 21 samples per RF signal. Quantitative accuracy measurements computed from the red box in these SOS maps are given in Table 4.2.

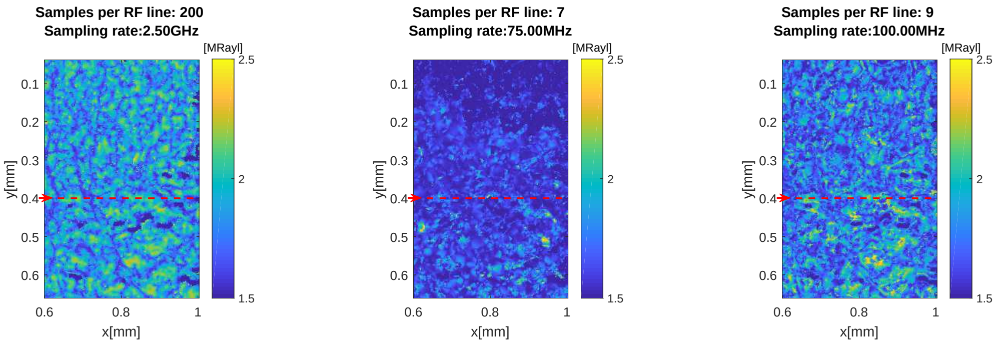

(a) (b) NRMSE (0.1073), PSNR (18.41dB) (c) NRMSE (0.0842), PSNR (21.42dB)

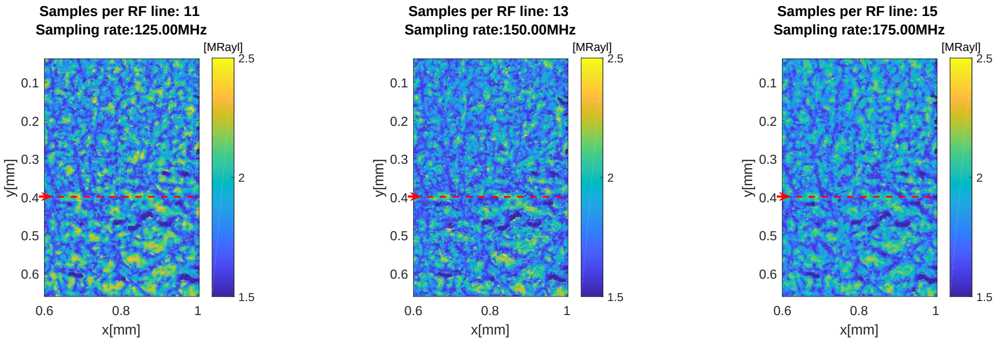

(d) NRMSE (0.0591), PSNR (24.51dB) (e) NRMSE (0.0631), PSNR (23.94dB) (f) NRMSE (0.0498), PSNR (25.99dB)

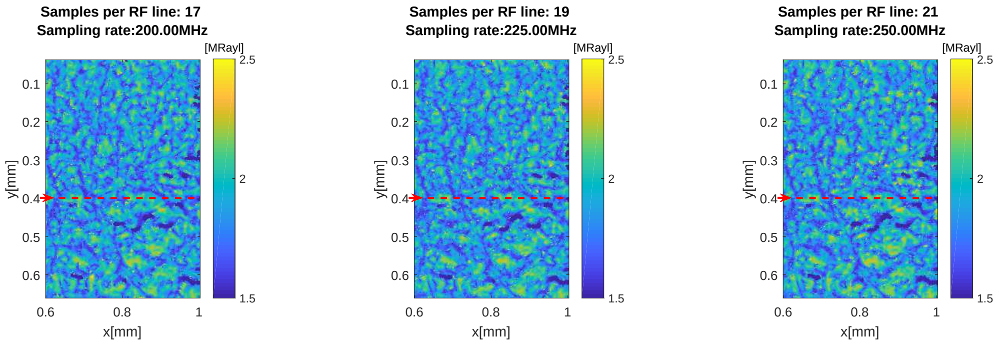

(g) NRMSE (0.0464), PSNR (26.60dB) (h) NRMSE (0.0461), PSNR (26.66dB) (i) NRMSE (0.0456), PSNR (26.74dB)

Figure 4.12: Magnified maps of the red boxes in Fig. 4.8. (a) is the acoustic impedance map created from fully-sampled RF data cube (200 samples per RF signal), (b-i) are the acoustic impedance maps estimated following the proposed approach corresponding to respectively 7, 9, 11, 13, 15, 17, 19 and 21 samples per RF signal. The red dotted line indicates the cross sectioned location of profiles in Fig. 4.13.

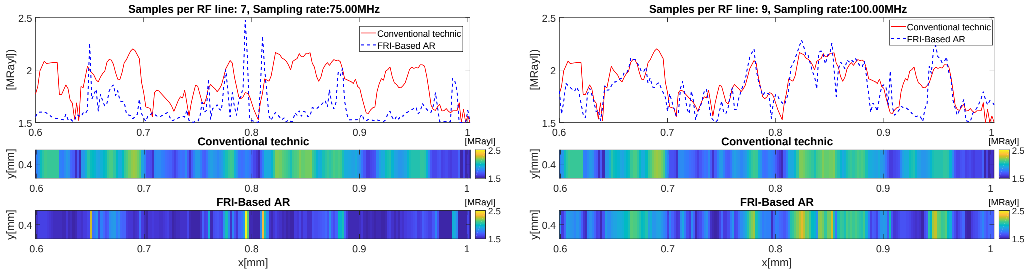

(a) NRMSE (0.1460), PSNR (16.69dB)
(b) NRMSE (0.1000), PSNR (19.97dB)

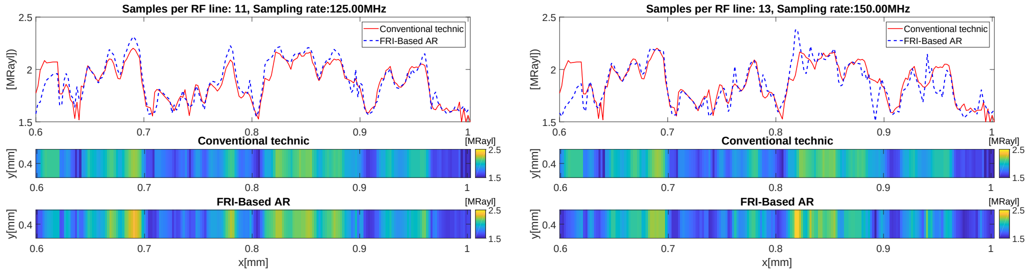

(c) NRMSE (0.0540), PSNR (25.31dB)
(d) NRMSE (0.0590), PSNR (24.54dB)

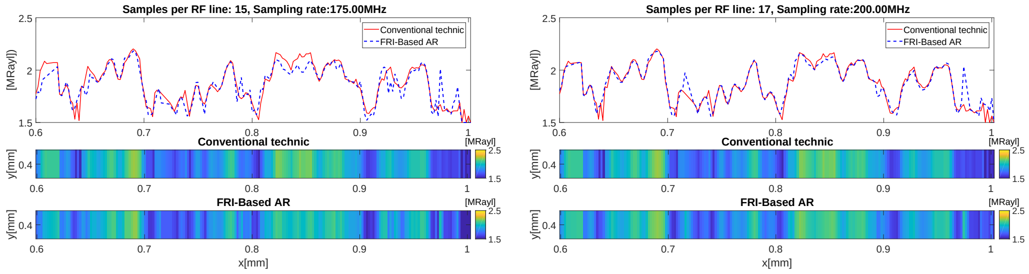

(e) NRMSE (0.0430), PSNR (27.31dB)
(f) NRMSE (0.0390), PSNR (28.12dB)

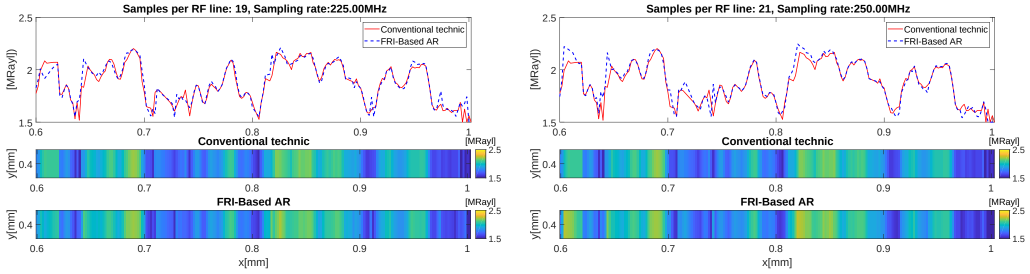

(g) NRMSE (0.0400), PSNR (27.96dB)
(h) NRMSE (0.0350), PSNR (29.20dB)

Figure 4.13: Horizontal cross sections and single lines of 2DZM at 0.4mm of y-axis in Fig. 4.12. The red continuous lines are a cross section from fully sampled map, *i.e.* Fig. 4.12(a) which is used as the criterion for comparison. The blue dotted lines of (a-h) represent the cross sections of Fig. 4.12(b-i) respectively.

Chapter 5

Compressed QAM in spatio-temporal domain

Part of the work in this chapter has been published in [Kim 2019].

Contents

5.1 Introduction

In QAM technology, the scanning for a data acquisition is a quite time consuming process relying on a sample size and the center frequency of transducer. In order to prevent the changes in mechanical properties of the sensitive thin sectioned tissue during scanning, a strategy for reducing the scanning time is of urgent necessity.

In this regard, the previous chapters were devoted to demonstrating: i) spatially under sampled measurements, following a spiral pattern combined with image reconstruction based on approximate message passing (AMP), allow decreasing the number of acquired RF signals by 40% without degrading the QAM image quality [Kim 2018a], ii) since QAM RF signals at a given location follow a parametric form with a limited number of degrees of freedom, each RF signal can be sampled (and adequately processed) at a much lower rate (162.5 MHz) than the Nyquist rate (800 MHz for our QAM system) [Kim 2018b].

The main objective of this chapter is to present a single solution by combining the two undersampling schemes to lead to far more parsimonious data acquisition, and to demonstrate that the combined approach is able to significantly save QAM data acquisition time and QAM data size at no detriment to image quality.

The remainder of this chapter is structured as follows. Section 5.2 describes the spatio-temporal sparse encoding of QAM data, sequentially operating two undersampling techniques individually adopted in spatial and temporal domain. Subsequently section 5.3 shows the process decoding the cubic dataset compressed in three dimension in the preceding section. Section 5.4 evaluates the simulation results through the comparison with the 2D map yielded by the traditional manner, and conclusions are presented in Section 5.5.

5.2 Spatio-temporal sparse encoding

Hereafter, the two frameworks (*i.e.*, CS using AMP and FRI) are combined to achieve spatio-temporal undersampling of QAM data. Fig. 5.1 illustrates the successive sampling process performed by CS and FRI frameworks. Firstly, the spiral pattern scanning is performed pointwise; only RF signals from these scan locations are retained, and are sampled using the FRI framework. As a result, the total amount of collected data was significantly reduced as depicted in the right cartoon in Fig. 5.1.

Compressed scanning in spatial domain

CS measurement in space is implemented with a spiral scanning pattern developed in [Kim 2018a] as addressed in chapter 3. The development was inspired by [Wan 2008, Quinsac 2010] which proposed alternative sensing manners as the breakthrough to overcome various practical issues caused by random sensing matrices recommended in canonical CS literature [Donoho 2006b]. As discussed in the previous chapter, the spiral sensing manner proved to simultaneously achieve the requirement of CS and the compatibility with an QAM motor stage. In particular, when it comes to the best results of the spiral

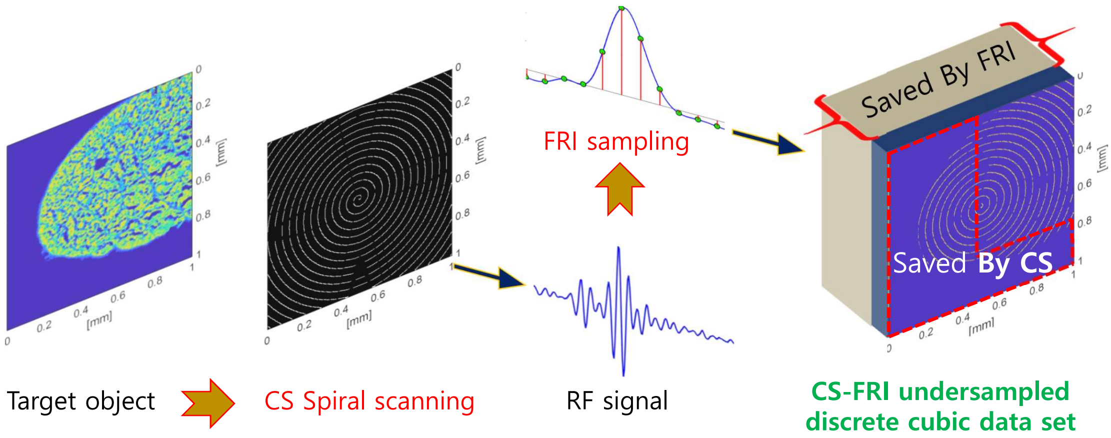

Figure 5.1: The block diagram describes the undersampling process based on the spiral pattern and FRI sampling in spatial and temporal domain respectively. The right cartoon clearly demonstrates the space saved by the proposed sampling scheme.

pattern compared with its counterparts, we tentatively concluded, in chapter 3, that it may result from lower coherence with wavelet basis than other considered sensing patterns.
CS measurement is given by:

$$\mathbf{y} = \mathbf{\Phi}\underbrace{\mathbf{W}^{-1}\boldsymbol{\theta}_{\mathbf{x}}}_{\mathbf{x}} + \mathbf{n} \tag{5.1}$$

where $\mathbf{\Phi}$ represents the sensing matrix, and actually the sparse scanning is performed by Bernoulli trial process which collects values corresponding to the index of elements to be scanned after vectorizing the spiral patterned matrix.

Innovation rate sampling in time domain

As a review of FRI sampling in chapter 4, recall that QAM RF signals are made up of two primary reflections due to the water-tissue and tissue-glass interfaces, which can be modeled by the sum of two time-delayed, amplitude-decayed and frequency-dependent attenuated versions of a reference RF pulse $h_0(t)$ as follow:

$$h(t) = a_1 h_0(t - t_1) + a_2 h_0^*(t - t_2) \tag{5.2}$$

where the symbol $*$ stands for frequency-dependent attenuation. Since the information of the pulse shape $h_0(t)$ is given as the echo from a planar reflector at the focal depth, and can be easily obtained experimentally from the data collected at only glass plate locations, (5.2) is regarded as an FRI signal fully defined with the parametric expression. The sampling procedure is identical to what we addressed in the previous chapter, but note that the RF signals are recorded following the spatial undersampling scheme proposed in chapter 3. As a result, the volume of the cubic dataset is dramatically shrunk compared to the conventional data acquisition manner as highlighted in the rightmost cartoon of Fig. 5.1.

5.3 Reconstruction of 2D acoustic maps

The reconstruction of 2D map begins by using the auto-regressive (AR) parameter estimation [Rohrbach 2018] from the cubic dataset illustrated in the bottom left of Fig. 5.2, the result of which is equivalent to CS measurement in spatial domain as depicted in Fig. 5.3(b). Therefore, the CS measurement of an QAM 2D map is reconstructed by the AMP algorithm as what we did in chapter 3. The overview of the recovery process in the spatio-temporal approach is described in Fig 5.2

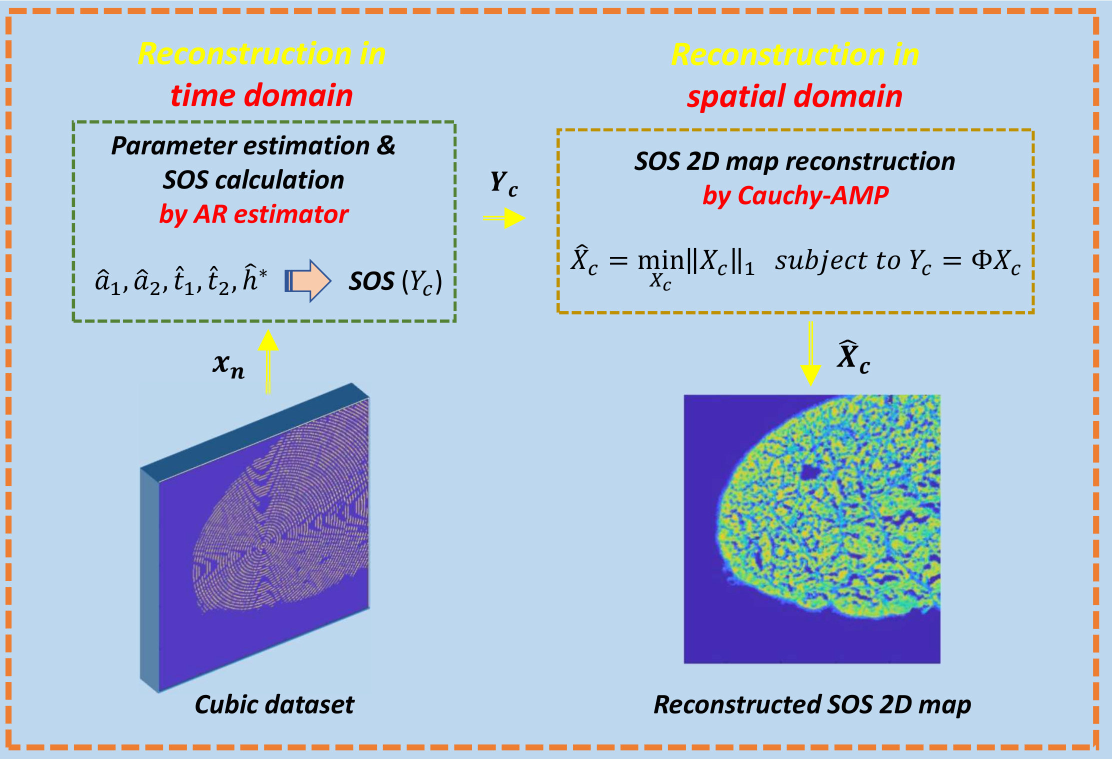

Figure 5.2: The block diagram describes the recovery process which is made up of two process, *i.e.*, the parameter estimation in time domain and image reconstruction in spatial domain.

Acoustic parameter estimation
The recovery scheme in time domain is exactly same as what we addressed in the sections associated with the model parameter estimation and the reconstruction of acoustic parameter 2D maps in chapter 4. However, the recovered SOS map is Y_c as described in Fig. 5.2, which is equivalent to the result of CS measurement with the spiral pattern scanning. Thus, the last step of this approach is completed by CS reconstruction framework developed in chapter 3

Reconstruction in acoustic 2D map
Since the RF signals collected in spatial domain covered only the spiral pattern, we accomplish the recovery process using AMP algorithm. The corresponding problem setting is as follows:

$$\hat{X}_c = \min_{X_c} \|X_c\|_1, \quad \text{subjec to} \quad Y_c = \Phi X_c \tag{5.3}$$

5.4 Simulation results

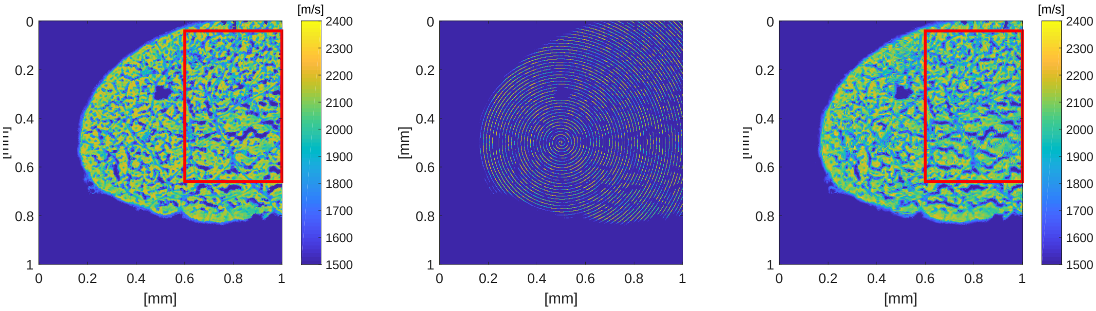

(a) (b) (c)

Figure 5.3: The figure shows the recovery process of the SOS 2D map of a chicken tendon tissue. (a) is the original 2D map yielded by the conventional method, (b) is an intermediate result produced by estimating the SOS of the RF signals reflected from the only positions scanned by the spiral pattern, and finally (c) is the complete FRI-CS recovery result.

A 2D SOS map of a chicken tendon tissue in Fig. 5.3 was reconstructed using the proposed approach described in Fig. 5.2 from the compressed spiral cubic data set (40% less spatial data than classical raster scan and sampling rate of only 6.5% of the currently used rate as shown in the Table 5.1). The spiral scanning pattern of Fig. 5.1 would allow to reduce the scan time by far more than 40% because of the continuous motion of the motors which is made possible through the smoothness of the spiral. Furthermore, significantly compressed data volume, *i.e.*, 2.6% compared to conventional method, could

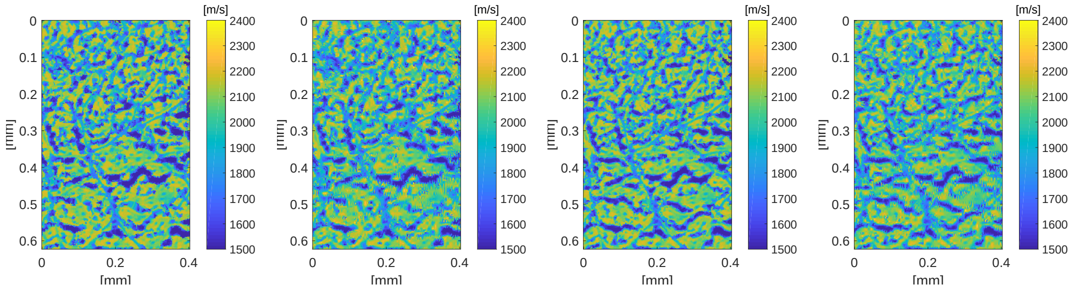

(a) (b) (c) (d)

Figure 5.4: The figure compares the SOS 2D map formed by the conventional approach (a) with the images (b-d) recovered from different methods, *i.e.*, wavelet based Cauchy-AMP in chapter 3, FRI-AR estimator in chapter 4, and spatio-temporal approach introduced in chapter 5 respectively.

contribute to saving the required data storage space. In spite of the enormous decrease of data acquisitions, in the resulting images in Fig. 5.4 (d), no critical image degradation is perceived. The metrics in Table 5.2 support the visual evaluation.

Methods	Compressed Ratio		
	Spatial	Temporal	Total volume (Spatial × Temporal)
CS	40%	-	40%
FRI	-	6.5%	6.5%
FRI-CS	40%	6.5%	2.6%

Table 5.1: Compressed ratio according to different methods. The ratios of data reduction on this table correspond to 1004 scanning points on 40% of the spatial domain, and 13 samples on 6.5%the temporal axis.

	PSNR(dB)	NRMSE	SSIM
CS	26.31	0.0483	0.7166
FRI	24.19	0.0617	0.6741
FRI-CS	23.38	0.0678	0.5511

Table 5.2: Resulting metrics according to different methods.

5.5 Conclusions

In this chapter, two approaches of CS and FRI sampling were combined, resulting into both shorter acquisition times and significantly reduced amount of acquired data, compared to not only the classical QAM sampling scheme but also the individual undersampling techniques introduced in chapter 3-4. To validate the feasibility of proposed approach (*i.e.*, spiral pattern scanning in spatial domain and innovation rate sampling in time domain) and to confirm the preliminary results obtained in post-processing, a hardware implementation on our QAM scanner will be carried out as a future work.

Chapter 6

Conclusions and Perspectives

6.1 Conclusions

Quantitative acoustic microscopy (QAM) provides a unique contrast of a resulting image by quantitatively characterizing the acoustic properties of biological soft tissue, compared to other contemporary microscopic imaging modalities. The most beneficial feature of the ultrasound-based method is to allow medical doctors to diagnose a disease by examining the abnormality in the mechanical property of tissues. For instance, malignant lesions in the breast or the stage of liver fibrosis typically accompanies the change of elasticity in tissue, which can be detected by the measurement of acoustic parameters. However, complying with the conventional data acquisition procedure, the elasticity imaging method leads to a prolonged exposure of the sample to be imaged, and consequently leads the change of its mechanical properties to be possibly. This can yield accuracy and reliability issues in parameter estimation.

From the perspective, this PhD thesis aimed to propose novel approaches able to realize an efficient measurement and faithful parameter estimation to tackle current problems. To achieve this objective, the first step was to use the characteristics of the data information recorded by the ultrasonic microscope. More specifically, the contributions of this work consisted in two different aspects: spatial and time domain approaches.

Our first work introduced compressed sensing framework based on the sparse property of parametric 2D maps. The challenge in the first work was to devise a practically implementable scanning pattern while leading to the incoherence measurement on the wavelet domain as a sparsifying transform. Three dedicated patterns, compatible with the restricted mechanical operation of QAM, were tested and it was concluded from the experimental results that the spiral scanning approach showed the best recovery quality. For subsequent image reconstruction, we designed and implemented an innovative technique based on the approximate message passing (AMP) method. Specifically, Cauchy maximum a posteriori (MAP) image denoising algorithm was thus employed to support the non-Gaussianity of QAM wavelet coefficients which have heavy-tails. The proposed methods were tested retrospectively on experimental data acquired with a 250-MHz or 500-MHz QAM system. The experimental data were obtained from a human lymph node sample (250 MHz) and human cornea (500 MHz). The spiral sensing matrix reduced the number of spatial samples by a factor of 2 and led to an excellent recovery quality when reconstructing QAM SOS images of a human lymph node. Moreover, our proposed recovery algorithm showed enhanced performance compared to alternative AMP algorithms associated with different shrinkage functions as well as standard CS reconstruction, based on ℓ_1 norm or ℓ_p norm optimization.

Overall, these results demonstrate that the CS approach could significantly improve scanning time, while reducing costs of future QAM systems. Nevertheless, it still seems to be necessary to clarify the incoherence of the introduced measurement scheme with sparsifying transforms so that future researches could facilitate CS application to QAM.

The second contribution of this thesis was focused on the parsimonious sampling of RF signal in time domain, which was accomplished using the proposed FRI-AR approach. The core idea behind the development was inspired by bridging the two methods of [Tur 2011] and [Rohrbach 2018]. Generally, the formulation of QAM RF signals is founded on the hypothesis that the thin section of tissue is homogeneously distributed in the direction of travel path of wave, and thus it is fully characterized by physical phenomena occurring on the only two main interfaces. Accordingly, the introduction of the FRI sampling scheme could lead to dramatic reduction in data acquisition of the QAM RF signal perfectly represented with a few parameters. The sum of sinc kernel performed the low rate sampling, which satisfies Strang-Fix condition and guarantee the exact reconstruction of Fourier coefficients of input. On the other hand, the discrepancy, between the ideal setting of the homogeneity in the cross section of sample and the reality, gives rise to noise or artefacts in our signal model. AR estimator showed the superiority to collect the two most desired echo pules among multiple reflections reconstructed. The combination of FRI and AR model for sampling and parametric map recovery allows decreasing the required number of samples per RF signal up to a factor of 18 compared to a conventional approach, with a minimal accuracy loss in the quantitative acoustic maps. This was proven by visual evaluations and numerical results for the reconstructed SOS map and acoustic impedance map.

The final contribution of this work was to combine two data acquisition schemes into a spatio-temporal single solution, and to highlight the benefit of our proposed approaches. The combination process was somehow straightforward, yet the results yielded a new data volume size hugely saved up to even 2.6% of the data originated by classical sampling techniques without critical deterioration of the 2D maps.

6.2 Perspectives

Incoherence of scanning pattern

Indeed, CS has been constructed on the premise of sensing matrices satisfying mathematical completeness such as RIP and incoherence to ensure perfect recovery of sparse signals. Nevertheless, since this work prioritized the aspect of practical implementation of sensing strategy, the proposed sensing patterns unavoidably followed deterministic sensing trajectories rather than CS sensing modalities design based on a randomness conditions stated above [Candès 2008]. Fortunately, our suggested scanning scheme seems to somehow keep the necessary requirements when considering the favorable outcomes. However, in order to pave the way for making our approach more robust to any problem setting or further improving our current achievement, it would be worth paying attention to the study on the deterministic sensing matrices [Naidu 2016] where promising results are presented. Aside from this, studies regarding structured random matrices have been carried out with the purpose of tackling various practical issues [Do 2011], but they were mainly developed to pursue fast and efficient implementation rather than overcoming the limitation of mechanical design like our case. Nonetheless, the studies also would deserve to be considered as a reference for our future work, when taking into account the universality with most sparsifying basis that the sensing strategy shows.

Denoiser in AMP

The most attractive merit of AMP consists in a capability to enhance its recovery performance by embedding more robust denoiser function in the iterative algorithm. In particular, we confirmed that the statistical model of signal and the behavior of the shrinkage function should be simultaneously considered to lead to the best result, including the fast convergence. In this regard, we chose the Cauchy denoiser to reconstruct heavy tailed distribution typically characterizing wavelet coefficients, instead of soft threshold devised based on the assumption of Gaussianity. Therefore, it would be still possible to produce better recovery quality for compressive imaging problems as far as a better denoiser function is used [Tan 2015]. Furthermore, Denoising-based AMP (D-AMP) [Metzler 2016] provides a quintessential solution by effectively employing generic denoiser in a CS reconstruction algorithm. Thus, a wide class of denoisers integrated within its iterations performs denoising. The key tuning scheme for each iteration is implemented with respect to the Onsager reaction term to make it appropriate use for the signal model.

The introduction of this approach in our problem could be a challenging project, yet would be expected to obtain fruitful results.

Estimation of model parameters

The parameter estimation of RF signal, in the proposed approach, was done by autoregressive model, the results of which were compared with those of annihilating filter technique as a competitive method, demonstrating its superiority. In fact, the performance was satisfactory especially due the reduced number of samples. However, the

applied undersampling rate was beyond the number of parameters fully characterizing the QAM RF signal, whereas it basically is assumed to be six, *i.e.*, $\{a_l, t_l, \beta_l\}_{l=1}^{2}$.
We had a closed form expression of the signal model in frequency domain, and confirmed that FRI sampling can faithfully retrieve the corresponding Fourier coefficients to samples in time domain. From this aspect, it would be worthy attempting to find other alternative to possibly enable an exact reconstruction from the innovation rate sampling.
The parametric model in frequency domain is represented as a decaying oscillation of the sum of two complex exponentials caused by the five unknown parameters, where a model mismatching would be interpreted as a spectrum perturbed by noise. Thus our aim is likely to estimating an original spectrum by denoising with an algorithm to be designed. Therefore, We suggest an iterative method based on the minimization of the residual between observation and estimation. The key idea to implement this process could be supported by literature related to optimization problem [Nocedal 2006].

Appendix

Appendix A

Auto regressive (AR) estimator

In this appendix, we detail the remaining steps after (4.13), for estimating the model parameters of QAM RF signals as proposed in [Rohrbach 2018].
The AR model coefficients $\mathbf{s}$ are solved by the following least-square approach:

$$\mathbf{s} = -(\mathbf{R}^H\mathbf{R})^{-1}\mathbf{R}^H\mathbf{n}, \tag{A.1}$$

where the superscript $(\,\cdot\,)^H$ represents the conjugate transpose of $(\,\cdot\,)$. Then, in order to determine λ_l, (4.11) is linked to (4.13) through the following relationship:

$$N_k = -\sum_{i=1}^{n} s_i \underbrace{\sum_{l=1}^{n} a_l \lambda_l^{k-i}}_{N_{k-i}} \tag{A.2}$$

$$= -\sum_{l=1}^{n} a_l \lambda_l^{k} \sum_{i=1}^{n} s_i \lambda_l^{-i} \tag{A.3}$$

Assuming that the second summation of (A.3) is equivalent to polynomials of n degree having zeros at $(1/\lambda_l)$, which can be recast as follows:

$$\sum_{l=1}^{n} a_l \lambda_l^{k} \mathrm{P}\left(\frac{1}{\lambda_l}\right) = 0 \tag{A.4}$$

Therefore, λ_l can be obtained by calculating the roots of the coefficients $\mathbf{s}$. For the estimation of the remaining unknown parameters, (4.11) is turned into the following matrix-vector form:

$$\mathbf{n}_2 = \mathbf{\Lambda}\mathbf{a} \tag{A.5}$$

where $\mathbf{n}_2$, $\mathbf{\Lambda}$ and $\mathbf{a}$ represent a column vector of a consecutive sequence selected from N_k, a matrix formed by λ_l^k and a column vector of the unknown parameter a_l. The size of the matrix-vector formation above is determined by the construction of AR model. Subsequently, the amplitudes a_l are obtained as a solution to (A.6) established from (A.5) using a least-square approach :

$$\mathbf{a} = (\mathbf{\Lambda}^H\mathbf{\Lambda})^{-1}(\mathbf{\Lambda}^H\mathbf{n}_2) \tag{A.6}$$

List of publications

International Journal Papers

[J1] Jong-Hoon Kim, Jonathan Mamou, Denis Kouamé, Alin Achim and, Adrian Basarab. *Autoregressive model-based reconstruction of quantitative acoustic maps from RF signals sampled at innovation rate.* IEEE Trans. on Computational Imaging, 2019. (submitted)

[J2] Jong-Hoon Kim, Jonathan Mamou, Paul R Hill, Nishan Canagarajah, Denis Kouamé, Adrian Basarab and Alin Achim. *Approximate Message Passing Reconstruction of Quantitative Acoustic Microscopy Images.* IEEE Trans. UFFC, 2018.

International Conference Papers

[C1] Jong-Hoon Kim, Jonathan Mamou, Denis Kouamé, Alin Achim and Adrian Basarab. *Spatio-temporal compressed quantitative acoustic microscopy.* IEEE Int. Ultrasonics Symposium (IUS), Glasgow, UK, October, 2019.

[C2] Jong-Hoon Kim, Jonathan Mamou, Denis Kouamé, Alin Achim and Adrian Basarab. *Reconstruction of quantitative acoustic microscopy images from RF signals sampled at innovation rate.* IEEE Int. Ultrasonics Symposium (IUS), Kobe, Japan, 2018.

[C3] Jong-Hoon Kim, Paul R Hill, Nishan Canagarajah, Daniel Rohrbach, Denis Kouamé, Jonathan Mamou, Alin Achim and Adrian Basarab. *Compressed quantitative acoustic microscopy.* IEEE Int. Ultrasonics Symposium (IUS), Washington, D.C., USA, 2017.

[C4] Jong-Hoon Kim, Adrian Basarab, Paul R Hill, David R Bull, Denis Kouamé and Alin Achim. *Ultrasound image reconstruction from compressed measurements using approximate message passing.* 24th IEEE EUSIPCO, Budapest, Hungary, 2016.

[C5] Paul R Hill, Jong-Hoon Kim, Adrian Basarab, Denis Kouamé, David R Bull and Alin Achim. *Compressive imaging using approximate message passing and a Cauchy prior in the wavelet domain.* IEEE Int. Conference on Image Processing (ICIP), Phoenix, USA, 2016.

Bibliography

[Achim 2001] Alin Achim, Anastasios Bezerianos and Panagiotis Tsakalides. *Novel Bayesian multiscale method for speckle removal in medical ultrasound images.* IEEE transactions on medical imaging, vol. 20, no. 8, pages 772–783, 2001.

[Achim 2004] Alin Achim and Ercan E Kuruoglu. *Image denoising using bivariate α-stable distributions in the complex wavelet domain.* IEEE Signal Processing Letters, vol. 12, no. 1, pages 17–20, 2004.

[Achim 2010] Alin Achim, Benjamin Buxton, George Tzagkarakis and Panagiotis Tsakalides. *Compressive sensing for ultrasound RF echoes using a-stable distributions.* In Engineering in Medicine and Biology Society (EMBC), 2010 Annual International Conference of the IEEE, pages 4304–4307. IEEE, 2010.

[Achim 2015] Alin Achim, Adrian Basarab, George Tzagkarakis, Panagiotis Tsakalides and Denis Kouamé. *Reconstruction of ultrasound RF echoes modeled as stable random variables.* IEEE Transactions on Computational Imaging, vol. 1, no. 2, pages 86–95, 2015.

[Alberts 2007] Bruce Alberts, Alexander Johnson, Julian Lewis, Martin Raff, Keith Roberts and Peter Walter. *Molecular biology of the cell: Reference edition.* 2007.

[Baraniuk 2008] Richard Baraniuk, Mark Davenport, Ronald DeVore and Michael Wakin. *A simple proof of the restricted isometry property for random matrices.* Constructive Approximation, vol. 28, no. 3, pages 253–263, 2008.

[Baron 2009] Dror Baron, Shriram Sarvotham and Richard G Baraniuk. *Bayesian compressive sensing via belief propagation.* IEEE Transactions on Signal Processing, vol. 58, no. 1, pages 269–280, 2009.

[Beaton 1974] Albert E Beaton and John W Tukey. *The fitting of power series, meaning polynomials, illustrated on band-spectroscopic data.* Technometrics, vol. 16, no. 2, pages 147–185, 1974.

[Beck 2009] Amir Beck and Marc Teboulle. *Fast gradient-based algorithms for constrained total variation image denoising and deblurring problems.* IEEE transactions on image processing, vol. 18, no. 11, pages 2419–2434, 2009.

[Berent 2009] Jesse Berent, Pier Luigi Dragotti and Thierry Blu. *Sampling piecewise sinusoidal signals with finite rate of innovation methods.* IEEE Transactions on Signal Processing, vol. 58, no. 2, pages 613–625, 2009.

[Blu 2008] Thierry Blu, Pier-Luigi Dragotti, Martin Vetterli, Pina Marziliano and Lionel Coulot. *Sparse sampling of signal innovations.* IEEE Signal Processing Magazine, vol. 25, no. ARTICLE, pages 31–40, 2008.

[Blumensath 2009] Thomas Blumensath and Mike E Davies. *Iterative hard thresholding for compressed sensing.* Applied and computational harmonic analysis, vol. 27, no. 3, pages 265–274, 2009.

[Cadzow 1988] J. A. Cadzow. *Signal enhancement-a composite property mapping algorithm.* IEEE Transactions on Acoustics, Speech, and Signal Processing, vol. 36, no. 1, pages 49–62, Jan 1988.

[Cai 2011] T Tony Cai and Lie Wang. *Orthogonal matching pursuit for sparse signal recovery with noise.* Institute of Electrical and Electronics Engineers, 2011.

[Candes 2004] Emmanuel Candes and Terence Tao. *Near optimal signal recovery from random projections: Universal encoding strategies?* arXiv preprint math/0410542, 2004.

[Candès 2005] Emmanuel J Candès and Terence Tao. *Decoding by linear programming.* Information Theory, IEEE Transactions on, vol. 51, no. 12, pages 4203–4215, 2005.

[Candès 2006a] Emmanuel J Candès, Justin Romberg and Terence Tao. *Robust uncertainty principles: Exact signal reconstruction from highly incomplete frequency information.* Information Theory, IEEE Transactions on, vol. 52, no. 2, pages 489–509, 2006.

[Candes 2006b] Emmanuel J Candes, Justin K Romberg and Terence Tao. *Stable signal recovery from incomplete and inaccurate measurements.* Communications on Pure and Applied Mathematics: A Journal Issued by the Courant Institute of Mathematical Sciences, vol. 59, no. 8, pages 1207–1223, 2006.

[Candès 2007a] EJ Candès. *Lectures on compressive sampling and frontiers in signal processing.* The Institute for Mathematics and its Applications, pages 2006–2007, 2007.

[Candès 2007b] Emmanuel Candès and Justin Romberg. *Sparsity and incoherence in compressive sampling.* Inverse problems, vol. 23, no. 3, page 969, 2007.

[Candès 2007c] Emmanuel J Candès. *ℓ_1-magic.* Technical report, 2007.

[Candès 2008] Emmanuel J Candès and Michael B Wakin. *An introduction to compressive sampling [a sensing/sampling paradigm that goes against the common knowledge in data acquisition].* IEEE signal processing magazine, vol. 25, no. 2, pages 21–30, 2008.

[Chartrand 2008] Rick Chartrand and Wotao Yin. *Iteratively reweighted algorithms for compressive sensing.* In 2008 IEEE International Conference on Acoustics, Speech and Signal Processing, pages 3869–3872. IEEE, 2008.

[Chen 2001] Scott Shaobing Chen, David L Donoho and Michael A Saunders. *Atomic decomposition by basis pursuit.* SIAM review, vol. 43, no. 1, pages 129–159, 2001.

[Cohen 2009] Albert Cohen, Wolfgang Dahmen and Ronald DeVore. *Compressed sensing and best k-term approximation.* Journal of the American mathematical society, vol. 22, no. 1, pages 211–231, 2009.

[Dabov 2007] K Dabov, A Foi, V Katkovnik and K Egiazarian. *Image denoising by sparse 3-D transform-domain collaborative filtering. Image Processing, IEEE Transactions on 16 (8), pp. 2080-2095.* 2007.

[Daubechies 2004] Ingrid Daubechies, Michel Defrise and Christine De Mol. *An iterative thresholding algorithm for linear inverse problems with a sparsity constraint.* Communications on Pure and Applied Mathematics: A Journal Issued by the Courant Institute of Mathematical Sciences, vol. 57, no. 11, pages 1413–1457, 2004.

[Do 2011] Thong T Do, Lu Gan, Nam H Nguyen and Trac D Tran. *Fast and efficient compressive sensing using structurally random matrices.* IEEE Transactions on signal processing, vol. 60, no. 1, pages 139–154, 2011.

[Donoho 1994] David L Donoho and Iain M Johnstone. *Minimax risk overl p-balls forl p-error.* Probability Theory and Related Fields, vol. 99, no. 2, pages 277–303, 1994.

[Donoho 2001] David L Donoho and Xiaoming Huo. *Uncertainty principles and ideal atomic decomposition.* Information Theory, IEEE Transactions on, vol. 47, no. 7, pages 2845–2862, 2001.

[Donoho 2006a] David Donoho. *For most large underdetermined system of linear equations the miniaml Ll-norm solution is also the sparseset solution.* Communications on pure and applied mathematics, 2006.

[Donoho 2006b] David L Donoho. *Compressed sensing.* Information Theory, IEEE Transactions on, vol. 52, no. 4, pages 1289–1306, 2006.

[Donoho 2009] David L Donoho, Arian Maleki and Andrea Montanari. *Message-passing algorithms for compressed sensing.* Proceedings of the National Academy of Sciences, vol. 106, no. 45, pages 18914–18919, 2009.

[Donoho 2010] David L Donoho, Arian Maleki and Andrea Montanari. *Message passing algorithms for compressed sensing: I. motivation and construction.* In 2010 IEEE Information Theory Workshop on Information Theory (ITW 2010, Cairo), pages 1–5. IEEE, 2010.

[Donoho 2011] David L Donoho, Arian Maleki and Andrea Montanari. *How to design message passing algorithms for compressed sensing.* preprint, 2011.

[Donoho 2012] David L Donoho, Yaakov Tsaig, Iddo Drori and Jean-Luc Starck. *Sparse solution of underdetermined systems of linear equations by stagewise orthogonal matching pursuit.* Information Theory, IEEE Transactions on, vol. 58, no. 2, pages 1094–1121, 2012.

[Dragotti 2005] P. L. Dragotti, M. Vetterli and T. Blu. *Exact sampling results for signals with finite rate of innovation using Strang-Fix conditions and local kernels.* In Proceedings. (ICASSP '05). IEEE International Conference on Acoustics, Speech, and Signal Processing, 2005., volume 4, pages iv/233–iv/236 Vol. 4, March 2005.

[Dragotti 2007] Pier Luigi Dragotti, Martin Vetterli and Thierry Blu. *Sampling moments and reconstructing signals of finite rate of innovation: Shannon meets Strang-Fix.* IEEE Transactions on signal processing, vol. 55, no. ARTICLE, pages 1741–1757, 2007.

[Emmanuel 2004] Candès Emmanuel, Justin Romberg and Terence Tao. *Robust uncertainty principles: Exact signal reconstruction from highly incomplete frequency information.* 2004.

[Fanet 2014] Hervé Fanet. Medical imaging based on magnetic fields and ultrasounds. John Wiley & Sons, 2014.

[Figueiredo 2001] Mário AT Figueiredo and Robert D Nowak. *Wavelet-based image estimation: an empirical Bayes approach using Jeffrey's noninformative prior.* IEEE Transactions on Image Processing, vol. 10, no. 9, pages 1322–1331, 2001.

[Golub 1999] Gene H Golub, Peyman Milanfar and James Varah. *A stable numerical method for inverting shape from moments.* SIAM Journal on Scientific Computing, vol. 21, no. 4, pages 1222–1243, 1999.

[Herrity 2006] Kyle K Herrity, Anna C Gilbert and Joel A Tropp. *Sparse approximation via iterative thresholding.* In 2006 IEEE International Conference on Acoustics Speech and Signal Processing Proceedings, volume 3, pages III–III. IEEE, 2006.

[Hill 2016] Paul R Hill, Jong-Hoon Kim, Adrian Basarab, Denis Kouamé, David R Bull and Alin Achim. *Compressive imaging using approximate message passing and a Cauchy prior in the wavelet domain.* In 2016 IEEE International Conference on Image Processing (ICIP), pages 2514–2518. IEEE, 2016.

[Hockin 1884] Charles Hockin. *On the Estimation of Aperture in the Microscope.* Journal of the Royal Microscopical Society, vol. 4, no. 3, pages 337–347, 1884.

[Hormati 2007] Ali Hormati and Martin Vetterli. *Annihilating filter-based decoding in the compressed sensing framework.* In Wavelets XII, volume 6701, page 670121. International Society for Optics and Photonics, 2007.

[Hozumi 2004] N Hozumi, R Yamashita, C.-K Lee, M Nagao, K Kobayashi, Y Saijo, M Tanaka, N Tanaka and S Ohtsuki. *Time–frequency analysis for pulse driven ultrasonic microscopy for biological tissue characterization.* Ultrasonics, vol. 42, no. 1, pages 717 – 722, 2004. Proceedings of Ultrasonics International 2003.

[Hua 1990] Yingbo Hua and Tapan K Sarkar. *Matrix pencil method for estimating parameters of exponentially damped/undamped sinusoids in noise.* IEEE Transactions on Acoustics, Speech, and Signal Processing, vol. 38, no. 5, pages 814–824, 1990.

[Indyk 2008] Piotr Indyk and Milan Ruzic. *Near-optimal sparse recovery in the l1 norm.* In 2008 49th Annual IEEE Symposium on Foundations of Computer Science, pages 199–207. IEEE, 2008.

[Johnston 1979] RN Johnston, Abdullah Atalar, J Heiserman, V Jipson and CF Quate. *Acoustic microscopy: resolution of subcellular detail.* Proceedings of the National Academy of Sciences, vol. 76, no. 7, pages 3325–3329, 1979.

[Kabashima 2003] Yoshiyuki Kabashima. *A CDMA multiuser detection algorithm on the basis of belief propagation.* Journal of Physics A: Mathematical and General, vol. 36, no. 43, page 11111, 2003.

[Keller 2008] Philipp J Keller, Annette D Schmidt, Joachim Wittbrodt and Ernst HK Stelzer. *Reconstruction of zebrafish early embryonic development by scanned light sheet microscopy.* science, vol. 322, no. 5904, pages 1065–1069, 2008.

[Khalidov 2005] Ildar Khalidov, Thierry Blu and Michael Unser. *Generalized L-spline wavelet bases.* In Wavelets XI, volume 5914, page 59140F. International Society for Optics and Photonics, 2005.

[Kim 2007] Seung-Jean Kim, Kwangmoo Koh, Michael Lustig, Stephen Boyd and Dimitry Gorinevsky. *An interior-point method for large-scale ℓ_1-regularized least squares.* Selected Topics in Signal Processing, IEEE Journal of, vol. 1, no. 4, pages 606–617, 2007.

[Kim 2016] Jong-Hoon Kim, Adrian Basarab, Paul R Hill, David R Bull, Denis Kouamé and Alin Achim. *Ultrasound image reconstruction from compressed measurements using approximate message passing.* In 2016 24th European Signal Processing Conference (EUSIPCO), pages 557–561. IEEE, 2016.

[Kim 2017] JH Kim, PR Hill, Nishan Canagarajah, Daniel Rohrbach, Denis Kouamé, Jonathan Mamou, Alin Achim and Adrian Basarab. *Compressed quantitative acoustic microscopy.* In 2017 IEEE International Ultrasonics Symposium (IUS), pages 1–4. IEEE, 2017.

[Kim 2018a] J. Kim, J. Mamou, P. R. Hill, N. Canagarajah, D. Kouamé, A. Basarab and A. Achim. *Approximate Message Passing Reconstruction of Quantitative Acoustic Microscopy Images.* IEEE Transactions on Ultrasonics, Ferroelectrics, and Frequency Control, vol. 65, no. 3, pages 327–338, March 2018.

[Kim 2018b] JH Kim, D Kouamé, A Basarab, J Mamou and A Achim. *Reconstruction of quantitative acoustic microscopy images from RF signals sampled at innovation rate.* In 2018 IEEE International Ultrasonics Symposium (IUS), pages 1–4. IEEE, 2018.

[Kim 2019] JH Kim, D Kouamé, A Basarab, J Mamou and A Achim. *Spatio-temporal compressed quantitative acoustic microscopy.* In 2019 IEEE International Ultrasonics Symposium (IUS), pages 1–4. IEEE, 2019.

[Kinsler 1999] Lawrence E Kinsler, Austin R Frey, Alan B Coppens and James V Sanders. *Fundamentals of acoustics.* Fundamentals of Acoustics, 4th Edition, by Lawrence E. Kinsler, Austin R. Frey, Alan B. Coppens, James V. Sanders, pp. 560. ISBN 0-471-84789-5. Wiley-VCH, December 1999., page 560, 1999.

[Kirkhorn 1999] Johan Kirkhorn. *Introduction to IQ-demodulation of RF-data.* IFBT, NTNU, vol. 15, 1999.

[Kouamé 2015] Denis Kouamé. *Lecture notes in Ultrasound imaging: Systems, signals and image processing.* Ecole d'été du LabEx PRIMES, 2015.

[Kremkau 1993] Frederick W Kremkau. *Multiple-element transducers.* RadioGraphics, vol. 13, no. 5, pages 1163–1176, 1993.

[Kutay 2001] M Alper Kutay, Athina P Petropulu and Catherine W Piccoli. *On modeling biomedical ultrasound RF echoes using a power-law shot-noise model.* IEEE transactions on ultrasonics, ferroelectrics, and frequency control, vol. 48, no. 4, pages 953–968, 2001.

[Lawson 1961] C.L. Lawson. *Contributions to the theory of linear least maximum approximations.* PhD thesis, UCLA, 1961.

[Leiserson 2001] Charles Eric Leiserson, Ronald L Rivest, Thomas H Cormen and Clifford Stein. Introduction to algorithms, volume 6. MIT press Cambridge, MA, 2001.

[Lemons 1974] RA Lemons and CF Quate. *Acoustic microscope—scanning version.* Applied Physics Letters, vol. 24, no. 4, pages 163–165, 1974.

[Lu 2008] Yue M Lu and Minh N Do. *A theory for sampling signals from a union of subspaces.* IEEE transactions on signal processing, vol. 56, no. 6, pages 2334–2345, 2008.

[Maleki 2009] Arian Maleki and David L Donoho. *Optimally tuned iterative reconstruction algorithms for compressed sensing.* arXiv preprint arXiv:0909.0777, 2009.

[Mallat 1999] Stéphane Mallat. A wavelet tour of signal processing. Elsevier, 1999.

[Mamou 2015a] J. Mamou, D. Rohrbach, E. Saegusa-Beecroft, E. Yanagihara, J. Machi and E. J. Feleppa. *Ultrasound-scattering models based on quantitative acoustic microscopy of fresh samples and unstained fixed sections from cancerous human lymph nodes.* In 2015 IEEE International Ultrasonics Symposium (IUS), pages 1–4, Oct 2015.

[Mamou 2015b] Jonathan Mamou, Daniel Rohrbach, Emi Saegusa-Beecroft, Eugene Yanagihara, Junji Machi and Ernest J Feleppa. *Ultrasound-scattering models based on quantitative acoustic microscopy of fresh samples and unstained fixed sections from cancerous human lymph nodes.* In 2015 IEEE International Ultrasonics Symposium (IUS), pages 1–4. IEEE, 2015.

[Maravic 2003] Irena Maravic, Julius Kusuma and Martin Vetterli. *Low-sampling rate UWB channel characterization and synchronization.* Journal of Communications and Networks, vol. 5, no. ARTICLE, pages 319–327, 2003.

[Maravic 2004] Irena Maravic, Martin Vetterli and Kannan Ramchandran. *Channel estimation and synchronization with sub-Nyquist sampling and application to ultra-wideband systems.* In 2004 IEEE International Symposium on Circuits and Systems (IEEE Cat. No. 04CH37512), volume 5, pages V–V. IEEE, 2004.

[Maravic 2005] Irena Maravic and Martin Vetterli. *Sampling and reconstruction of signals with finite rate of innovation in the presence of noise.* IEEE Transactions on Signal Processing, vol. 53, no. ARTICLE, pages 2788–2805, 2005.

[Mendelson 2008] Shahar Mendelson, Alain Pajor and Nicole Tomczak-Jaegermann. *Uniform uncertainty principle for Bernoulli and subgaussian ensembles.* Constructive Approximation, vol. 28, no. 3, pages 277–289, 2008.

[Metzler 2016] Christopher A Metzler, Arian Maleki and Richard G Baraniuk. *From denoising to compressed sensing.* IEEE Transactions on Information Theory, vol. 62, no. 9, pages 5117–5144, 2016.

[Moor 1993] Bart De Moor. *Structured total least squares and L2 approximation problems.* Linear Algebra and its Applications, vol. 188-189, pages 163 – 205, 1993.

[Naidu 2016] R Ramu Naidu, Phanindra Jampana and Challa S Sastry. *Deterministic compressed sensing matrices: Construction via euler squares and applications.* IEEE Transactions on Signal Processing, vol. 64, no. 14, pages 3566–3575, 2016.

[Natarajan 1995] Balas Kausik Natarajan. *Sparse approximate solutions to linear systems.* SIAM journal on computing, vol. 24, no. 2, pages 227–234, 1995.

[Needell 2009a] Deanna Needell and Joel A Tropp. *CoSaMP: Iterative signal recovery from incomplete and inaccurate samples.* Applied and Computational Harmonic Analysis, vol. 26, no. 3, pages 301–321, 2009.

[Needell 2009b] Deanna Needell and Roman Vershynin. *Uniform uncertainty principle and signal recovery via regularized orthogonal matching pursuit.* Foundations of computational mathematics, vol. 9, no. 3, pages 317–334, 2009.

[Needell 2010] Deanna Needell and Roman Vershynin. *Signal recovery from incomplete and inaccurate measurements via regularized orthogonal matching pursuit.* Selected Topics in Signal Processing, IEEE Journal of, vol. 4, no. 2, pages 310–316, 2010.

[Nocedal 2006] Jorge Nocedal and Stephen Wright. Numerical optimization. Springer Science & Business Media, 2006.

[Oñativia 2013] Jon Oñativia, Simon R Schultz and Pier Luigi Dragotti. *A finite rate of innovation algorithm for fast and accurate spike detection from two-photon calcium imaging.* Journal of Neural Engineering, vol. 10, no. 4, page 046017, 2013.

[Pan 2017] H. Pan, T. Blu and M. Vetterli. *Towards Generalized FRI Sampling With an Application to Source Resolution in Radioastronomy.* IEEE Transactions on Signal Processing, vol. 65, no. 4, pages 821–835, Feb 2017.

[Pearl 2014] Judea Pearl. Probabilistic reasoning in intelligent systems: networks of plausible inference. Elsevier, 2014.

[Petropulu 2000] Athina P Petropulu, J-C Pesquet and Xueshi Yang. *Power-law shot noise and its relationship to long-memory/spl alpha/-stable processes.* IEEE Transactions on Signal Processing, vol. 48, no. 7, pages 1883–1892, 2000.

[Porat 1997] B. Porat. A course in digital signal processing. Wiley, New York, 1997.

[Powell 1984] James L Powell. *Least absolute deviations estimation for the censored regression model.* Journal of Econometrics, vol. 25, no. 3, pages 303–325, 1984.

[Qaisar 2013] Saad Qaisar, Rana Muhammad Bilal, Wafa Iqbal, Muqaddas Naureen and Sungyoung Lee. *Compressive sensing: From theory to applications, a survey.* Journal of Communications and networks, vol. 15, no. 5, pages 443–456, 2013.

[Quate 1979] C. F. Quate, A. Atalar and H. K. Wickramasinghe. *Acoustic microscopy with mechanical scanning—A review.* Proceedings of the IEEE, vol. 67, no. 8, pages 1092–1114, Aug 1979.

[Quinsac 2010] Céline Quinsac, Adrian Basarab, Jean-Marc Girault and Denis Kouamé. *Compressed sensing of ultrasound images: Sampling of spatial and frequency domains.* In 2010 IEEE Workshop On Signal Processing Systems, pages 231–236. IEEE, 2010.

[Rauhut 2010] Holger Rauhut. *Compressive sensing and structured random matrices.* Theoretical foundations and numerical methods for sparse recovery, vol. 9, pages 1–92, 2010.

[Richardson 2008] Tom Richardson and Ruediger Urbanke. Modern coding theory. Cambridge university press, 2008.

[Rohrbach 2015a] D. Rohrbach, H. O. Lloyd, R. H. Silverman, R. Urs and J. Mamou. *Acoustic-property maps of the cornea for improved high-frequency ultrasound corneal biometric accuracy.* In 2015 IEEE International Ultrasonics Symposium (IUS), pages 1–4, Oct 2015.

[Rohrbach 2015b] Daniel Rohrbach, Harriet O Lloyd, Ronald H Silverman and Jonathan Mamou. *Fine-resolution maps of acoustic properties at 250 MHz of unstained fixed murine retinal layers.* The Journal of the Acoustical Society of America, vol. 137, no. 5, pages EL381–EL387, 2015.

[Rohrbach 2017] D. Rohrbach, A. Jakob, H. O. Lloyd, S. H. Tretbar, R. H. Silverman and J. Mamou. *A Novel Quantitative 500-MHz Acoustic Microscopy System for Ophthalmologic Tissues.* IEEE Transactions on Biomedical Engineering, vol. 64, no. 3, pages 715–724, March 2017.

[Rohrbach 2018] D. Rohrbach and J. Mamou. *Autoregressive Signal Processing Applied to High-Frequency Acoustic Microscopy of Soft Tissues.* IEEE Transactions on Ultrasonics, Ferroelectrics, and Frequency Control, vol. 65, no. 11, pages 2054–2072, Nov 2018.

[Rudresh 2017] S. Rudresh and C. S. Seelamantula. *Finite-Rate-of-Innovation-Sampling-Based Super-Resolution Radar Imaging.* IEEE Transactions on Signal Processing, vol. 65, no. 19, pages 5021–5033, Oct 2017.

[Sarkar 1995] Tapan K Sarkar and Odilon Pereira. *Using the matrix pencil method to estimate the parameters of a sum of complex exponentials.* IEEE Antennas and Propagation Magazine, vol. 37, no. 1, pages 48–55, 1995.

[Schermelleh 2010] Lothar Schermelleh, Rainer Heintzmann and Heinrich Leonhardt. *A guide to super-resolution fluorescence microscopy.* The Journal of cell biology, vol. 190, no. 2, pages 165–175, 2010.

[Schoenberg 1946] Isaac Jacob Schoenberg. *Contributions to the problem of approximation of equidistant data by analytic functions. Part B. On the problem of osculatory interpolation. A second class of analytic approximation formulae.* Quarterly of Applied Mathematics, vol. 4, no. 2, pages 112–141, 1946.

[Selesnick 2009] Ivan Selesnick. *A derivation of the soft-thresholding function.* Polytechnic Institute of New York University, 2009.

[Shannon 1984] Claude E Shannon. *Communication in the presence of noise.* Proceedings of the IEEE, vol. 72, no. 9, pages 1192–1201, 1984.

[Simoncelli 1999] Eero P Simoncelli. *Bayesian denoising of visual images in the wavelet domain.* In Bayesian inference in wavelet-based models, pages 291–308. Springer, 1999.

[Smith 2010] Nadine Barrie Smith and Andrew Webb. Introduction to medical imaging: physics, engineering and clinical applications. Cambridge university press, 2010.

[Som 2012] Subhojit Som and Philip Schniter. *Compressive imaging using approximate message passing and a Markov-tree prior.* IEEE transactions on signal processing, vol. 60, no. 7, pages 3439–3448, 2012.

[Stoica 2005] Petre Stoica, Randolph L Moses*et al.* *Spectral analysis of signals.* 2005.

[Strang 2011] Gilbert Strang and George Fix. *A Fourier analysis of the finite element variational method.* In Constructive aspects of functional analysis, pages 793–840. Springer, 2011.

[Tan 2015] Jin Tan, Yanting Ma and Dror Baron. *Compressive imaging via approximate message passing with image denoising.* IEEE Transactions on Signal Processing, vol. 63, no. 8, pages 2085–2092, 2015.

[Thouless 1977] David J Thouless, Philip W Anderson and Robert G Palmer. *Solution of'solvable model of a spin glass'.* Philosophical Magazine, vol. 35, no. 3, pages 593–601, 1977.

[Tibshirani 1996] Robert Tibshirani. *Regression shrinkage and selection via the lasso.* Journal of the Royal Statistical Society: Series B (Methodological), vol. 58, no. 1, pages 267–288, 1996.

[Tropp 2007] Joel A Tropp and Anna C Gilbert. *Signal recovery from random measurements via orthogonal matching pursuit.* IEEE Transactions on information theory, vol. 53, no. 12, pages 4655–4666, 2007.

[Trots 2007] Ihor Trots and Andrzej Nowicki. *Influence of the transducer bandwidth on compressed ultrasonic echoes.* Archives of Acoustics, vol. 32, no. 4, pages 903–915, 2007.

[Tsaig 2006] Yaakov Tsaig and David L Donoho. *Extensions of compressed sensing.* Signal processing, vol. 86, no. 3, pages 549–571, 2006.

[Tur 2011] Ronen Tur, Yonina C Eldar and Zvi Friedman. *Innovation rate sampling of pulse streams with application to ultrasound imaging.* Signal Processing, IEEE Transactions on, vol. 59, no. 4, pages 1827–1842, 2011.

[Unser 1999] Michael Unser. *Splines: A perfect fit for signal and image processing.* IEEE Signal processing magazine, vol. 16, no. ARTICLE, pages 22–38, 1999.

[Unser 2005] Michael Unser and Thierry Blu. *Cardinal exponential splines: Part I-Theory and filtering algorithms.* IEEE Transactions on Signal Processing, vol. 53, no. 4, pages 1425–1438, 2005.

[Urigüen 2011] Jose Antonio Urigüen, Pier Luigi Dragotti and Thierry Blu. *On the exponential reproducing kernels for sampling signals with finite rate of innovation.* Proceedings of Sampling Theory and Applications (SampTA), 2011.

[Urigüen 2013a] Jose Antonio Urigüen. *Exact and approximate Strang-Fix conditions to reconstruct signals with finite rate of innovation from samples taken with arbitrary kernels.* 2013.

[Urigüen 2013b] Jose Antonio Urigüen, Thierry Blu and Pier Luigi Dragotti. *FRI sampling with arbitrary kernels.* IEEE Transactions on Signal Processing, vol. 61, no. 21, pages 5310–5323, 2013.

[Vetterli 2002] M. Vetterli, P. Marziliano and T. Blu. *Sampling signals with finite rate of innovation.* IEEE Transactions on Signal Processing, vol. 50, no. 6, pages 1417–1428, June 2002.

[Vonesch 2007] Cédric Vonesch, Thierry Blu and Michael Unser. *Generalized Daubechies wavelet families.* IEEE Transactions on Signal Processing, vol. 55, no. 9, pages 4415–4429, 2007.

[Wan 2008] Tao Wan, Nishan Canagarajah and Alin Achim. *Compressive image fusion.* In 2008 15th IEEE International Conference on Image Processing, pages 1308–1311. IEEE, 2008.

[Wang 2004] Zhou Wang, Alan Conrad Bovik, Hamid Rahim Sheikh and Eero P Simoncelli. *Image quality assessment: from error visibility to structural similarity.* Image Processing, IEEE Transactions on, vol. 13, no. 4, pages 600–612, 2004.

[Wei 2016] Xiaoyao Wei. *Extensions of the theory of sampling signals with finite rate of Innovation, performance analysis and an application to single image super-resolution.* 2016.

[Yang 2018] Bin Yang, Ning-Jiun Jan, Bryn Brazile, Andrew Voorhees, Kira L Lathrop and Ian A Sigal. *Polarized light microscopy for 3-dimensional mapping of collagen fiber architecture in ocular tissues.* Journal of biophotonics, vol. 11, no. 8, page e201700356, 2018.

[Yedidia 2005] Jonathan S Yedidia, William T Freeman and Yair Weiss. *Constructing free-energy approximations and generalized belief propagation algorithms.* IEEE Transactions on information theory, vol. 51, no. 7, pages 2282–2312, 2005.